

UNIVERSITÀ DEGLI STUDI DI NAPOLI FEDERICO II



DIPARTIMENTO DI INGEGNERIA CHIMICA, DEI MATERIALI
E DELLA PRODUZIONE INDUSTRIALE

PHD PROGRAMME IN
PRODUCTION TECHNOLOGY AND SYSTEMS
COORDINATOR: PROF. LUIGI CARRINO
XXVI CYCLE

PHD THESIS

**MACHINING PROCESS MONITORING VIA
COGNITIVE SENSOR FUSION**

TUTOR

PROF. ING. ROBERTO TETI

PHD CANDIDATE

ING. SARA KARAM

ACADEMIC YEAR 2013/2014



FRAUNHOFER JOINT LABORATORY OF EXCELLENCE ON ADVANCED PRODUCTION TECHNOLOGY
FH-J_LEAPT AT DICMAPI FEDERICO II

Table of Contents

Acknowledgements.....	7
1. Introduction.....	9
1.1. Scope and purposes	9
1.2. Review of the publications of the Ph.D. Candidate.....	11
1.3. State of the Art	12
1.3.1. Historical/philosophical background of sensorial perception.....	12
1.3.2. Modern theories of sensorial perception	13
1.3.3. Sensors and sensor systems for machining	13
1.3.4. Advanced Signal Processing	18
1.3.5. Monitoring scopes.....	21
1.3.6. Decision making support systems and paradigms	22
1.3.7. Sensor fusion technology	27
2. Conventional and advanced signal processing and feature extraction.....	31
2.1. Conventional feature extraction	31
2.2. Wavelet packet transform	32
2.2.1 Generalities.....	32
2.2.2 Wavelet packet decomposition.....	40
2.2.3 Wavelet packet transform feature extraction.....	41
2.2.4 Matlab procedure	42
3. Knowledge based decision making	45
3.1. Neural network based pattern recognition	45
3.2. Training algorithm: Levenberg-Marquardt (LM).....	47
3.3. Matlab Procedure	49
4. Sensor monitoring applications	53
4.1. Chip form classification in turning of AISI 1045 carbon steel	54
4.1.1 Generalities: chip formation	55
4.1.2 Chip form classification: ISO 3685, Annex G [150]	59
4.1.3 Experimental setup and procedure.....	60
4.1.4 Sensor signal data analysis	64
4.1.5 Decision making and results.....	68
4.2. Residual stress assessment	71
4.2.1 Generalities: residual stress in machining.....	71

4.2.2	X-ray diffraction technique	72
4.2.3	Basic procedure	79
4.2.4	X-ray stress analyzer.....	86
4.2.5	Experimental setup and procedure.....	88
4.2.6	Residual stress measurement results.....	95
4.2.7	Sensor signal data analysis.....	97
4.2.8	Decision making and results.....	98
4.3.	Surface roughness assessment.....	101
4.3.1	Generalities	101
4.3.2	Surface roughness measurement techniques	105
4.3.3	Experimental setup and procedure.....	114
4.3.4	Sensor signal data analysis.....	119
4.3.5	Decision making and results.....	125
5.	Conclusion	132
	References.....	134

Acknowledgements

The activities of this PhD thesis work has received funding support from the European Community's Seventh Framework Program FP7 under grant agreements n. 213855 (ACCENT) and n. 285489 (IFaCOM).

The Fraunhofer Joint Laboratory of Excellence for Advanced Production Technology (Fh-J_LEAPT) at the Department of Chemical, Materials and Industrial Production Engineering, University of Naples Federico II, is gratefully acknowledged for its support to this research work.

Foremost, I would like to express my sincere gratitude to my advisor Prof. Ing. Roberto Teti for the continuous support during my Ph.D. study and research, for his patience, motivation, enthusiasm, and immense knowledge. His guidance helped me in all the time of research and writing of this thesis.

I would also like to thank my lab colleagues Tiziana Segreto, Alessandra Caggiano, Piera Centobelli, Davide Matarazzo, and Doriana D'Addona.

I would not have contemplated this road if not for my parents, Charbel and Laure, who supported me all along and helped me become who I am now. To my parents, thank you. My sister, Lara, has also been the best of friends along this journey encouraging me to look forward. This thesis would also not be possible without the love and support of my Neapolitan family, Alessandro Simeone, Danilo Spasiano, Rosa Giordano, and CEICC (Centro Europeo di informazione cultura cittadinanza) in general, who gave me a home away from home.

Lastly, a special thank you to a person that is not with us anymore, Franca Sibilio, an amazing and radiant woman, that taught me the real meaning of being a woman and helped me become a better person, a better lady.

1. Introduction

1.1. Scope and purposes

This thesis work was developed in conjunction with the activities of the EC FP7 *Adaptive Control of Manufacturing Processes for a New Generation of Jet Engine Components* (ACCENT) Project (agreement n. 213855) as well as the EC FP7 *Intelligent Fault Correction and self-Optimizing Manufacturing systems* (IFaCOM) Project (agreement n. 285489).

The goal of this thesis work can be summarized as follows: sensor monitoring of machining processes for the ultimate goal of optimizing the machining process under study, through processing and analyzing the detected sensor signals during the machining process and relating them to a chosen quality parameter of the machined workpiece.

First of all, several experimental campaigns were carried out in an industrial environment. A multi sensor monitoring system, endowed with diverse sensing units was employed during each of the experimental campaigns in order to acquire different sensor signals on an online basis.

Mainly, three sensor-monitoring applications were studied in this thesis work resulting in different multi sensor monitoring system adapted to the three applications under study.

Raw signals detected during the experiments were processed and analyzed using mainly conventional and advanced signal analysis methods in order to extract significant features useful for knowledge-based decision making on process conditions.

The thesis work includes material characterization tests carried out to inspect the surface integrity of the workpiece, chip form classification, and surface roughness levels in polishing with the scope of correlating these conditions to the extracted sensor signals features.

A decision-making support system, neural networks for pattern recognition, was employed the sensor signal features extracted by signal processing techniques for the identification of defects in the workpiece due to the machining process.

The flow chart shown in Figure 1.1 summarizes the activities and steps followed in this thesis work.

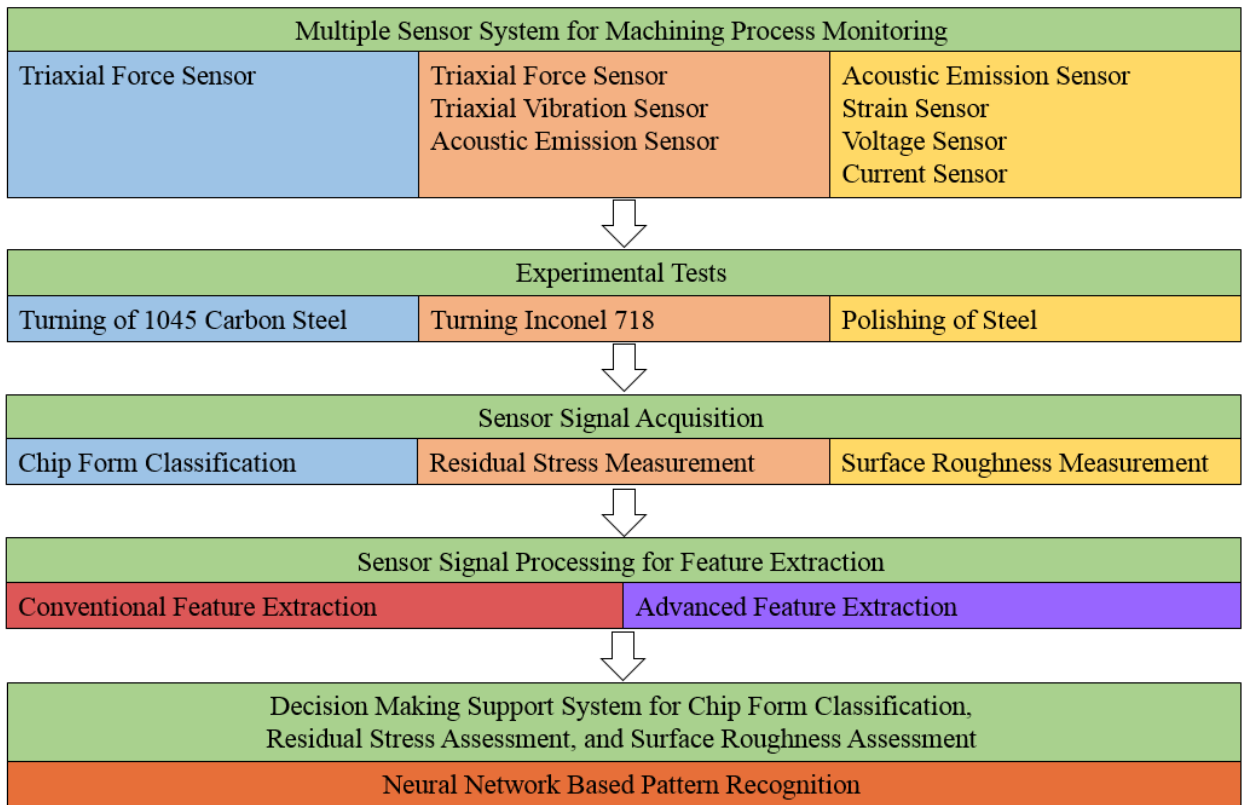


Figure 1.1: Activities flow chart.

1.2. Review of the publications of the Ph.D. Candidate

SEGRETO, T., KARAM, S., SIMEONE, A., TETI, R., 2013, RESIDUAL STRESS ASSESSMENT IN INCONEL 718 MACHINING THROUGH WAVELET SENSOR SIGNAL ANALYSIS AND SENSOR FUSION PATTERN RECOGNITION, 2ND CIRP GLOBAL WEB CONFERENCE (CIRPe2013), PROCEA CIRP, VOLUME 9, ISSN 2212-8271, PP. 103-108.

On-line residual stress assessment in turning of Inconel 718 was carried out through multiple sensor monitoring based on cutting force, acoustic emission and vibration signals acquisition and analysis. The detected sensor signals were processed by the wavelet packet transform technique to extract statistical features from the packet coefficients for the construction of wavelet feature vectors. The latter were used for sensor fusion pattern recognition through neural network data processing grounded on X-ray diffraction residual stress measurements on the turned part surface. The scope of the sensory data fusion approach was to achieve a robust scheme for multi-sensor monitoring decision making on machined surface integrity in terms of residual stress level acceptability. [1]

KARAM, S., TETI, R., 2012, WAVELET TRANSFORM FEATURE EXTRACTION FOR PATTERN RECOGNITION OF CHIP FORM IN C STEEL TURNING, 8TH CIRP INT. CONFERENCE ON INTELLIGENT COMPUTATION IN MANUFACTURING ENGINEERING – CIRP ICME '12, 18-20 JULY, ISCHIA, ITALY, PP. 97-102

Cutting force sensor monitoring and wavelet decomposition signal processing were implemented for feature extraction and pattern recognition of chip form typology during turning of 1045 carbon steel. The wavelet packet transform was applied for the analysis of the detected cutting force signals by representing them in a time-frequency domain and providing for the extraction of wavelet packet statistical features. The latter were used to construct wavelet packet feature vectors, ranked according to the number of overlapping elements related to favourable or unfavourable chip forms that cause noise in the pattern recognition procedure (lower number, lower noise, higher rank). The eight highest ranked wavelet packet feature vectors were selected as inputs to a neural network decision-making system on chip form acceptability. Subsequently, a data refinement procedure was employed to improve the neural network performance in the chip form identification process. [2]

1.3. State of the Art

In cognitive sciences, sensorial perception is the conscious recognition and interpretation of sensory stimuli that serve as a basis for understanding, learning, and knowing or for motivating a particular action or reaction. In the 1950s, it was predicted that building perceiving machines would take about a decade, a goal which is still very far from achievement being a task far more complex than was imagined. [3]

1.3.1. Historical/philosophical background of sensorial perception

Since the early times of ancient Greek philosophy, several interesting views and theories concerning the connection between Sensorial Perception (SP), knowledge achievement and truth identification have emerged. These diverse concepts, views and theories concerning SP and knowledge acquisition are grouped into different categories that, along with the predominant cultural tendency in the course of time, attribute to SP a certain level of importance. (Table 1.1) [3]

Table 1.1: Concepts of sensorial perception (SP) and its role in knowledge acquisition and truth identification during the different epochs.

SP role	Authors of concepts/theories of SP in the course of epochs
Trivial, minor or no value	Heraclitus (535–475 B.C.); Parmenides (515–450 B.C.) and the Eleatics; Pyrrho (360–320 B.C.) and the Sceptics
Initiates cognition	Empedocles (490–430 B.C.); Democritus (460–370 B.C.) and the Atomists
Supports cognition	Plato (427–347 B.C.); Plotinus (205–270 A.D.); St. Augustine (354–430 A.D.); Hegel (1770–1831) and the Idealists
Indispensible for cognition	Aristotle (384–322 B.C.); St. Thomas Aquinas (1221–1274); Ockam (1280–1349); Spinoza (1632–1677); Leibniz (1646–1716); Locke (1632–1704) and the Empyrist; Kant (1724–1804); Peirce (1839–1914) and the Pragmatists
Basis of all knowledge acquisition	Epicurus (341–270 B.C.); Zeno (334–262 B.C.) and the Stoics; L. da Vinci (1452–1519); Telesio (1509–1588); Galilei (1564–1642); F. Bacon (1561–1626); Newton (1642–1727); Descartes (1596–1650) and the theory of passive perception; Condillac (1714–1780) and the Sensists; Stuart Mill (1806–1873), Comte (1798–1857) and the Positivists
Continuous adaptation of sensing to environment	Darwin (1809–1882), Avenarius (1843–1900), Mach (1838–1916) and the Empiriocriticists; Dewey (1859–1952) and the Instrumentalists; Bergson (1859–1941); Gregory [6–8] and the theory of active perception

1.3.2. Modern theories of sensorial perception

R. Descartes initially conceived the passive perception theory. The following “static” sequence of events can summarize it: surrounding \rightarrow input (senses) \rightarrow processing (brain) \rightarrow output (reaction). Mainstream philosophers, psychologists, neurologists and scientists still support this theory. However, nowadays, it is largely losing momentum. Instead, the theory of active perception has emerged from extensive research of sensory misapprehensions, most notably the works of Gregory [4] [5]. This theory of active perception, which is increasingly gaining experimental support, can be defined as the “dynamic” relationship between description (in the brain) \leftrightarrow senses \leftrightarrow surrounding, all of which holds true to the linear concept of experience [6].

1.3.3. Sensors and sensor systems for machining

The measuring techniques for the monitoring of machining operations have traditionally been classified into two approaches: direct and indirect. In the direct approach, the actual quantity of the variable, e.g. tool wear, is measured. In this case, some examples of direct measurement are the use of cameras for visual inspection, radioactive isotopes, laser beams, and electrical resistance. Many direct methods can only be used as laboratory experimental techniques but not on site techniques. Mainly, this is due to the practical limitations caused by numerous problems during machining such as access problems, illumination, and the use of cutting fluid. However, direct measurement has a high degree of accuracy and has been extensively employed in research laboratories to support investigations of fundamental measurable phenomena during machining processes. Through indirect measurement approaches, auxiliary quantities such as the cutting force components can be measured. The actual measurement/value/quantity is subsequently deduced through empirically determined correlations. These indirect methods are less accurate than direct ones but are also less complex and more suitable for practical applications. In contrast to traditional detecting methods, the indirect approach provides continuous monitoring of the machining process through sensing devices to quantify the performance of the process and provide information aiming at process optimization using sensors. Sensors commonly used for online measurement are illustrated in Figure 1.2. [3]

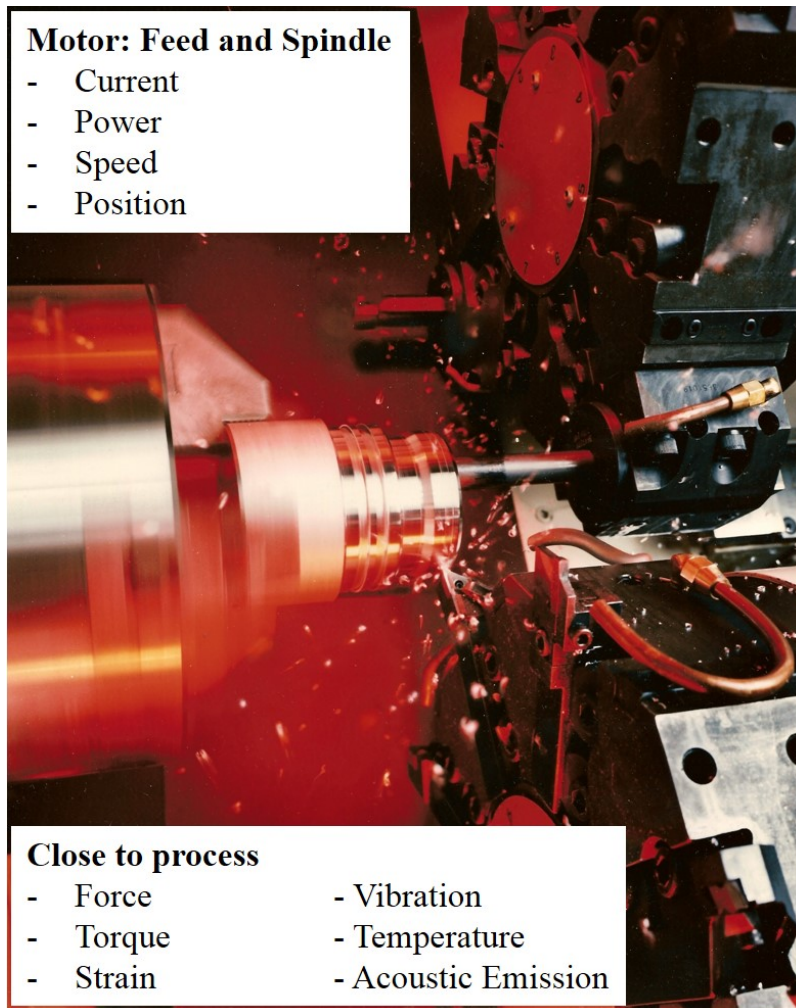


Figure 1.2: Measurable phenomena for online sensor monitoring [7].

Force and torque measuring technology and sensors

Any cutting operation requires a certain force to separate and remove the material from the workpiece. The monitoring of cutting forces in machining has been used extensively by researchers [8]. One of the aims of monitoring of cutting forces is the validation of analytical process models. Force sensors are highly sensitive and respond rapidly to changes during the cutting states. Torque sensors, like force sensors, also consist of a mechanical structure that responds to a deformation but, in this case, the applied load is torsional. Often, the underlying force measurement technology is identical. What is different is the application of torque sensors and the method of signal transmission from rotating tool holders. Both force and torque sensors generally employ sensing elements that convert the applied force or torsional load into deformation of an elastic element. The two main sensor types used are piezoelectric based and strain gage based sensors.

A piezoelectric based sensor is a device that uses the piezoelectric effect to measure changes in pressure, acceleration, strain or force by converting them to an electrical charge [9]. The force transducer mounted in line with the force path allows the direct force measurement using piezoelectric sensors. For lab-based applications that require more measurement

flexibility, multi-component force transducers have been developed and are extensively used. Rotating cutting force dynamometers are also available and contain force-sensing elements capable of measuring three components of force and torque. The data is transmitted from the rotating part of the sensor to a stator via telemetry. Rotating cutting force dynamometers can operate at speeds of up to 20,000 rpm and have been used for high speed milling of aerospace materials. Developments like the integration of force sensors into the machine structure have taken place over the last 10 years with concepts developed for drilling [10] and milling [11]. Figure 1.3 shows sensors integrated into the main force flux of the motor spindle.

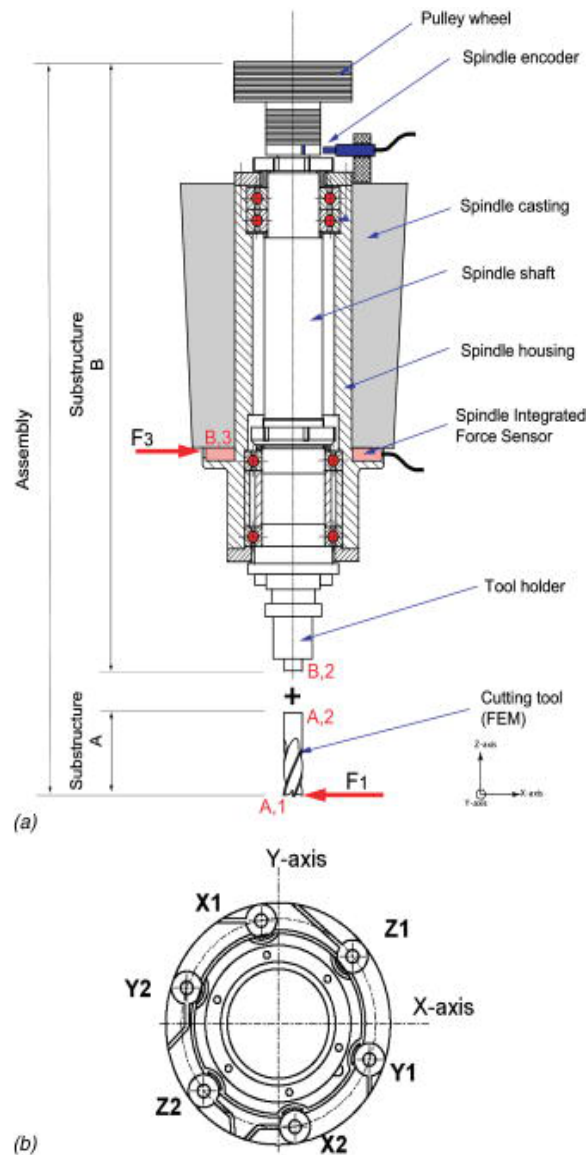


Figure 1.3 – Integrated force sensors in motor spindle [12].

Strain gage based sensors consist of a structure that deforms under a force. This type of transducers offer reasonably high frequency response and long-term stability. The most common type of strain gage consists of an insulating flexible backing, which supports a metallic foil pattern. The gauge is attached to the object. As the object is deformed, the foil is deformed, causing its electrical resistance to change. This resistance change, usually measured

using a Wheatstone bridge, is related to the strain by the quantity known as the gauge factor [13]. Figure 1.4 shows a strain gage sensor integrated into a static Swiss tool holder.



Figure 1.4: Strain gage sensor embedded in a static Swiss tool holder [14].

Acoustic emission measuring technology and sensors

There are several sources of acoustic emissions in machining and these causes are illustrated in Figure 1.5. Piezoelectric sensor technology is particularly suitable for measuring acoustic emission (AE) [11] [15] in machining process monitoring. With a very wide sensor dynamic bandwidth ranging between 100 kHz and 900 kHz, AE can detect most of the phenomena in machining. It is noted that significant data acquisition as well as signal processing is required [16]. Band pass filters usually provide great flexibility for AE detection by selecting the appropriate frequency ranges. The output signal from the AE sensor is fed through a pre-amplifier that has a high input impedance and low output impedance. A root mean square (RMS) converter, gain selection unit, and filters are typically contained within the preamplifier housing. Another potential principle for AE detection is the capacitance principle. The capacitance of two parallel plates changes with the changing distance between plates. The accuracy of this AE detection method is higher than many other techniques and capacitance based AE sensors are used for calibrating other AE sensors. However, capacitance type displacement sensors for AE detection are very sensitive to the sensor position and surface mounting. Thus, they are not suitable for machining process monitoring where the operating environment is usually quite severe on the sensor [17].

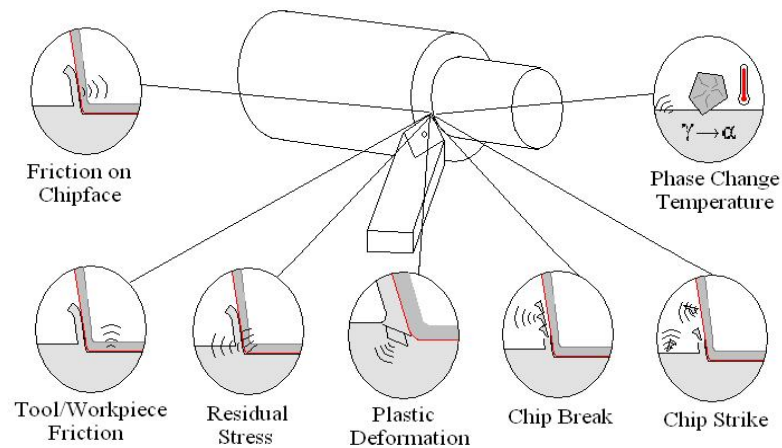


Figure 1.5: Sources of AE in machining [16].

Another sensing method for AE detection is the application of a piezoelectric thin film sensor deposited on a shim and located between the cutting insert and the tool holder. This type of AE sensor is reported to have advantages over commercially available AE sensors. It is located close to the cutting process zone and is characterized by a very large frequency bandwidth. Good signal quality has been reported, particularly in the high frequency range, with less interference and lower geometrical propagation loss and absorption rate [18]. An alternative approach using fiber optics was investigated [19] [20]. This sensing method has reported advantages over conventional AE sensors such as a broader bandwidth, flat frequency response and absolute calibration. More importantly, the fiber optic interferometer is a noncontact method of signal transmission from source to sensor. The latter two methods have largely been developed in the laboratory and have not been significantly used in industrial applications.

Signal transmission via a coupling fluid is possible due to the high frequency and low amplitude nature of AE. Due to the fact that the AE sensor is located on the coolant supply nozzle, the coolant can be used as transmission path [21]. A nonintrusive coupling fluid was used to couple the AE sensor to the spindle drive shaft [22]. These signal transmission methods had a distinct advantage for rotating tools such as in milling and drilling. Various other methods of signal transmission from AE sensor to AE coupler/signal processor are common to other sensing applications, including slip rings, inductive coupling, and radio frequency transmission [21][22]. Aspects of AE signal processing in machining were investigated and it was proposed that in the machine tool environment the AE signal is repeatedly reflected from the inner surfaces of the structure where the sensor is mounted [23]. This resulted in prolonged duration of the signal recorded by the sensor. The further the sensor is placed from the AE source, the greater the signal attenuation. This has significant implications on measuring AE during machining. If the AE sensor is mounted on the workpiece side, the changing distance between the sensor and the source during machining is a factor that requires consideration [24].

Vibration sensor types

A large variety of sensing principles are used for sensing vibrations. However, piezoelectric transduction is the most common type in vibration sensing in machining processes. Vibrations that occur during metal machining can be divided into two groups: (i) dependent and (ii) independent of the cutting process. These two groups are not mutually exclusive. Vibration independent of metal cutting include forced vibration caused by the environment of machining, i.e. other machines or machine components, e.g. vibration transmitted through foundations, unbalance of rotating parts, inertia forces of reciprocating parts and kinematic inaccuracies of drives. Furthermore, vibration dependent on metal cutting can demonstrate a number of characteristics as a function of the process, e.g. interrupted cutting. The varying cutting forces that occur during metal cutting may result from non-homogeneity and properties variations in the work material. Tool engagement conditions during machining play a notable role in the vibration produced. The self-excited vibration characteristic known as chatter is the most renowned type of vibration in machining and is detrimental to surface finish and tool life. Chatter mainly occurs due to the waviness regeneration caused by the interaction between material surface and tool at particular spindle rotational frequencies, and by mode coupling where relative vibration between workpiece and tool occurs concurrently in two directions in the cutting [3].

1.3.4. Advanced Signal Processing

Advanced signal-processing aims at extracting significant features that relate to specific process conditions. Generally, it is acknowledged that reliable process condition monitoring based on a single signal feature (SF) is not feasible. Therefore, the calculation of a sufficient number of SFs related to the process conditions [25] [26] [27] is a key issue in machining monitoring systems. This is obtained through signal processing methods that are performed successively in stages as shown in Figure 1.6.

First comes the pre-processing stage (filtering, amplification, A/D conversion, and segmentation) that occasionally includes signal transformation into frequency or time–frequency domain (Fourier transform, wavelet transform, etc.). The next stage is the extraction of signal or signal transform features changing with specific process conditions. There are many diverse signal features coming from different sensor signals, but most cannot be easily related with the process being monitored. Thus, the selection of the nature of the signal feature is of critical importance. Identified relevant features are finally integrated into the process condition diagnosis system, the decision-making system.

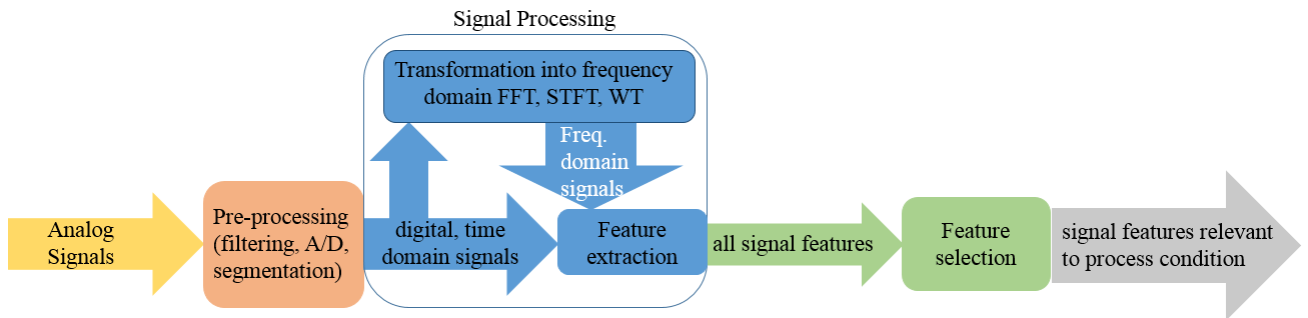


Figure 1.6: Signal processing scheme [28].

Signal pre-processing

Analog signals, directly out of the sensor, usually cannot be directly connected to the A/D converter. Before this stage, the analog signal needs to undergo pre-processing by a conditioner specific to the sensor (piezotron coupler, charge amplifier, etc.). A typical example is the procedure of analog AE signal pre-processing that follows the pattern schematically shown in Figure 1.7.

Usually, the AE sensor of piezoelectric nature is placed as close as possible to the cutting zone, e.g. on the tool shank, the tool post, the headstock or the spindle. Because of its high impedance, the sensor must be directly connected to a buffer amplifier that converts the charged signal from the sensor into a proportional voltage signal. This is typical also of other piezoelectric sensors such as dynamometers or accelerometers. The analog signal should be filtered to keep it within the range of the frequency response of the sensor, suppress high frequency noise or continuous biases. The filtered signal is then subjected to further processing and/or recording. The frequency range of the raw AE reaches 1 MHz (typically 80–700 kHz). Therefore, dealing with such signals requires a high sampling frequency (>1 MHz) and large memory resources with high computing costs. Thus, in numerous cases, the AE signal is demodulated and the Root Mean Square (RMS) of the signals is calculated (AE_{RMS}) to obtain a low frequency variable, which can be further processed with cheaper signal processing devices [3].

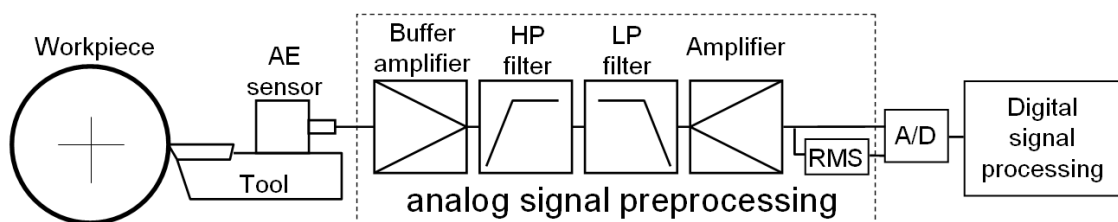


Figure 1.7: Typical measuring chain for AE detection during machining [3].

The integration time constant of the RMS converter should be carefully selected. This selection depends on the subsequent SF extraction process. Signal averages can be calculated as well as other features such as burst rate, event counts, etc. In such cases, the integration time constant should be ten times shorter than the typical burst duration, which is

approximately 2 ms [23]. The AE energy from the cutting zone can be significant. Because of the pre-processing units characteristics, these high amplitude signals may cause overloading of the buffer amplifier and signal saturation. High-pass filtering of saturated signals results in temporal vanishing of the signal value [29]. This can often result in misleading data evaluation. It should be noted that this signal distortion cannot be detected in the AE_{RMS} signal and, in this particular case, such signals must be considered completely distorted and useless. To avoid these problems, the gain of the buffer amplifier should be as small as possible and any further necessary amplification should be done after signal filtering. This is critically important when AE_{RMS} is used instead of AE_{raw} [29]. Just before conversion into the digital form, for the highest possible accuracy, the signal is usually amplified so that the signal's maximum voltage range equals the maximum input range of the A/D converter. The digital signal is often subjected to further pre-processing. Digital filtering reduces frequency bands not correlated with the monitored process or extracts information necessary for specific pattern recognition stages. For example, while using a spindle-integrated force sensor system on a machining center, when the spindle speed harmonics coincide with the spindle natural modes, the cutting force signals are distorted. One type of filters, the Kalman filters, eliminate the influence of structural modes on force measurement and significantly increase the frequency bandwidth of the force measurement system [30]. In many applications, a digital signal is filtered to prevent high frequency noise and signal oscillations due to transient mechanical events [31][32].

Another sensor signal pre-processing method is segmentation. Signal information should be extracted when the tool is actually removing metal in a steady state, since only this signal portion contains information about the process conditions [33][34]. Sensor features (SF) were calculated from force samples in one spindle rotation, instead of one tooth period, to reduce the influence of run out [35]. Despite constant cutting conditions in single micro-milling cut, AE was not constant; thus, separate SFs were calculated for all the cut and for the 1st and the 2nd third of the cut [36].

Features extraction in time domain

From the detected sensor signals, SFs that can describe the signal adequately and maintain the relevant information about the process conditions need to be extracted.

There are several SFs that can be extracted from time domain signals. The most common are:

- (i) arithmetic mean, average value, magnitude [31][35][37][38][39][40][41][42][43][44][45];
- (ii) effective value (root mean square – RMS) [31][35][37][39][40][41][43][45][46];
- (iii) variance (or standard deviation) [31][32][38][39][40][46][47];
- (iv) skewness [32][39][40][41][42][43][47];
- (v) kurtosis [32][39][40][41][42][43][47][48];
- (vi) signal power [33][43][47];
- (vii) peak-to-peak, range, or peak-to-valley amplitude [29][31][32][37][39][41];
- (viii) crest factor [31][37][41][45][47];
- and (ix) ratios of the signals, signal increments [37][49];

Acoustic emission time domain features.

Some features are applicable only to vibration and AE signals:

- (a) pulse rate: number of times AE_{raw} signal crosses the threshold level [26][29][45][46][50];
- (b) pulse width: the percentage of time during which AE_{raw} remains above the threshold level [29][50];
- (c) burst rate number of times AE_{RMS} signal exceeds preset thresholds per second [26][29][36];
- and (d) burst width – percentage of time AE_{RMS} signal remains above each threshold [29][50].

1.3.5. Monitoring scopes

In this section, a survey of applications related to the main goals of advanced monitoring of machining operations is presented.

Chip condition classification

Filtered AE spectrum components was used for chip form classification [51]. A method of chip disposal state monitoring in drilling was proposed based on spindle motor power features [38]. Wavelet packet decomposition and spectral estimation of cutting force signals was applied for chip form recognition [52][53][54]. A variety of sensors was used to obtain stable clusters of chip form under varying dry cutting conditions through geometric transformations of the control variables: they aimed at recognizing chip entanglements, chip size (including continuity), and chip shape [55]. A laboratory system for automatic chip breaking detection via frequency analysis of cutting forces was developed and tested [56].

Residual stress assessment

The approach of sensor fusion during the turning of Inconel 718 nickel alloy was used [28]. The multiple sensor monitoring system, equipped with cutting force, acoustic emission, and vibration sensor units was employed in association with advanced procedures for signal analysis, sensor fusion and cognitive decision making for residual stress evaluation. Two signal processing and feature extraction methodologies, based respectively on sensory data statistical evaluation, Principal Component Analysis, and Wavelet Packet Transform [1] were applied to the sensor signals generated during experimental turning tests. The extracted features were combined into sensor fusion input feature vectors to be fed to neural network based pattern recognition paradigms for decision making on machined surface integrity in terms of residual stress conditions. The influence of the cutting process parameters on machining performance and surface integrity generated during the dry turning of Inconel 718 and austenitic stainless steel AISI 316L with coated and uncoated tools was studied [57]. Also, the process was modelled for the prediction of the tensile residual stress using a three-dimensional finite element model. The use of on-line monitoring systems with process-integrated measurement of acoustic emission to evaluate hard turning and grinding processes is described [58]. The correlation between acoustic emission signals and subsurface integrity is determined to analyze the progression of the processes and the workpiece quality.

Surface integrity

Cutting parameters and two cutting force components were applied for online estimation of surface finish and dimensional deviations [59]. A statistical approach was employed to correlate surface roughness and cutting force in end milling operations [44]. A method of surface roughness prediction was developed in turning based on cutting parameters and FFT analysis of tool vibrations [60]. Singular spectrum analysis is used to decompose the vibration signals for in-process prediction of surface roughness in turning [61]. Time series analysis of vibration acceleration signals measured during cutting operations for real-time prediction of surface roughness were investigated [62]. A trial to correlate the quality of the machined surface after broaching, in terms of geometrical accuracy, burr formation, chatter marks and surface anomalies, and the output signals from multiple sensors: AE, vibration, cutting force; the former proved efficient to detect small surface anomalies such as plucking, laps and smeared material was performed [63]. The sensitivity of a broad range of AE parameters to white layer, surface finish and tool wear in hard machining: AE_{RMS} , frequency and count rate have good correlation with white layer formation and may be used to monitor surface integrity factors was investigated [45]. AE signal analysis was applied to recognize grinding burns in cylindrical plunge grinding processes [46]. A method for in process surface roughness prediction based on the displacement signal of spindle motion was developed [64]. Using AE signals backed up by cutting force data, it was reported on process monitoring to detect surface anomalies when abusively broaching and milling difficult-to-machine aerospace materials [65][66]. It is reported the dynamics of broaching of complex part features: force and acceleration signal analysis revealed that damped coupled vibrations, resulting in tilted chatter surface marks, occur due to specific geometry of cutting edges that enable coupling of 3D vibrations [67]. The detection of workpiece surface discontinuities, plucking, and smearing is attempted through an array of 3 AE sensors during multiple cutting edge machining [68][69]. The effect of cutting speed and feed rate on the quality features of drilled holes in carbon fiber composites (delamination, geometric errors, surface finish) by recording cutting forces with a dynamometer and inserting two K type thermocouples inside the drill is investigated [70].

1.3.6. Decision making support systems and paradigms

The role of cognitive computing methods employed in the implementation of intelligent sensors and sensorial systems is fundamental in monitoring and control activities for modern untended manufacturing systems [71]. Decision-making were developed using a conspicuous number of schemes, techniques and paradigms to support functional systems to come to a conclusion on machining process conditions based on sensor signals data features.

Neural Networks

In computer science and other related fields, artificial neural networks are computational models inspired by animals and humans central nervous systems (in particular the brain) that are capable of machine learning and pattern recognition. They are usually

presented as systems of interconnected "neurons" that can compute values from inputs by feeding information through the network. It is distributed over several simple interconnected processing elements, called neurons or nodes, which operate in parallel [72]. A NN provides a mapping through which points in the input space are associated with corresponding points in an output space on the basis of designated attribute values, of which class membership can be one. Usually, a neural network is trained and adjusted so that a particular input gives a specific output. Comparison is done between the obtained output and the target. Based on this comparison, the neural network is adjusted. Several input/target pairs are required to train a neural network [73]. This method is known as supervised training. Other NN are trained in an unsupervised mode where only the input patterns are provided during training: the NN learns automatically to cluster them in groups with similar features. NN can capture domain knowledge from examples, do not archive knowledge in an explicit form such as rules or databases, can readily handle both continuous and discrete data, and have a good generalization capability [74][75].

Supervised learning

One of the supervised learning paradigms that has been very popular for their performance is the back propagation (BP) NN paradigm, which is a multiple-layered feed forward (FF) NN [72]. Conventional training of FF BP NN very soon leads to overtraining and deterioration of the NN response [50]. Furthermore, training of these NN depends very much on the initial weight values. A good way to obtain satisfactory results is to modify the weight system and to introduce random distortions to that weight system, which efficiently pushes the NN out of local minima of testing errors. An even more effective method is to apply temporary shifts in the weights, alternately negative and positive.

This leads to a balance in the NN between training and testing errors and reduces notably the number of hidden nodes. Furthermore, different supervised NN approaches are also considered due to their use in decision making during monitoring of machining: probabilistic NN (PNN) [76] recurrent NN (RNN) [77][78][79], artificial cellular NN (ACNN) [80], fuzzy logic NN (FLNN) or neurofuzzy systems (NFS) combining NN and FL methods to integrate the benefits of both paradigms [81].

Unsupervised learning

Opposingly, in unsupervised learning, only input stimuli are introduced to the NN which organizes itself internally so that each hidden processing element responds strongly to a different set or closely related group of stimuli. These sets of stimuli represent clusters in the input space which typically stand for distinct real concepts. Among unsupervised learning paradigms, the self-organising map (SOM) NN has been largely used for their performance [82]. The SOM NN creates a 2D feature map of input data so that order is preserved: if two input vectors are close, they will be mapped to processing elements that are close together in the 2D layer that represents the features or clusters of the input data.

NN applications to sensor monitoring of machining

NN have been used in several applications in sensor monitoring of machining processes. In [83], automated classification of broaching tool conditions utilizing cutting force data using PNN is described. A force sensor was used to monitor the cutting forces during the experiments. The experimental trials used short broaching tools to simulate the roughing stage of industrial broaching and were carried out in order to produce square profile slots while detecting cutting force signals. The used broaching tools had cutting teeth in different conditions: fresh, worn, chipped tooth, broken tooth in order to reproduce real industrial tool failures, where both tool wear and single tooth chipping or breakage may randomly occur. The push-off force F_y was selected as the most sensitive to tool conditions. Tool failure recognition was based on the extraction of a set of N characteristic points from the F_y plot by repetitive selection of local maxima to construct N -elements feature vectors (pattern vectors). Pattern vectors for different tool conditions were used as inputs to a PNN with 4 tool state classes: fresh, worn, chipped, broken. The success rate achieved was as high as 92%. A scheme of the tool failure recognition paradigm is shown in Figure 1.8.

Several works, [84][85][86][87][88], use NN with simple architecture for the evaluation of tool wear in turning. Features from the wavelet representation of AE signals were related to flank wear [84]. Using RNN data processing, accurate flank wear estimations were obtained for the operating conditions adopted in the experimentation tests [85].

Fractal dimensions were used as input features to a RNN for flank wear land estimation [86][87]. The development of this estimator is composed of four stages: (i) signal representation, (ii) signal separation, (iii) feature extraction, and (iv) state estimation (flank wear land). In stage (i), a compact Suboptimal Wavelet Packet Representation (SWPR) [85], superior to other wavelet-based signal representation schemes, was used. In stage (ii), a method for suppressing noise components from measured time series data, called Modified Wavelet Method (MWM) [88], was selected for signal separation due to its high performance.

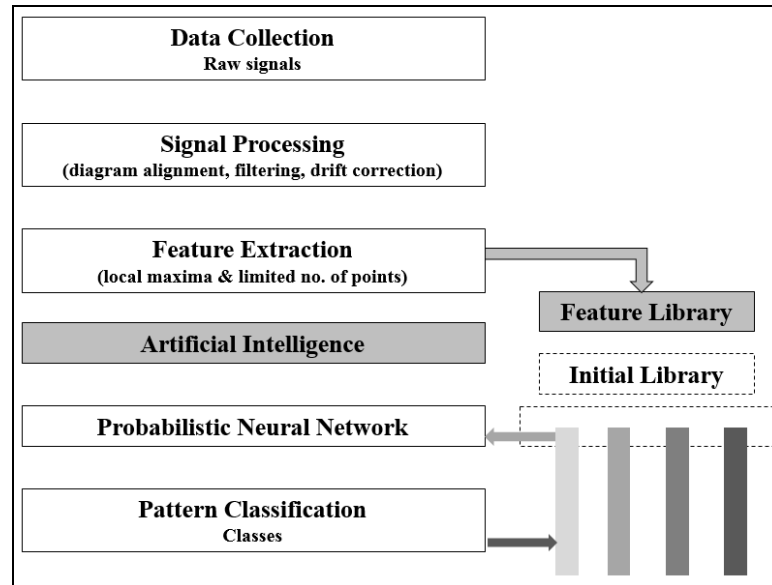


Figure 1.8: Schematic of the process condition recognition system [3].

Combining cutting force and vibration signals, a 4D time series vector was formed composed of the extracted features, which are the capacity, correlation and information fractal dimensions. A trained RNN was used to relate the extracted features to the flank wear land knowing that the trained RNN out-performed earlier tool wear estimators in terms of architecture simplicity and estimation accuracy. In able to be able to early detect undue tool wear and related machining process faults, this estimator may be used for real-time flank wear estimation at time epochs of few milliseconds, due to the high signal sampling rate [86].

Industrial needs were put under particular attention:

- (a) no reduction in machine stiffness;
- (b) compatibility with pallet and tool changers;
- (c) no restriction on tools, parts and cutting parameters;
- (d) robustness against sensing units failures;
- and (e) independence from cutting conditions and system dynamics.

To evaluate the system capability for a broad application range, different test setups with diverse milling machines, toolings, sensor systems and work materials were used. A NN approach was used for decision making, comprising an ACNN [80], applied to acceleration signals and a fuzzy NN [81] for axial force signals. Good levels of NN accuracy were obtained with all single sensor signals.

To realize the concept of multi-sensor chatter detection, the NN outputs for each single sensor signal were combined through:

- (i) linear combination of single sensor chatter indicators;
- (ii) a separate NN for multi-sensor classification;
- (iii) fuzzy logic classification (Sugeno fuzzy model);
- and (iv) statistical inference classification based on conditional probability, i.e. the probability that the system is unstable for a specific combination of single chatter indicators.

The accuracy of the first three approaches was very high: 95–96%. But residual accuracy in case of sensing unit malfunctions dropped notably: 50–75%. The behavior of the fourth approach was quite different: accuracy was slightly lower, 94%, but insensitivity to malfunctions was extremely robust: 90–92%. Thus, the statistical inference multi-sensor chatter indicator (example shown in Figure 1.9), combining NN data processing and statistical methods to achieve both high accuracy and high robustness, was assessed as the most suitable for industrial milling applications. A sensor monitoring method, based on spindle motor power sensing and NN processing, was evaluated for chip disposal state detection in drilling [89]. Spindle motor power measurements have the advantage of being easily realized during machining. From them, selected features such as variance/mean, mean absolute deviation, gradient, and event count were calculated to form input vectors to a FF BP NN for decision making on chip disposal state. The selected features were experimentally shown to be sensitive to changes in chip disposal state and relatively insensitive to changes in drilling conditions. So, the proposed monitoring system could effectively recognize chip disposal states over a wide range of drilling parameters, even if training was carried out under diverse process conditions.

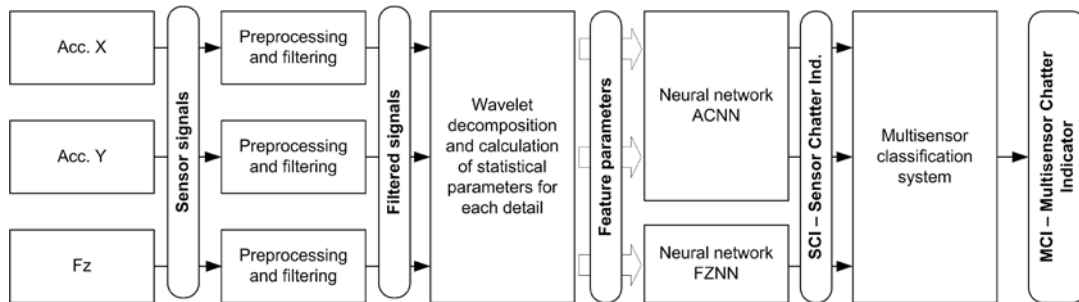


Figure 1.9: Outline of a multi-sensor chatter detection system [3].

Among the various sensing techniques, audible sound energy appears as one of the most practical ones since it can replace the traditional ability of the operator, based on his experience and senses (mainly vision and hearing), to determine the process state and react adequately to any machine performance decay [90]. This monitoring technology, however, has not been exhaustively investigated for process monitoring in machining, even though machine tool operators for real-time decision-making extensively use it. Audible sound energy generated by milling and band sawing of Al alloy and C steel under different process and tool conditions was analyzed in the frequency domain by a real-time spectrum analyzer to develop an automatic process monitoring system based on inexpensive sound sensors [91][92][93][94]. Signal analysis was carried out by suppressing the noise generated by the machine and the environment from the sound emitted during machining. Classification of audible sound SFs was performed by a NN approach that could successfully identify the process and tool conditions solely based on sound sensor monitoring.

1.3.7. Sensor fusion technology

Sensor fusion concepts and paradigms

When measuring a particular variable, a single sensory source for that variable may not be able to meet all the required performance specifications. A solution to this problem is sensor fusion that combines sensory data from disparate sources so that the resulting information is better than would be possible when these sources are used individually. The term “better” can mean more accurate, more complete, more dependable, more robust, or refer to the result of an emerging view, such as stereoscopic vision that calculates depth information by combining 2D images from two cameras at slightly different viewpoints. One can distinguish direct fusion, indirect fusion and fusion of the outputs of the former two. Direct fusion is the fusion of sensor data from a set of heterogeneous or homogeneous sensors, soft sensors, and history values of sensor data, while indirect fusion uses information sources like a priori knowledge about the environment and human input [95][96][97].

Reconfigurable monitoring system for sensor fusion research

Sensor fusion for machining process monitoring has been extensively investigated [98][99][100][101][102] within a multi-annual project aiming at the implementation of a reconfigurable multisensory monitoring system (Figure 1.10), endowed with cutting force, vibration, AE, motor current, audible sound and optical sensors, for application to diverse machining processes (orthogonal cutting, turning, milling, drilling, and broaching), work materials (steels, composite materials, Ti alloys, Ni alloys, Ni–Ti alloys) and monitoring scopes (tool wear, chip form, process conditions, work material state, and machinability assessment). Sensor signal characterization is based on frequency domain analysis, accomplishing sensor signal spectral estimation through a parametric method that allows for feature extraction from the signal frequency content [103]. In this procedure, the signal spectrum is assumed to take on a specific functional form, the parameters of which are unknown. The spectral estimation problem, therefore, becomes one of estimating these unknown parameters of the spectrum model rather than the spectrum itself [104]. From each signal specimen (measurement vector), p features $\{a_1, \dots, a_p\}$ (feature vector), characteristic of the spectrum model, are obtained through Linear Predictive Analysis (LPA) by applying Durbin’s algorithm [105][106].



Figure 1.10: Reconfigurable multi-sensor monitoring system [3].

Feature vectors are used to construct input pattern vectors for pattern recognition paradigms [107]. If single signal specimens are utilized as inputs, the feature vector and pattern vector coincide. If signal specimens' inputs come from two or more diverse sensor signals, input patterns are complex vectors integrating sensory data from diverse sources to realize the concept of sensor fusion. Three layers FF BP NN whose architecture is automatically configured as a function of the monitoring application carry out pattern recognition and decision making in the reconfigurable multi-sensor monitoring system. The constructed input pattern vectors are the input of the first NN layer that, accordingly, assumes a number of nodes equal to the number of input pattern vector elements. The hidden layer takes up a number of nodes as a function of the number of input nodes. The output layer contains one or more nodes, yielding coded values associated with the monitored process variables that need to be recognized. For NN learning, the leave-k-out method, particularly useful when dealing with relatively small training sets, is typically utilized [108]: one homogeneous group of k patterns, extracted from the training set, is held back in turn for testing and the rest of the patterns is used for training. The NN output is correct if the actual output, O_a , is equal to the desired output, O_d , $\pm 50\%$ of the difference between the numerical codes for different process conditions.

By setting error $E = (O_a - O_d)$, process conditions identification is correct if $-0.5 \leq E \leq +0.5$; otherwise, a misclassification case occurs. The ratio of correct classifications over total training cases yields the NN success rate.

Sensor fusion application to machining process monitoring

The NN pattern recognition paradigm of the reconfigurable multi-sensor monitoring system proved able to effectively realize the concept of sensor fusion for a broad range of machining process monitoring applications, yielding satisfactory results also under unfavorable situations by synergically combining the knowledge extracted from multiple sources of information. In [100][109][110] system was applied to process condition and machinability evaluation during cutting of difficult-to-machine materials such as Ti alloys and NiTi alloys, using cutting force and acceleration signals through both single signal and sensor fusion data analysis.

Training sets with input pattern vectors of different size and nature were built:

(a) signal specimen feature vectors of single cutting force or acceleration component: F_x , F_y , F_z , a_x , a_y , a_z ;

(b) integrated pattern vectors of the 3 cutting force or acceleration components:

$$[F] = [F_x \ F_y \ F_z]; [A] = [a_x \ a_y \ a_z];$$

(c) sensor fusion pattern vectors combining cutting force and acceleration pattern vectors:

$$[S] = [F \ A] = [F_x \ F_y \ F_z \ a_x \ a_y \ a_z].$$

The NN outputs were coded values to evaluate process condition and machinability. Results showed that the use of single component signal data as pattern inputs provided acceptable accuracy: 78–85%. If the integrated 3 acceleration or 3 cutting force components signal data are used as inputs, accuracy improves notably: 92–97%. By applying sensor fusion technology to fully combine information from cutting force and acceleration signal data, a very high accuracy is obtained: 99–100%.

Sensor monitoring during cutting of plastic matrix fiber reinforce composites was performed for consistent and reliable identification of tool state [99]. AE and cutting force signals were subjected to the NN based sensor fusion paradigm. The superior classification results found by merging cutting force and AE data stressed sensor fusion aptitude for data analysis enhancement and decision making reinforcement [52][111].

It is worth noting that the above results were achieved via sensor fusion of multimodal data which is far less common than fusion of data from the same sensor type. This highlights the NN ability to efficiently realize the concept of sensor fusion as well as to deal with incomplete or noisy data sets, yielding satisfactory results also under adverse situations by synergically combining knowledge extracted from multiple sources of information. The combination of a direct sensor (vision) and an indirect sensor (force) is proposed to create an intelligent integrated TCM system for online monitoring of tool wear and breakage in milling, using the complementary strengths of the two types of sensors [112]. For tool flank wear, images of the tool are captured and processed in-cycle using successive moving-image analysis. Two features of the cutting force, which closely indicate flank wear, are extracted in-process and appropriately preprocessed. A SOM network is trained in a batch mode after each cutting pass, using the two features from the cutting force, and measured wear values obtained by interpolating the vision-based measurements. The trained SOM network is applied to the

succeeding machining pass to estimate the flank wear in-process. The in-cycle and in-process procedures are employed alternatively for the online monitoring of flank wear. To detect tool breakage, two time domain features from cutting force are used, and their thresholds are determined dynamically. Again, vision is used to verify any breakage identified in-process through cutting force monitoring. Experimental results show that this sensor fusion scheme is feasible and effective to implement online TCM in milling and is independent of cutting conditions [3].

2. Conventional and advanced signal processing and feature extraction

2.1. Conventional feature extraction

The conventional features to be extracted from each dataset are statistical features [113], which are:

- Mean: the arithmetical average which is the central value of a discrete set of numbers;
- Variance: the measure of how far a set of numbers is spread out;
- Skewness: the measure of the asymmetry of the probability distribution of a real-valued random variable about its mean;
- Kurtosis: measure of the "peakness" of the probability distribution of a real-valued random variable;
- Energy: logarithmic energy of the distribution of a discrete data set.

From every acquired data signal, the mean, variance, skewness, kurtosis, and energy values are calculated.

This conventional feature extraction procedure is done with the help of Matlab ®.

```
clear workspace
m=mean(detected_signal);
v=var(detected_signal);
s=skew(detected_signal);
k=kurt(detected_signal);
e=energy(detected_signal);

save m, v, s, k, e;
```

2.2. Wavelet packet transform

2.2.1 Generalities

What are wavelets?

A wavelet is a wave-like oscillation with an amplitude that begins at zero, increases, and then decreases back to zero. It can typically be visualized as a "brief oscillation" like one might see recorded by a seismograph or heart monitor. Generally, wavelets are purposefully crafted to have specific properties that make them useful for signal processing [114]. Wavelets can be combined, using a "reverse, shift, multiply and integrate" technique called convolution, with portions of a known signal to extract information from the unknown signal [115]. They are mathematical functions that cut up data into different frequency components, and then study each component with a resolution matched to its scale [116]. In wavelet analysis, a 'mother wavelet' is chosen from a set of standard wavelets, and then this 'mother wavelet' is shifted and scaled in order to look like the original signal. Coefficients are used to scale and shift the mother wavelet and are capable to relate the mother wavelet with the original signal. A useful reference explaining wavelets, the different types of wavelet transforms and their uses is the wavelet toolbox manual of MATLAB ® [116].

Scaling

Scaling a wavelet simply means stretching or compressing it. The *scale factor* is often denoted by a . Taking sinusoids as an example, the effect of the scale factor is shown below in Figure 2.1.

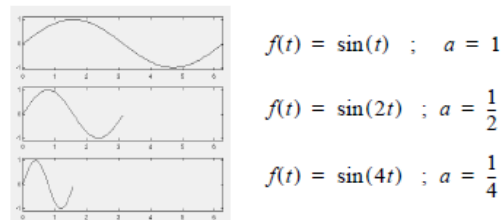


Figure 2.1: Effect of the scale factor on sinusoids.

The scale factor works exactly the same with wavelets as shown in Figure 2.2. The smaller the scale factor, the more "compressed" the wavelet.

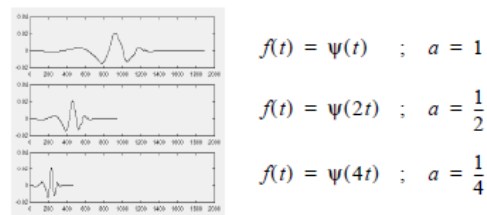


Figure 2.2: Effect of the scale factor on wavelets.

Shifting

Shifting a wavelet simply means delaying (or hastening) its onset. Mathematically, delaying a function $f(t)$ by k is represented by $f(t - k)$. Figure 2.3 illustrates a wavelet function as well as the same function delayed by a certain value k .



Figure 2.3: Wavelet function and its corresponding shifted wavelet function.

Scale and frequency

The higher scales correspond to the most “stretched” wavelets. The more stretched the wavelet, the longer the portion of the signal with which it is being compared, and thus the coarser the signal features being measured by the wavelet coefficients as shown in Figure 2.4.



Figure 2.4: Comparison between a low and high scale wavelet of the same signal.

There is a correspondence between wavelet scales and frequency as revealed by wavelet analysis:

- Low scale $a \rightarrow$ Compressed wavelet \rightarrow Rapidly changing details \rightarrow High frequency ω .
- High scale $a \rightarrow$ Stretched wavelet \rightarrow Slowly changing, coarse features \rightarrow Low frequency ω .

What is wavelet analysis?

Wavelet analysis or wavelet transform represents a windowing technique with variable-sized regions. Wavelet transform allows the use of long time intervals where we want more precise low frequency information, and shorter regions where we want high frequency information. One major advantage of wavelets is the ability to perform *local analysis*, i.e., to analyze a localized area of a larger signal.

Below is an example. A sinusoidal signal with a very small, barely visible discontinuity is considered (Figure 2.5). Such a signal easily could be generated in the real world, perhaps by a power fluctuation or a noisy switch.

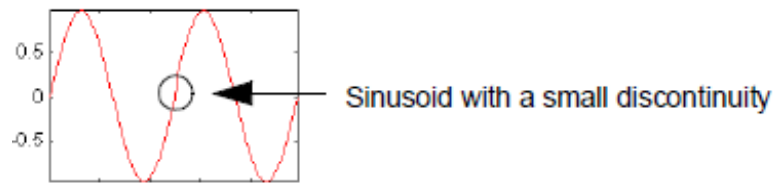


Figure 2.5: Sinusoid with a small discontinuity.

A plot of the Fourier coefficients of this signal shows nothing particularly interesting: a flat spectrum with two peaks representing a single frequency. However, a plot of wavelet coefficients clearly shows the exact location in time of the discontinuity (Figure 2.6).

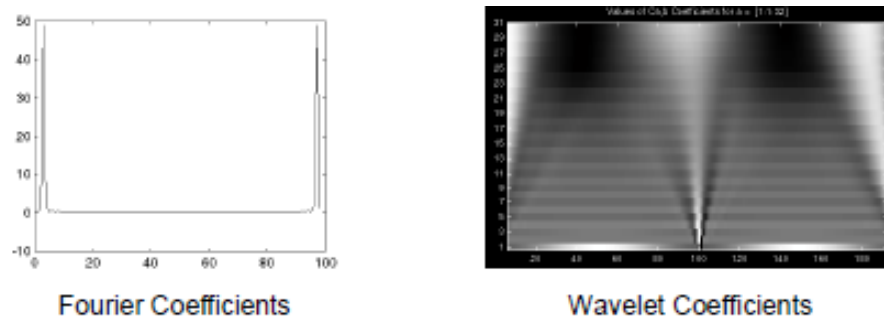


Figure 2.6: Comparison between the plot of the Fourier and Wavelet coefficients of a sinusoid with a small discontinuity.

Wavelet analysis is capable of revealing aspects of data that other signal analysis techniques miss such as trends, breakdown points, discontinuities in higher derivatives, and self-similarity. Furthermore, wavelet analysis can often compress or de-noise a signal without appreciable degradation.

The Continuous Wavelet Transform

The continuous wavelet transform (CWT) is defined as the sum over all time of the signal multiplied by scaled, shifted versions of the wavelet function, ψ :

$$C(\text{scale}, \text{position}) = \int_{-\infty}^{\infty} f(t)\psi(\text{scale}, \text{position}, t)dt$$

The result of the CWT is a matrix of wavelet coefficients, C , which are a function of scale and position. An example is shown in Figure 2.7.

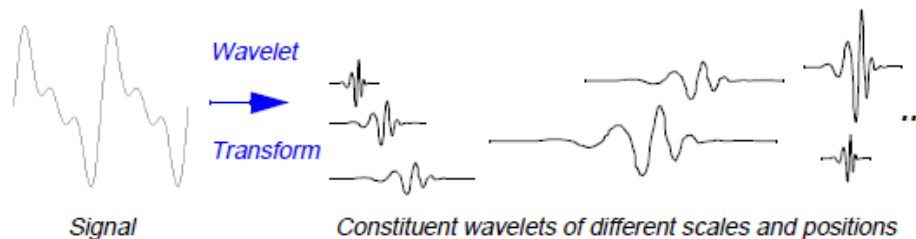


Figure 2.7: Wavelet transform of a given signal.

The Discrete Wavelet Transform

Calculating wavelet coefficients at every possible scale is a fair amount of work, and it generates an awful lot of data. Choosing only a subset of scales and positions at which to make our calculations is called the discrete wavelet transform (DWT).

One-stage filtering

This very practical filtering algorithm yields a fast wavelet transform — a box into which a signal passes, and out of which wavelet coefficients quickly emerge (Figure 2.8).

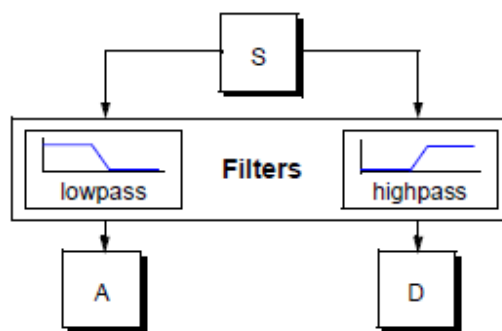


Figure 2.8: One-stage discrete Wavelet transform.

The original signal, S , passes through two complementary filters and emerges as two signals.

Unfortunately, if this operation is performed on a real digital signal, the obtained data is twice as much as the original one. To solve this problem, the notion of downsampling is introduced. This simply means throwing away every second data point.

Multiple-stage filtering

The decomposition process can be iterated, with successive approximations being decomposed in turn, so that one signal is broken down into many lower-resolution components. This is called the wavelet decomposition tree (shown in Figure 2.9).

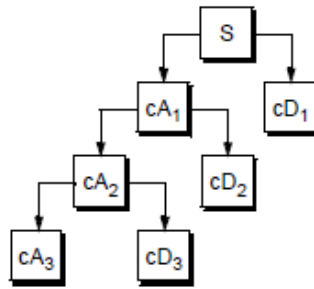


Figure 2.9: Wavelet decomposition tree.

An Introduction to the Wavelet Families

The wavelet analysis procedure is to adopt a wavelet prototype function, called an analyzing wavelet or mother wavelet [117]. Several families of wavelets have proven to be useful [116].

Haar

Any discussion of wavelets begins with Haar, the first and simplest. Haar is discontinuous, and resembles a step function (Figure 2.10). It represents the same wavelet as Daubechies db1.

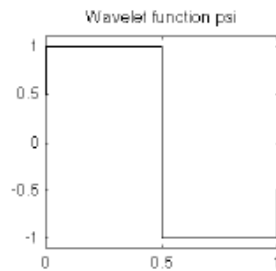


Figure 2.10: Haar wavelet.

Daubechies

The names of the Daubechies family wavelets are written dbN, where N is the order, and db the “surname” of the wavelet. The db1 wavelet, as mentioned above, is the same as Haar. Figure 2.11 illustrates the next nine members of the Daubechies family.

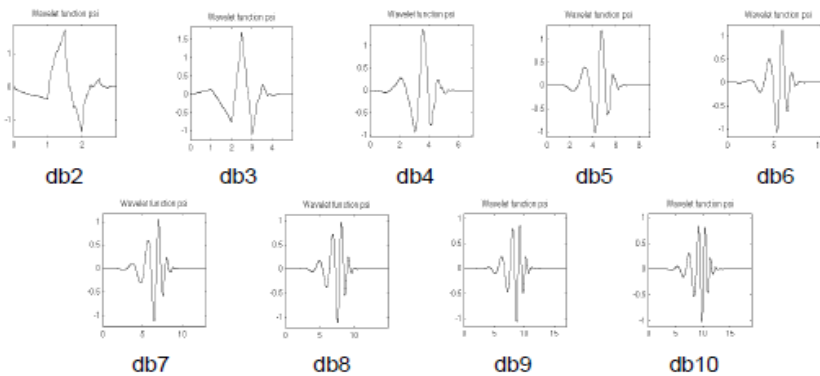


Figure 2.11: Daubechies wavelet family.

Coiflets

The wavelet function has $2N$ moments equal to 0 and the scaling function has $2N-1$ moments equal to 0. The two functions have a support of length $6N-1$. The family of coiflets is shown in Figure 2.12.

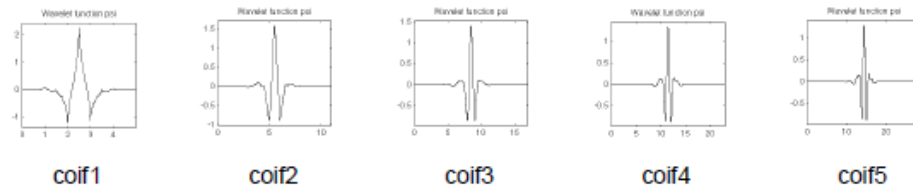


Figure 2.12: Coiflets wavelet family.

Symlets

The symlets, shown in Figure 2.13 are nearly symmetrical wavelets proposed by Daubechies as modifications to the db family. The properties of the two wavelet families are similar.

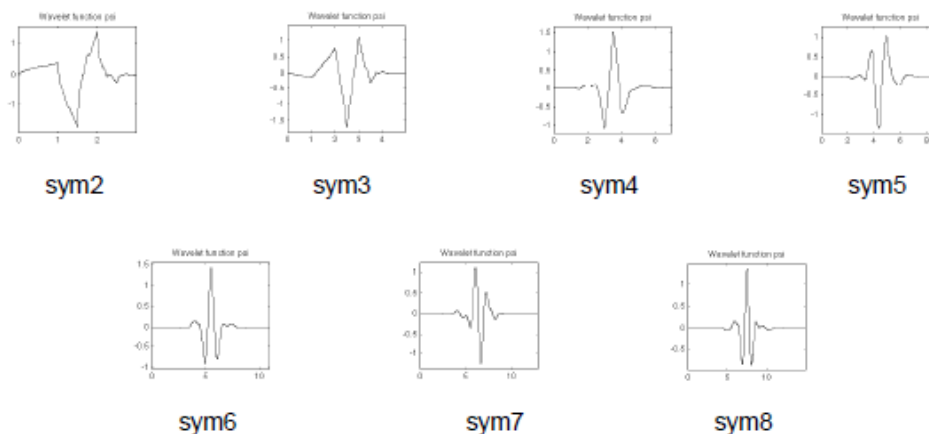


Figure 2.13: Symlets wavelet family.

Biorthogonal

Figure 2.14 illustrates the biorthogonal family of wavelets. This family of wavelets exhibits the property of linear phase, which is needed for signal and image reconstruction. By using two wavelets, one for decomposition and the other for reconstruction instead of the same single one, interesting properties are derived.

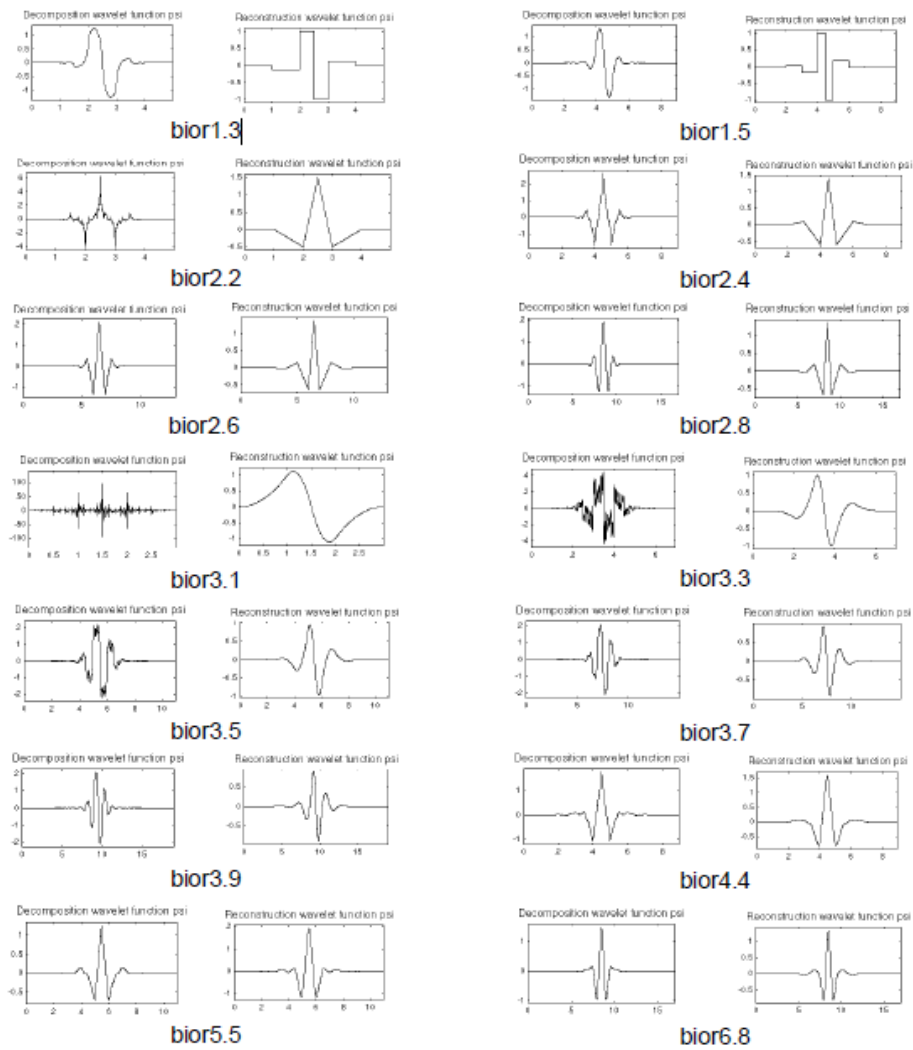


Figure 2.14: Biorthogonal family of wavelets.

Morlet

This wavelet has no scaling function, but is explicit. It is shown in Figure 2.15.

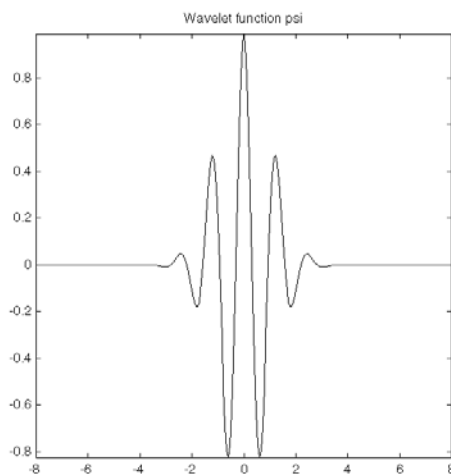


Figure 2.15: Morlet wavelet.

Mexican Hat

This wavelet has no scaling function and is derived from a function that is proportional to the second derivative function of the Gaussian probability density function. It is shown in Figure 2.16.

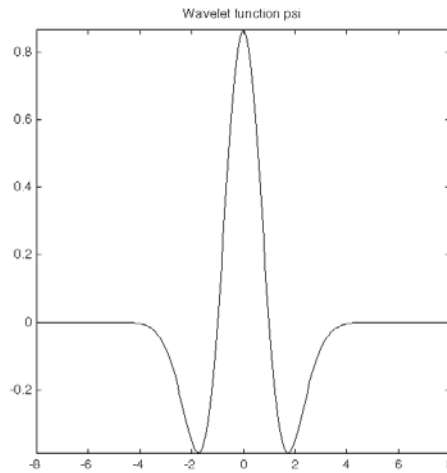


Figure 2.16: Mexican hat wavelet .

Meyer

The Meyer wavelet and scaling function are defined in the frequency domain. This wavelet is illustrated in Figure 2.17.

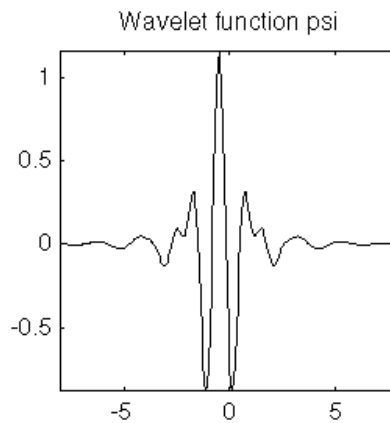


Figure 2.17: Meyer wavelet.

2.2.2 Wavelet packet decomposition

The wavelet packet decomposition method is a generalization of wavelet decomposition that offers a richer range of possibilities for signal analysis [116]. The Wavelet packet decomposition extends the discrete wavelet transform in a way that each level i consists of 2^i boxes, generated by a tree of low pass and high pass operations [118]. The wavelet transform is applied to low pass results only which is not the case of wavelet packet decomposition, which is applied to both low pass and high pass filters. In other words, the only difference between wavelet packet decomposition and the discrete wavelet transform is that in addition to the decomposition of the wavelet approximation component at each level, the wavelet detail component is also decomposed to obtain its own approximation and detail components [119].

The wavelet coefficients are obtained from the following equations [118]:

$$b_1^0 = I$$

$$b_{2^{j-1},n}^{i+1} = G * b_j^i(2n)$$

$$b_{2^j,n}^{i+1} = H * b_j^i(2n)$$

where:

- | | |
|---|------------------------|
| b: signal packet | i: decomposition level |
| j: number of coefficients in given packet | n: decomposition depth |
| G: low pass filter | H: high pass filter |
| *: denotes a convolution operation | |

In wavelet packet decomposition, a signal is split into an approximation (A) and a detail (D). The approximation is, then, itself split into a second-level approximation and detail, and the process is repeated. For an n -level decomposition, there are $n+1$ possible ways to decompose or encode the signal. This n -level decomposition is illustrated in the wavelet tree shown in Figure 2.18 below [116].

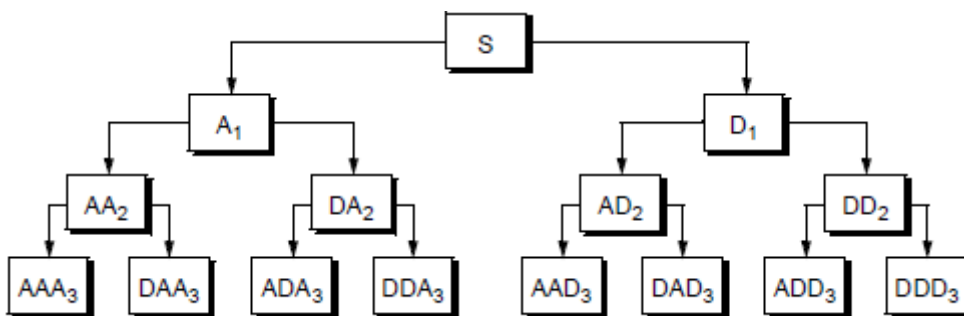


Figure 2.18: 3rd level decomposition wavelet tree [116].

The original signal can be represented as the summation of the wavelet packets. For instance, wavelet packet decomposition allows the signal S to be represented as $A_1 + AAD_3 + DAD_3 + DD_2$. This is an example of a representation that is not possible with ordinary wavelet analysis [116].

Compared to other types of wavelet transforms, wavelet packet decomposition gives more flexibility. Instead of zooming in on lower and lower frequencies, it allows focusing on any part of the time-frequency domain. The frequency increases going from left to right in the wavelet tree [115].

Each component in this wavelet packet tree can be viewed as a filtered component with a bandwidth of a filter decreasing with increasing level of decomposition and the whole tree can be viewed as a filter bank. At the top of the tree, the time resolution of the wavelet packet components is good but at an expense of poor frequency resolution whereas at the bottom with the use of wavelet packet analysis, the frequency resolution of the decomposed component with high frequency content can be increased. As a result, the wavelet packet decomposition provides better control of frequency resolution for the decomposition of the signal [120].

2.2.3 Wavelet packet transform feature extraction

The objective behind the applying the wavelet packet decomposition is obtaining characteristic features that were later on used for decision-making. The procedure described in this section summarizes the passageway from the detected sensor signals to reach the characteristic features [2]. An example shown below using the detected signals of the cutting force in the x-direction, F_x .

The starting point is setting up the F_x sensorial data table containing the n valid cutting test F_x signals (columns) composed of j samplings (rows) (Figure 2.19). In this case, the number of valid cutting tests, n , is 77 and the number of samplings, j , is 8192.

	1	2		77
F_x	T0001353	T0001354		T0001304
1	2.85×10^2	4.09×10^2		-6.11
2	3.68×10^2	4.25×10^2	...	6.11
.	.	.		.
.	.	.		.
.	.	.		.
8192	3.78×10^2	4.43×10^2		6.04×10^2

Figure 2.19: F_x sensorial data table.

The wavelet packet decomposition A was performed on the F_x signals to obtain the A packets containing the corresponding 77 A packets (columns) composed of 4099 packet coefficients (rows) (Figure 2.20).

	1	2		77
A packet of F_x	T0001353	T0001354		T0001304
1	488.52	600.94		24.57
2	545.05	599.12		-3.24
.
.	.	.		.
.	.	.		.
4099	525.36	625.36		791.07

Figure 2.20: A packet coefficients table.

For each A packet, the standard deviation of the packet coefficients was calculated and reported as row vector under the A packets table (Figure 2.21).

Std. Dev. (σ)	29.03	50.75	...	147.61
Row Vector				

Figure 2.21: Standard deviation (σ) row vector.

This row vector was transposed into a column vector representing the 77-elements standard deviation wavelet feature vector $\sigma[A]F_x$ (Figure 2.22).

	$\sigma[A] F_x$
1	29.03
2	50.75
.	.
.	.
.	.
77	147.61

Figure 2.22: $\sigma[A]F_x$ wavelet feature vector.

2.2.4 Matlab procedure

It is important to know how to perform a wavelet transform using the software Matlab ®. The procedure will go through:

- Loading a signal
- Performing the wavelet packet transform analysis
- De-noising and compressing using the wavelet packet
- Showing and exporting statistics, histograms, coefficients... for later use

Loading signal

The signal is usually stored in a text, excel ... file. The first step is to import the signal and store in the workspace of Matlab® for later processing. The table shows the Matlab® functions that can be used in order to import and load the signals.

importdata	Imports data from a file outside Matlab and stores in the workspace
xlsread	Reads and imports data from an excel file

example:

```
Fla1v1a=importdata('C:\...\Text file data\f0_08\Fla1v1a.txt');
```

The above statement imports the data from the text file **Fla1v1a.txt** and stores in the variable **Fla1v1a** in Matlab® workspace so it can be used later on. Note that, in many cases the matrix is not one-dimensional. In wavelet transformation, one dimension is studied at a time. So, it is necessary to make sure that only one dimension is analyzed and transformed at a time. The matrix can be separated into several one-dimensional matrices.

Performing a wavelet packet analysis

Now that signal is loaded to workspace, the wavelet packet analysis can be performed. Below is a table showing all the useful functions in wavelet packet analysis.

wpdec	Full decomposition of the signal
wpccoef	Extracts the coefficients of the wavelet packet at a specific decomposition

example:

```
wpt1 = wpdec(Fla1v1a',4,'db2');
cfs1 = wpccoef(wpt1,[1 0]);
```

The above statement decomposes **Fla1v1a** using the db2 as a mother wavelet up to the fourth level. The wavelet decomposition is stored in **wpt1**. Then, the wavelet coefficients of the packet (1, 0) are calculated using the **wpccoef** function and are stored in **cfs1** for later use.

Showing and exporting statistics, histograms, coefficients... for later use

This last stage can be summarized by plotting the needed information as well as exporting the required data into a file for later use. The functions usually used are listed in table below.

plot	Plots the required matrix
xlswrite	Writes the data, information... to a specific excel file

example:

```
plot(cfs1);  
s1=std(cfs1);  
v1= var(cfs1);
```

After this step, the coefficients or other data can be stored for later use or any other functions can be applied on the coefficient matrix as any other matrix. The standard deviation, variance, moment of 3rd and 4th degree, and energy can be calculated. It depends on the application and the study to be accomplished.

3. Knowledge based decision making

3.1. Neural network based pattern recognition

What are neural networks?

Neural networks are a type of artificial intelligence that attempts to imitate the way the human brain functions [121]. They are computational models and are usually presented as systems of interconnected "neurons" that can compute values from inputs by feeding information through the network [122].

Examining closely the central nervous system, it has inspired artificial neural networks where simple artificial nodes, called neurons, are connected together in a form of a network and their function mimics how a biological neural network functions [123].

The connection between the neurons is considered an adaptive weight that is adapted according to the function of each neuron. These weights can be defined as numerical parameters that are tuned by a learning algorithm [124]. Similar to biological neural networks, artificial neural networks perform functions collectively and act in parallel units [125].

Neural networks have been used to solve a wide variety of problems that are difficult to solve using ordinary problem solving methods such as rule-based programming. Some of the fields where neural networks are used are: sales forecasting, industrial process control, data validation, risk management, customer research, and target marketing.

Neural networks are composed of three layers containing nodes that are connected to each other. These three layers are: input layer, hidden layer, and the output layer. The input layer is made of a number of nodes equal to the number of elements in the input data matrix. The hidden layer is composed of a number of nodes equal to a multiple of the nodes of the input data matrix, i.e. if the input layer has 4 nodes, the hidden layer can have 8, 12, ... nodes. The number of nodes in the output layer depends on the target output.

There are three basic learning paradigms, each corresponding to a particular abstract learning task.

Supervised learning

Supervised learning is the machine-learning task of inferring a function from labeled training data, which is a set of training examples [126]. Each training example is a pair consisting of an input object and a desired output value. A supervised learning algorithm analyzes the training data and deduces a function, which can be used for mapping new examples. In optimal cases, the algorithm labels correctly unknown cases. This is done in a "reasonable" way. This is often referred as concept learning in human and animal psychology.

Unsupervised learning

Unsupervised learning is the machine-learning task of trying to find a function, the hidden structure of data without known output [127]. Having no output designated to the training data, there can be no error to evaluate a potential solution. This is what distinguishes supervised learning from unsupervised learning.

Reinforcement learning

Behaviorist psychology has inspired reinforcement learning, which concerned with how agents take action in an environment in such a way to maximize some notion of cumulative reward [128]. This type of problem is also studied in many other disciplines, such as game theory, control theory, operations research, and genetic algorithms.

What is pattern recognition?

In machine learning, pattern recognition is the process of labeling a given input value. An example of pattern recognition is classification, which attempts to assign each input value to one of a given set of classes [129].

The general aim of pattern recognition is to provide a reasonable answer for all possible inputs and to match to the "most likely" inputs, taking into account their statistical variation [130]. This is not to be confused with pattern matching algorithms, which look for exact matches in the input with pre-existing patterns.

Pattern recognition using neural networks

3-Layers feedforward backpropagation neural networks were used for pattern recognition purposes.

The term "feedforward" describes how the neural network works and recalls patterns. In this type of neural networks, the neurons are only connected forward, i.e. each layer of the neural network is connected to the next layer and not the preceding layer. An example to explain the concept are the nodes of the hidden layer, which are connected to the output layer but not to the input layer, which is in position before the hidden layer [131].

The term "backpropagation" describes the training procedure of the neural network. It is a form of supervised training of the network. It must be provided with an equal number of sample inputs and anticipated outputs. The predicted outputs are compared with the actual outputs for a given input. Through this comparison, an error is calculated. Using this calculated error, the weights of the various layers of the neural networks are adjusted backwards from the output layer to the input layer [131].

Often, the backpropagation and feedforward algorithms are used together. The feedforward neural network begins with the input layer, which may be connected to the hidden layer or directly to the output layer. If connected to a hidden layer, the hidden layer can then be connected to another hidden layer or directly to the output layer. There can be any number of hidden layers, as long as there is at least one hidden layer or output layer provided. In common use, most neural networks will have one hidden layer, and it is very rare for a neural network to have more than two hidden layers [131].

The input layer represents the conditions for which the neural network is trained. The input layer presents a pattern from the external environment to the neural network. Once a pattern is identified in the input layer, the output layer will yield another pattern. Every input neuron

should represent some independent variable that has an influence over the output of the neural network [131].

The output layer of the neural network is what actually presents a pattern to the external environment influenced by the input layer. The pattern presented by the output layer can be directly traced back to the input layer. The number of output neurons should be directly related to the type of decision-making that the neural network is to perform.

To determine the number of neurons to use in the output layer, the intended use of the neural network should be considered. If the neural network is to be used to classify items into groups, then it is often preferable to have one output neuron for each group that input items are to be assigned into [131].

Figure 3.1 illustrates a typical feedforward neural network with a single hidden layer.

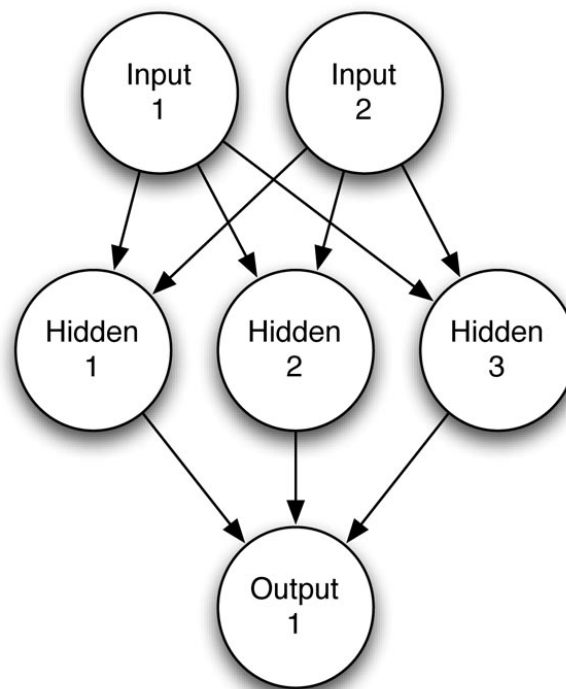


Figure 3.1: A typical feedforward neural network (single hidden layer) [133].

3.2. Training algorithm: Levenberg-Marquardt (LM)

The Levenberg-Marquardt (LM) algorithm is one of the most used algorithm in training neural networks. It is an iterative technique that locates the minimum of a multivariate function that is expressed as the sum of squares of non-linear real-valued functions [134, 135]. It has become a standard technique for non-linear least-squares problems [136], widely adopted in a broad spectrum of disciplines.

LM can be thought of as a combination of steepest descent and the Gauss-Newton method. When the current solution is far from the correct one, the algorithm behaves like a steepest descent method: slow, but guaranteed to converge. When the current solution is close to the correct solution, it becomes a Gauss-Newton method [137].

Like the quasi-Newton methods, the Levenberg-Marquardt algorithm 0 was designed to approach second-order training speed without having to compute the Hessian matrix. When the performance function has the form of a sum of squares (as is typical in training feedforward networks), then the Hessian matrix can be approximated as

$$H = J^T J$$

and the gradient can be computed as

$$g = J^T e$$

Where J is the Jacobian matrix that contains first derivatives of the network errors with respect to the weights and biases, and e is a vector of network errors. The Jacobian matrix can be computed through a standard backpropagation technique that is much less complex than computing the Hessian matrix.

The Levenberg-Marquardt algorithm uses this approximation to the Hessian matrix in the following Newton-like update:

$$x_{k+1} = x_k - [J^T J + \mu I]^{-1} J^T e$$

When the scalar μ is zero, this is just Newton's method, using the approximate Hessian matrix. When μ is large, this becomes gradient descent with a small step size. Newton's method is faster and more accurate near an error minimum, so the aim is to shift toward Newton's method as quickly as possible. Thus, μ is decreased after each successful step (reduction in performance function) and is increased only when a tentative step would increase the performance function. In this way, the performance function is always reduced at each iteration of the algorithm [139].

3.3. Matlab Procedure

Input

The input matrix dimension is $n \times m$, where:

- n rows, representing the number of samplings;
- m columns, representing the number of extracted signal features;

Target

The target vector dimensions $n \times 1$. The target elements are zeroes and ones in function of the purposes.

Output

Output represent the classification resulting from the neural network implementation, and it must be compared to the target in order to find out the success rate.

Data division

Validation and test data sets are each set to 15% of the original data. With these settings, the input vectors and target vectors will be randomly divided into three sets as follows:

- Training set: 70% of the test cases are used for training.
- Validation set: 15% of the tests cases are used to validate that the network is generalizing and to stop training before overfitting.
- Testing set: the last 15% of the test cases are used as a completely independent test of network generalization.

The process for inserting the input and target into the Neural Network and training it is shown in Figure 3.2. In 4th step of Figure 3.2, it is shown a table containing percentages. These percentages are the success rate obtained through training the neural network. The success rate (SR) is the percentage of correctly identified cases from the overall cases that the neural network achieved. There are 4 SRs, training SR, validation SR, testing SR, and the overall SR, which are respectively the SRs of the sample sets that constitute the whole dataset.

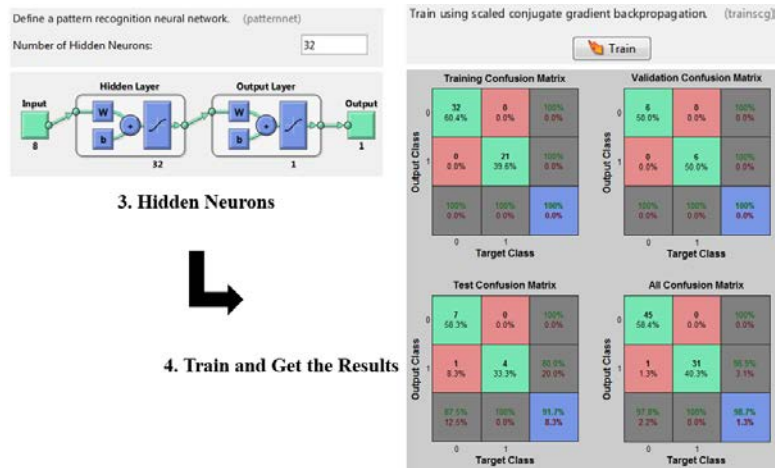
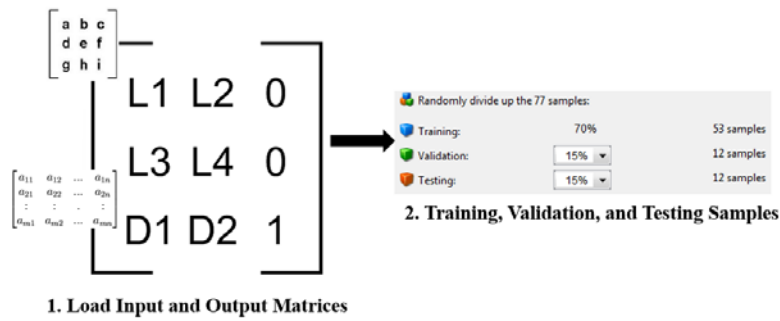


Figure 3.2: Neural network process using Matlab @.

The following MATLAB @ code is the built-in code of the function 'NPRTool' that MATLAB @ uses for training the neural network. It uses the Levenberg-Marquardt algorithm for training the neural network for pattern recognition.

```
% Solve a Pattern Recognition Problem with a Neural Network
% Script generated by NPRTOOL

inputs = input'; % input - input data
targets = target'; % target - target data

% Create a Pattern Recognition Network
hiddenLayerSize = 12;
net = patternnet(hiddenLayerSize);

% Choose Input and Output Pre/Post-Processing Functions
% For a list of all processing functions type: help nnprocess
net.inputs{1}.processFcns = {'removeconstantrows', 'mapminmax'};
net.outputs{2}.processFcns = {'removeconstantrows', 'mapminmax'};

% Setup Division of Data for Training, Validation, Testing
% For a list of all data division functions type: help nndivide
net.divideFcn = 'dividerand'; % Divide data randomly
net.divideMode = 'sample'; % Divide up every sample
net.divideParam.trainRatio = 70/100;
net.divideParam.valRatio = 15/100;
net.divideParam.testRatio = 15/100;

% For help on training function 'trainlm' type: help trainlm
```

```

% For a list of all training functions type: help nntrain
net.trainFcn = 'trainlm'; % Levenberg-Marquardt

% Choose a Performance Function
% For a list of all performance functions type: help nnperformance
net.performFcn = 'mse'; % Mean squared error

% Choose Plot Functions
% For a list of all plot functions type: help nnplot
net.plotFcns =
{'plotconfusion', 'plotperform', 'plottrainstate', 'ploterrhist',
'plotregression', 'plotfit'};

% Train the Network
[net, tr] = train(net, inputs, targets);

% Test the Network
outputs = net(inputs);
errors = gsubtract(targets, outputs);
performance = perform(net, targets, outputs)

% Recalculate Training, Validation and Test Performance
trainTargets = targets .* tr.trainMask{1};
valTargets = targets .* tr.valMask{1};
testTargets = targets .* tr.testMask{1};
trainPerformance = perform(net, trainTargets, outputs)
valPerformance = perform(net, valTargets, outputs)
testPerformance = perform(net, testTargets, outputs)

view(net) % View the Network

%Plots
figure, plotperform(tr)
figure, plottrainstate(tr)
figure, plotconfusion (targets, outputs)
figure, ploterrhist (errors)

```

The results of the neural networks computations are organized in confusion matrices.

The confusion matrix shows the percentages of correct and incorrect classifications. Correct classifications are the green squares on the matrices diagonal. Incorrect classifications form the red squares [140].

In Figure 3.3 an example of confusion matrix is reported. The confusion matrix consists of a set of success rates (SR): the training SR, the validation SR, the testing SR, and the overall SR.

All Confusion Matrix

Output Class	0	88 48.9%	1 0.6%	98.9% 1.1%
	1	2 1.1%	89 49.4%	97.8% 2.2%
		97.8% 2.2%	98.9% 1.1%	98.3% 1.7%
		0	1	
		Target Class		

Figure 3.3: Confusion Matrix example.

4. Sensor monitoring applications

Three applications of sensor monitoring of machining processes have been developed during the preparation of this PhD thesis work as summarized below.

Chip form classification

Chip form monitoring and recognition has been a major concern and of great interest for the industrial research community. The chip forms can be classified into two types: long and snarled chips which are the unfavorable form of chips and short chips which are the favorable forms of chips. A sensor monitoring approach has been developed for the identification of favorable and unfavorable chip forms during the turning of AISI 1045 carbon steel. The research activities were carried out in the framework of a bi-lateral joint project between the University of Naples Federico II, Naples, Italy, and the University of Kentucky, KY, USA.

Residual stress assessment

Residual stress is the stress present in a workpiece in the absence of any external loading and represent a datum stress over which the service load stresses are subsequently superimposed. This type of stress can have a very significant effect on the fatigue life of the final components. It would be highly desirable to create an online method that can automatically detect the level of residual stress in the machined component during the machining process. An experimental campaign was carried out for the assessment of residual stress in turning of Inconel 718 under the framework of the European project ACCENT.

Surface roughness assessment

In some manufactured components, the surface has actually functional properties such as bearing or sealing, or to have high fluid retention capabilities. Therefore, the requirements of the surface define topographic features of the component. The third application is based on the assessment of the surface roughness in polishing of AISI 52100 steel. The experimental tests were carried out under the framework of the European project IFaCOM.

4.1. Chip form classification in turning of AISI 1045 carbon steel

One of the outputs of traditional machining processes is given by the chip, which is considered a waste material. Being so, formed chips seem to be useless and of no importance. However, as a matter of fact, the chip formed is an important product of the machining process and can greatly affect the machining process as well as the quality of the machined product [141].

Chip form monitoring and recognition has been a major concern and of great interest for the industrial research community [3]. Chips can be classified into two general categories: favorable and unfavorable chip forms. The unfavorable chips are described as long and snarled chips. These unfavorable forms of chips tend to clog around the tool edge as well as the tool holder causing deterioration of the machined surface, blocking the cooling fluid, and may be harmful to the machine operator. As for the favorable chip forms, they are described as short, can be easily discarded, and do not hamper the machining process.

It would be highly desirable to develop methods capable of automatically detecting and classifying chips as favorable or unfavorable on an on-line basis during the machining process [3][142].

With the aim of implementing a sensor monitoring approach to chip form identification, experimental machining tests were conducted within a CIRP collaborative work [5] in order to detect cutting force signals from turning tests performed on 1045 carbon steel under variable cutting conditions.

The obtained cutting force signals were subjected to diverse advanced signal processing methods [54][143], including one approach based on wavelet packet transform [53][144]. This signal processing technique has been used in several different fields such as data compression, fingerprint verification, finance, speech recognition, DNA analysis, etc. [145]. It has also been used for research studies on machining process and tool condition monitoring [146].

The wavelet packet transform provides for the representation of the original time domain signal in a time-frequency domain [147]. When the wavelet packet transform is applied to a signal, the output is a “tree” of decomposition packets where each packet is composed of a series of coefficients. These coefficients are statistically processed to obtain characteristic signal features (standard deviation, variance, energy, etc.) that can be used for pattern recognition procedures [145][147].

4.1.1 Generalities: chip formation

Chip formation is part of the process of cutting materials by mechanical means using tools such as saws, lathes, and milling cutters. An understanding of the theory and engineering of this formation is an important part of the development of such machines and their cutting tools.

The formal study of chip formation was encouraged with the increase in the use of faster and more powerful cutting machines, particularly for metal cutting using the new high speed steel cutters.

Theoretical chip formation: orthogonal cutting model

Chip formation is usually described according to the orthogonal cutting model [148] shown in Figure 4.1. Although an actual machining process is three-dimensional, the orthogonal model has only two dimensions that play active roles in the analysis. The three-dimensional machining process is reduced into the a two-dimensional model for simplification purposes.

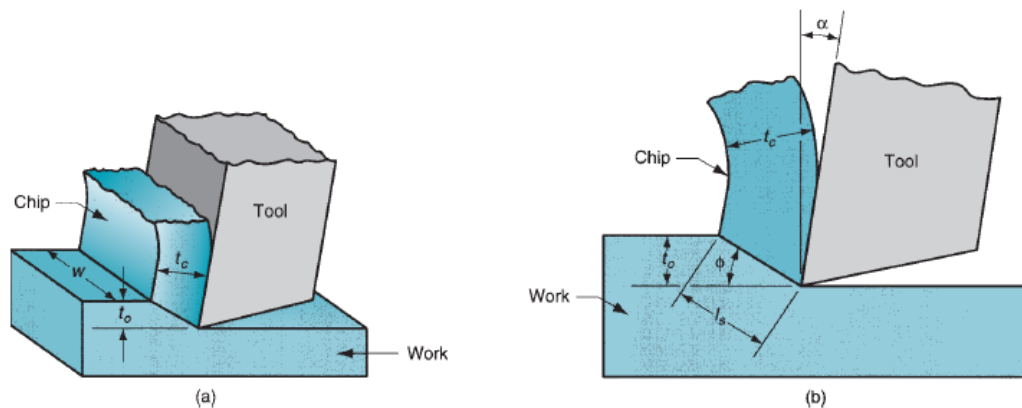


Figure 4.1: Orthogonal cutting: (a) as a three-dimensional process, and (b) how it reduces to two dimensions in the side view [148].

By definition, orthogonal cutting uses a wedge-shaped tool whose cutting edge is perpendicular to the direction of cutting speed. As the tool is forced into the material, the chip is formed by shear deformation along the plane which is called shear plane, oriented at an angle f with the surface of the workpiece. Only at the sharp cutting edge of the tool failure of the material occurs, resulting in the separation of the chip from the parent material. Along the shear plane, where the bulk of the mechanical energy is consumed in machining, the material is plastically deformed.

The tool in orthogonal cutting has only two elements of geometry: the rake and clearance angles. The rake angle, α , determines the direction in which the chip flows as it is being formed. The clearance angle provides a clearance between the tool flank and the newly generated work surface. During the cutting process, the cutting edge of the tool is positioned below the original work surface. This is the thickness of the chip prior to chip formation, denominated by t_o . As the chip is formed along the shear plane, its thickness increases to t_c .

The ratio of t_o to t_c is called the chip thickness r :

$$r = \frac{t_o}{t_c}$$

Since the chip thickness after cutting is always greater than the corresponding thickness before cutting, the chip ratio will always be less than 1.

In addition to t_o , the orthogonal cut has a width dimension w , as shown in Figure 4.1(a), even though that this dimension does not contribute much to the analysis in orthogonal cutting.

The geometry of the orthogonal cutting model allows us to establish an important relationship between the chip thickness ratio, the rake angle, and the shear plane angle.

Let l_s be the length of the shear plane. We can make the substitutions: $t_o = l_s \sin \phi$, and $t_c = l_s \cos(\phi - \alpha)$. Thus,

$$r = \frac{l_s \sin \phi}{l_s \cos(\phi - \alpha)} = \frac{\sin \phi}{\cos(\phi - \alpha)}$$

This can be rearranged to determine ϕ as follows:

$$\tan \phi = \frac{r \cos \alpha}{1 - r \sin \alpha}$$

The shear strain that occurs along the shear plane can be estimated by examining Figure 4.2(a) shows shear deformation approximated by a series of parallel plates sliding against one another to form the chip. Consistent with our definition of shear strain, each plate experiences the shear strain shown in Figure 4.2(b).

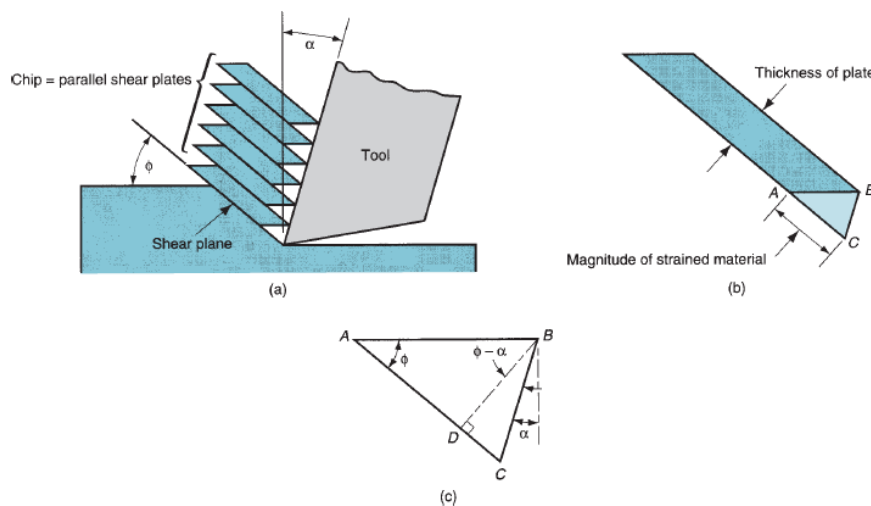


Figure 4.2: Shear strain during chip formation: (a) chip formation depicted as a series of parallel plates sliding relative to each other; (b) one of the plates isolated to illustrate the definition of shear strain based on this parallel plate model; and (c) shear strain triangle [148].

Referring to Figure 4.2(c), this can be expressed as:

$$\gamma = \frac{AC}{BD} = \frac{AD + DC}{BD}$$

which can be reduced to the following definition of shear strain in metal cutting:

$$\gamma = \tan(\phi - \alpha) + \cot \phi$$

Actual chip formation

There are differences between the orthogonal model and an actual machining model. First, the shear deformation process does not occur along a plane, but within a zone. If shearing were to take place across a plane of zero thickness, it would imply that the shearing action must occur instantaneously as it passes through the plane, rather than over some finite (although brief) time period. For the material to behave in a realistic way, the shear deformation must occur within a thin shear zone. This more realistic model of the shear deformation process in machining is illustrated in Figure 4.3. Metal-cutting experiments have indicated that the thickness of the shear zone is only a few thousandths of an inch. Since the shear zone is so thin, there is not a great loss of accuracy in most cases by referring to it as a plane.

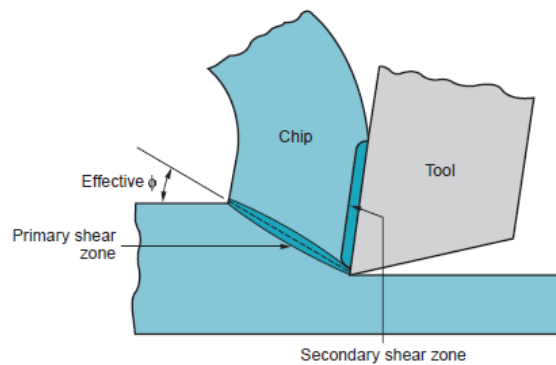


Figure 4.3: More realistic view of chip formation, showing shear zone rather than shear plane. Also shown is the secondary shear zone resulting from tool–chip friction [148].

Second, in addition to shear deformation that occurs in the shear zone, another shearing action occurs in the chip after it has been formed. This additional shear is referred to as secondary shear to distinguish it from primary shear. Secondary shear results from friction between the chip and the tool as the chip slides along the rake face of the tool. Its effect increases with increased friction between the tool and chip. The primary and secondary shear zones can be seen in Figure 4.3. Third, formation of the chip depends on the type of material being machined and the cutting conditions of the operation. Four basic types of chip can be distinguished, illustrated in Figure 4.4.

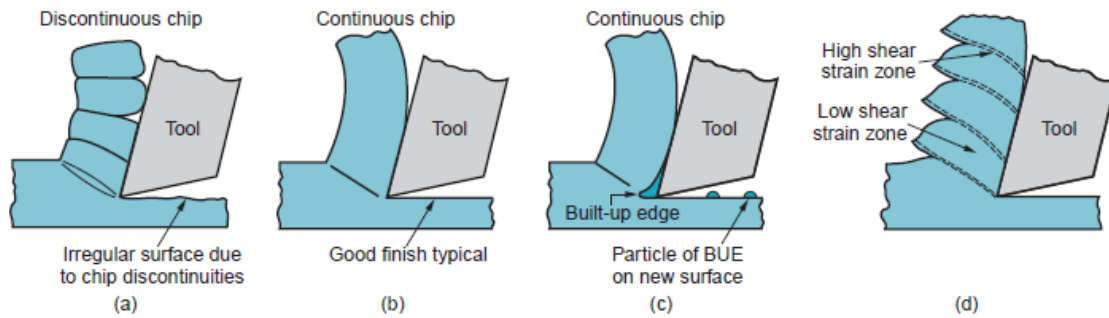


Figure 4.4: Four types of chip formation in metal cutting: (a) discontinuous, (b) continuous, (c) continuous with built-up edge, (d) serrated [148].

- Discontinuous chip (type a): When relatively brittle materials (e.g., cast irons) are machined at low cutting speeds, the chips often form into separate segments (sometimes the segments are loosely attached). This tends to impart an irregular texture to the machined surface. High tool–chip friction and large feed and depth of cut promote the formation of this chip type.
- Continuous chip (type b): When ductile work materials are cut at high speeds and relatively small feeds and depths, long continuous chips are formed. A good surface finish typically results when this chip type is formed. A sharp cutting edge on the tool and low tool–chip friction encourage the formation of continuous chips. Long, continuous chips (as in turning) can cause problems with regard to chip disposal and/or tangling about the tool. To solve these problems, turning tools are often equipped with chip breakers.
- Continuous chip with built-up edge (type c): When machining ductile materials at low-to medium cutting speeds, friction between tool and chip tends to cause portions of the work material to adhere to the rake face of the tool near the cutting edge. This formation is called a built-up edge (BUE). The formation of a BUE is cyclical; it forms and grows, then becomes unstable and breaks off. Much of the detached BUE is carried away with the chip, sometimes taking portions of the tool rake face with it, which reduces the life of the cutting tool. Portions of the detached BUE that are not carried off with the chip become imbedded in the newly created work surface, causing the surface to become rough.
- Serrated chips (or shear-localized) (type d): These chips are semi-continuous in the sense that they possess a saw-tooth appearance that is produced by a cyclical chip formation of alternating high shear strain followed by low shear strain. This fourth type of chip is most closely associated with certain difficult-to-machine metals such as titanium alloys, nickel-base superalloys, and austenitic stainless steels when they are machined at higher cutting speeds. However, the phenomenon is also found with more common work metals (e.g., steels) when they are cut at high speeds [149].

4.1.2 Chip form classification: ISO 3685, Annex G [150]

The chip formed during a cutting process has characteristics, which are related to the work material, tool material, tool geometry, condition of the cutting edges, cutting edge position and cutting data and conditions.

For any given set of conditions, the chip formation will remain unchanged unless one of the above mentioned factors changes. Observations of chip formation can therefore be a useful indicator when attempting to reproduce test conditions used in a previous test, as an indicator of changing conditions during a given tool-life test, to indicate varying stability in the cutting conditions, as an indicator of changing machinability of the work pieces or as an indicator of unexpected edge failure. The standard ISO 3685 classifies the types of chips according to their form.

It is therefore essential to be able to report characteristics of chips and their form in a consistent manner. Table 4.1 can be used, together with information on chip cross-section and length, to define chips produced. The table also includes a numeric coding system for the more commonly observed chip types.

The basic coding system is composed of two digits that relate to the basic chip characteristics, i.e. 2.2 is the code to denote a short tubular chip.

A third digit can be added to designate either the direction in which the chip flows or the mode of chip breaking, e.g. 1.3.4 denotes a “snarled ribbon chip” which flows away from the work piece in a direction opposite to the direction of feed motion. Code 6.1.5 denotes a “connected arc chip” which breaks against the transient surface of the workpiece.

Table 4.1: Chip Forms.

1. Ribbon chips	2. Tubular chips	3. Spiral chips	4. Washer-type helical chips	5. Conical helical chips	6. Arc chips	7. Elemental chips	8. Needle chips
1.1 Long 	2.1 Long 	3.1 Flat 	4.1 Long 	5.1 Long 	6.1 Connected 		
1.2 Short 	2.2 Short 	3.2 Conical 	4.2 Short 	5.2 Short 	6.2 Loose 		
1.3 Snarled 	2.3 Snarled 		4.3 Snarled 	5.3 Snarled 			

4.1.3 Experimental setup and procedure

Machine Tool

The machine utilized for the experimental campaign was a Mazak CNC turning lathe (Figure 4.5).



Figure 4.5: Mazak CNC turning lathe.

Work material

Longitudinal turning tests with cutting force signal detection were carried out on 1045 carbon steel bars for sensor monitoring based chip form recognition [52].

AISI 1045 carbon steel is a medium tensile steel supplied in the black hot rolled or normalized condition. It is characterized by good weldability, good machinability, and high strength and impact properties in either the normalized or hot rolled condition.

Table 4.2: Typical analysis in percent.

C:	0.42-0.45
Fe:	98.51-98.98
Mn:	0.60-0.90
P:	≤ 0.04
S:	≤ 0.05

Table 4.3: AISI 1045 carbon steel physical properties.

Density:	7.87 g/cm ³
Melting point range:	1150 – 1280 ° C
Specific heat:	486 J/kg·K
Average Coefficient of Thermal Expansion:	13.0 μm/m·K
Thermal Conductivity:	51.9 W/m-K
Electrical Resistivity:	1620 n.m
Curie Temperature:	751 °C

Table 4.4: AISI 1045 carbon steel mechanical properties.

At room temperature	
Ultimate tensile strength:	565 MPa
Yield strength:	310 MPa
Elongation in 50 mm:	16 %
Elastic modulus (Tension):	200 GPa
Hardness:	163 HRC

Workpiece

The experimental campaign was carried out by turning AISI 1045 carbon steel cylindrical shaft. No data on the dimensions of the shafts is available.

Cutting tool

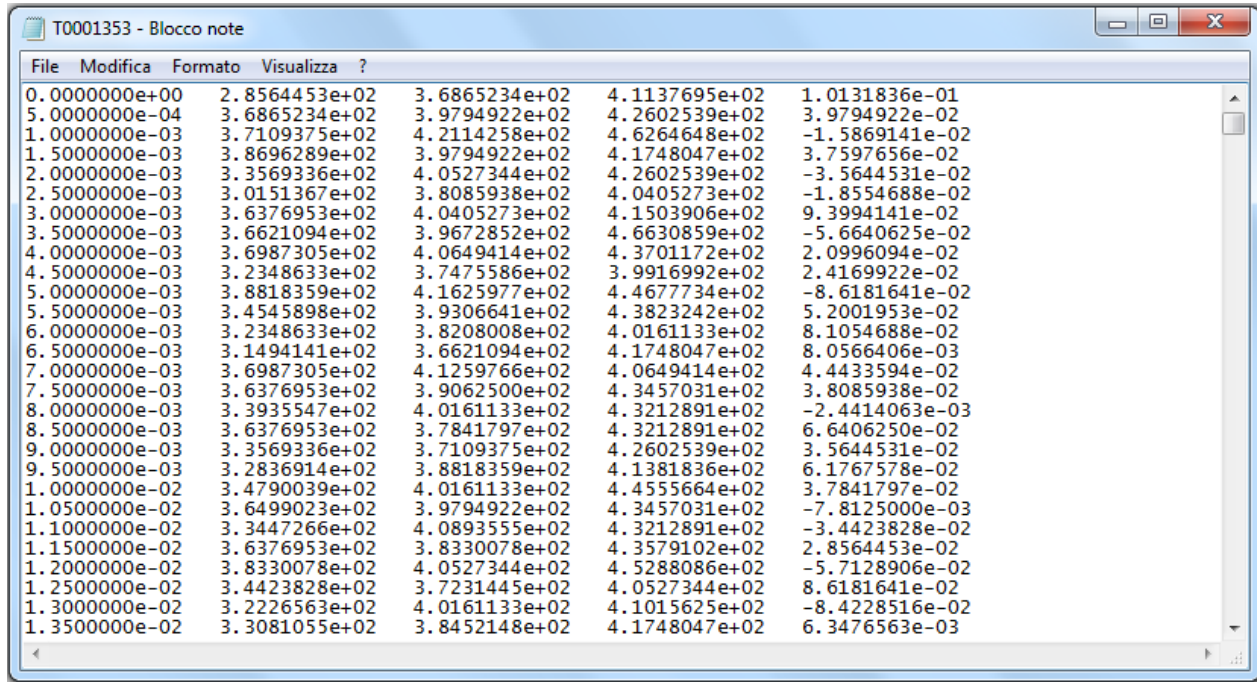
The cutting tool used was a Kennametal carbide insert mounted on a standard Sandvik tool holder (Figure 4.6).



Figure 4.6: Kennametal tool insert (model TNMG322P KC 850) mounted on a standard SANDVIK tool holder (MTGNR/L).

Experimental tests program

A Kistler dynamometer was used to provide sensor signals for the measurement, in N, of the three components of the cutting force: F_x – feed force, F_y – radial force, and F_z – cutting force. The cutting force component signals were digitized at 2000 Hz for 4.1 seconds, making up a data sequence of 8192 samplings (example shown in Figure 4.7).



File	Modifica	Formato	Visualizza	?	
0.000000e+00	2.8564453e+02	3.6865234e+02	4.1137695e+02	1.0131836e-01	
5.000000e-04	3.6865234e+02	3.9794922e+02	4.2602539e+02	3.9794922e-02	
1.000000e-03	3.7109375e+02	4.2114258e+02	4.6264648e+02	-1.5869141e-02	
1.500000e-03	3.8696289e+02	3.9794922e+02	4.1748047e+02	3.7597656e-02	
2.000000e-03	3.3569336e+02	4.0527344e+02	4.2602539e+02	-3.5644531e-02	
2.500000e-03	3.0151367e+02	3.8085938e+02	4.0405273e+02	-1.8554688e-02	
3.000000e-03	3.6376953e+02	4.0405273e+02	4.1503906e+02	9.3994141e-02	
3.500000e-03	3.6621094e+02	3.9672852e+02	4.6630859e+02	-5.6640625e-02	
4.000000e-03	3.6987305e+02	4.0649414e+02	4.3701172e+02	2.0996094e-02	
4.500000e-03	3.2348633e+02	3.7475586e+02	3.9916992e+02	2.4169922e-02	
5.000000e-03	3.8818359e+02	4.1625977e+02	4.4677734e+02	-8.6181641e-02	
5.500000e-03	3.4545898e+02	3.9306641e+02	4.3823242e+02	5.2001953e-02	
6.000000e-03	3.2348633e+02	3.8208008e+02	4.0161133e+02	8.1054688e-02	
6.500000e-03	3.1494141e+02	3.6621094e+02	4.1748047e+02	8.0566406e-03	
7.000000e-03	3.6987305e+02	4.1259766e+02	4.0649414e+02	4.4433594e-02	
7.500000e-03	3.6376953e+02	3.9062500e+02	4.3457031e+02	3.8085938e-02	
8.000000e-03	3.3935547e+02	4.0161133e+02	4.3212891e+02	-2.4414063e-03	
8.500000e-03	3.6376953e+02	3.7841797e+02	4.3212891e+02	6.6406250e-02	
9.000000e-03	3.3569336e+02	3.7109375e+02	4.2602539e+02	3.5644531e-02	
9.500000e-03	3.2836914e+02	3.8818359e+02	4.1381836e+02	6.1767578e-02	
1.000000e-02	3.4790039e+02	4.0161133e+02	4.4555664e+02	3.7841797e-02	
1.050000e-02	3.6499023e+02	3.9794922e+02	4.3457031e+02	-7.8125000e-03	
1.100000e-02	3.3447266e+02	4.0893555e+02	4.3212891e+02	-3.4423828e-02	
1.150000e-02	3.6376953e+02	3.8330078e+02	4.3579102e+02	2.8564453e-02	
1.200000e-02	3.8330078e+02	4.0527344e+02	4.5288086e+02	-5.7128906e-02	
1.250000e-02	3.4423828e+02	3.7231445e+02	4.0527344e+02	8.6181641e-02	
1.300000e-02	3.2226563e+02	4.0161133e+02	4.1015625e+02	-8.4228516e-02	
1.350000e-02	3.3081055e+02	3.8452148e+02	4.1748047e+02	6.3476563e-03	

Figure 4.7: Example of sensor signals text file of a cutting test T0001353. 2nd column represents F_x , 3rd column F_y , and 4th column F_z .

Throughout the experimental campaign, the cutting parameters were varied as follows:

- Cutting speed, $v_c = 150, 200, 250$ m/min
- Feed rate, $f = 0.1, 0.2, 0.3, 0.35, 0.4, 0.5$ mm/rev
- Depth-of-cut, DoC = 1.0, 1.2, 1.3, 1.4, 1.5 mm

By combining 3 cutting speeds, 6 feed rates and 5 depth-of-cut values, a total of 90 cutting conditions were used for sensor monitoring turning tests with generation of diverse chip forms. However, not all experimental tests provided usable cutting force signals due to errors in signal data transmission and storage.

Figure 4.8 summarizes the typology of the chip forms generated during the corresponding turning tests. The boxes barred with an X identify the cutting conditions cases for which no viable cutting force signals were acquired.

All in all, 77 valid cutting tests with variable cutting conditions and diverse chip forms were considered for the purpose of this work (Figure 4.8). The generated chip forms were grouped into two classes of favorable or unfavorable chips and classified according to Annex G of the ISO 3685 standard [150] as follows (Table 4.5).

DoC \ f	0.1	0.2	0.3	0.35	0.4	0.5
1.0	T0001353 1.3	T0001354 2.1	X	T0001356 4.1	T0001357 4.1	T0001358 4.1
1.2	T0001347 1.3	X	T0001349 6.1	T0001350 6.1	T0001351 6.1	T0001352 6.1
1.3	T0001341 1.3	X	T0001343 6.1	T0001344 6.1	T0001345 6.2	T0001346 6.2
1.4	T0001335 1.3	X	T0001337 6.1	T0001338 6.1	T0001339 6.1	T0001340 6.2
1.5	T0001329 1.3	X	T0001331 6.1	T0001332 6.1	T0001333 6.1	T0001334 6.1

(a)

DoC \ f	0.1	0.2	0.3	0.35	0.4	0.5
1.0	T0001384 1.3	T0001385 4.1	T0001386 4.1	T0001387 4.1	T0001388 4.1	T0001389 4.2
1.2	T0001378 1.3	T0001379 4.1	X	X	X	X
1.3	T0001372 1.3	T0001377 4.1	T0001373 6.2	T0001374 6.2	T0001375 6.2	T0001376 6.2
1.4	T0001366 1.3	T0001367 4.1	T0001368 6.2	T0001369 6.2	T0001370 6.2	T0001371 6.2
1.5	T0001360 1.3	T0001361 4.1	T0001362 6.2	T0001363 6.2	T0001364 6.2	T0001365 6.2

(b)

DoC \ f	0.1	0.2	0.3	0.35	0.4	0.5
1.0	T0001323 1.3	T0001324 4.1	T0001325 4.2	T0001326 4.2	T0001327 4.2	T0001328 4.2
1.2	T0001317 1.3	T0001318 4.2	X	T0001320 6.2	T0001321 6.2	T0001322 6.2
1.3	T0001311 1.3	T0001312 4.1	X	T0001314 6.2	T0001315 6.2	T0001316 6.2
1.4	T0001335 1.3	T0001306 4.1	T0001307 6.2	T0001308 6.2	T0001309 6.2	T0001310 6.2
1.5	X	X	T0001301 6.2	T0001302 6.2	T0001303 6.2	T0001304 6.2

(c)

Figure 4.8: Chip forms obtained from different combinations of feed rate and depth-of-cut values for the three cutting speeds: (a) $v_c = 150$ m/min; (b) $v_c = 200$ m/min; (c) $v_c = 250$ m/min.

Table 4.5: Generated chip forms classified per ISO 3685 standard.

Unfavourable chip form	Favourable chip form
1.3 – Snarled Ribbon 	4.2 – Short Washer Type 
2.1 – Long Tubular 	6.1 – Connected Arc 
4.1 – Long Washer Type 	6.2 – Loose Arc 

4.1.4 Sensor signal data analysis

Wavelet Packet Transform Feature Extraction

The wavelet packet transform was used to process each of the three cutting force component signals: F_x , F_y , and F_z . The mother wavelet used was a Daubechies 4 (db4); the decomposition was performed up to the 4th level, generating thirty packets for each cutting force component [52]. For every obtained decomposition packet, five statistical features were calculated: standard deviation (σ), variance (σ^2), third (σ^3) moment, and fourth (σ^4) moment, and energy ($E = \sum \log(x_i)^2$).

Thus, for each cutting test, 3 cutting force component signals \times 30 decomposition packets \times 5 statistical features = 450 wavelet packet statistical features were obtained. Then, 450 wavelet packet statistical feature vectors for pattern recognition were constructed, composed of 77 elements given by the values of one statistical feature for one decomposition packet and one cutting force component signal obtained from the 77 valid cutting tests. These 77-element vectors are called shortly “wavelet feature vectors” and each of their elements was associated to the chip form generated by the corresponding turning test.

The starting point is the set up of the F_x sensorial data table containing the 77 valid cutting test F_x signals (columns) composed of 8192 samplings (rows). The wavelet packet decomposition A was performed on the F_x signals to obtain the A packets table containing the corresponding 77 A packets (columns) composed of 4099 packet coefficients (rows). For each A packet, the standard deviation of the packet coefficients was calculated and reported as row vector under the A packets table. This row vector was transposed into a column vector representing the 77-elements standard deviation wavelet feature vector $\sigma[A]F_x$ for decomposition packet A of cutting force component signal F_x . This procedure is clearly explained and illustrated in section 2.2.3.

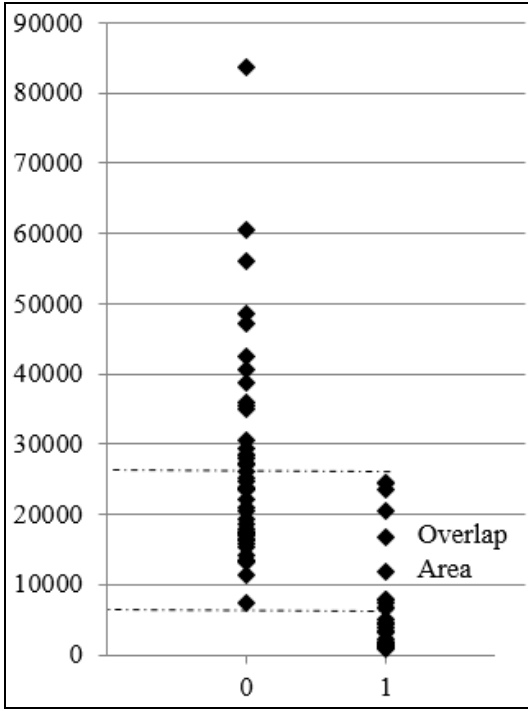
Wavelet Packet Feature Vector Selection for Sensor Fusion Pattern Recognition

Examining the constructed wavelet feature vectors, it can be noted that in all cases the elements for favorable or unfavorable chip forms in the same wavelet feature vector display an overlap of values, responsible for uncertainty in the chip form classification. Thus, the wavelet feature vectors were ranked according to the number of elements with overlapping values: the lower this number, the less the uncertainty, the higher the wavelet feature vector ranking.

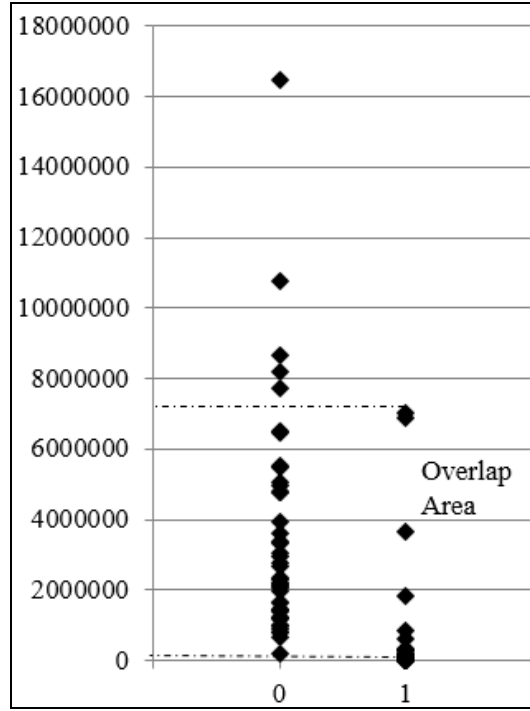
Figure 4.9 (a) shows the values of the 77-elements of wavelet feature vector $\sigma^2[\text{DAA}]F_x$ constructed with the variance of decomposition packet DAA of cutting force component signal F_x . An overlap of element values for unfavorable (“0” binary code) or favorable (“1” binary code) chip forms is clearly visible in the graph, allowing for the identification of 7 cutting tests that generate uncertainty in the classification of chip form when using $\sigma^2[\text{DAA}]F_x$: T0001356, T0001357, T0001358, T0001386, T0001388, T0001373, T0001301.

In Figure 4.9 (b), the element values of wavelet feature vector $\sigma^2[\text{DDD}]F_x$ made of the variance of decomposition packet DDD of cutting force component signal F_x are shown. In this case, the overlap of favorable/unfavorable chip form cases is verified for 7 cutting tests: T0001356, T0001357, T0001358, T0001385, T0001386, T0001379, T0001382.

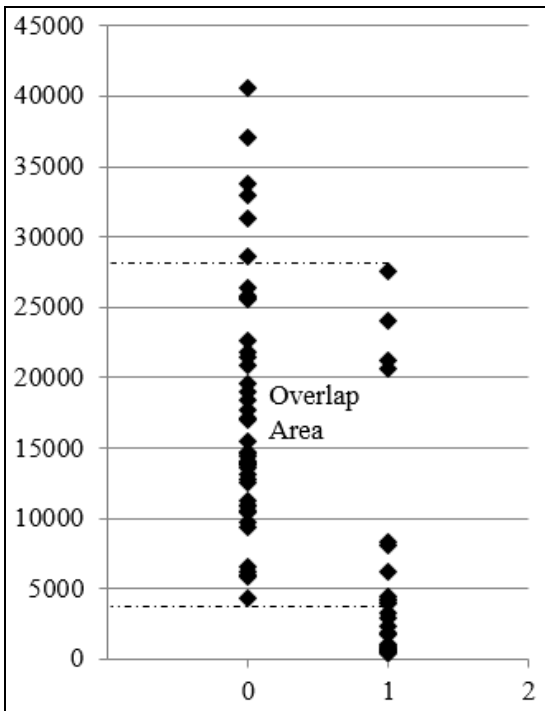
Figure 4.9 (c) reports the element values of wavelet feature vector $E[\text{AAAA}]F_x$ composed of the energy of decomposition packet AAAA of cutting force component signal F_y , showing an overlap of favorable/ unfavorable chip form cases for 5 cutting tests: T0001387, T0001388, T0001373, T0001361, T0001324.



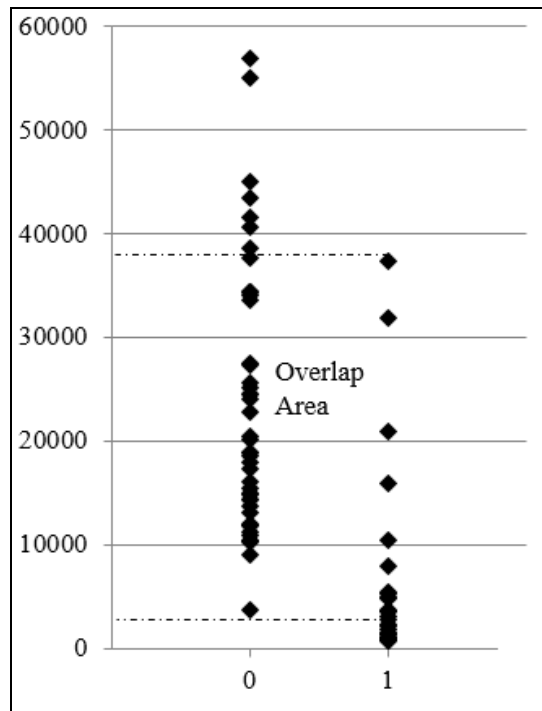
(a)



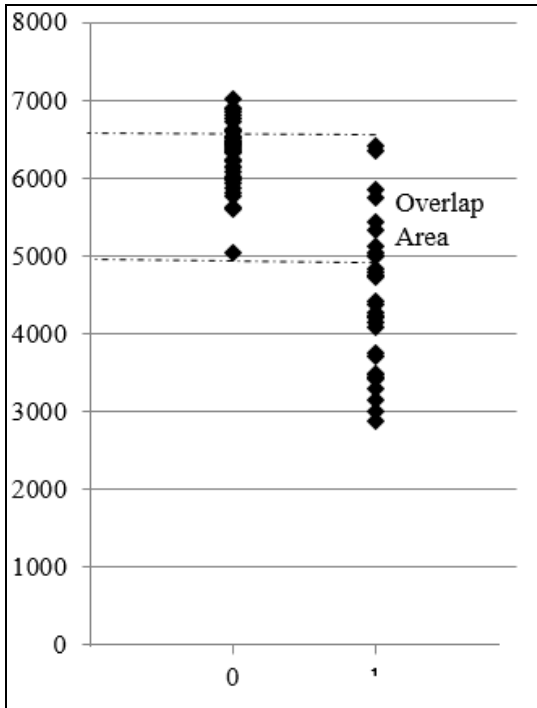
(b)



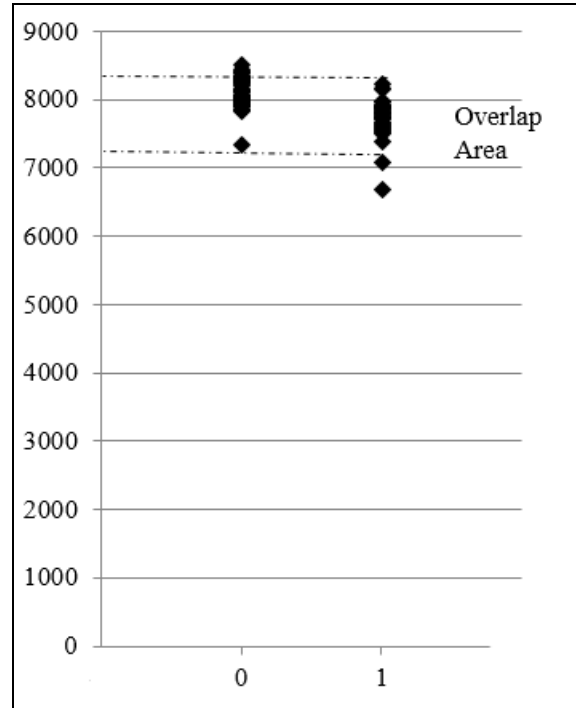
(c)



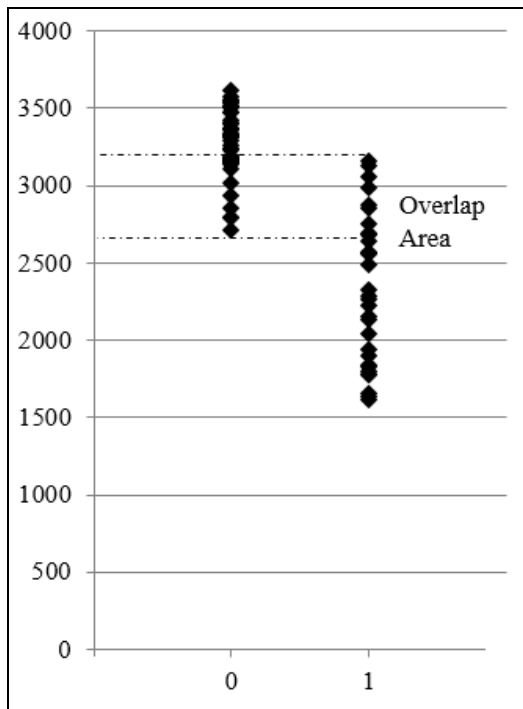
(d)



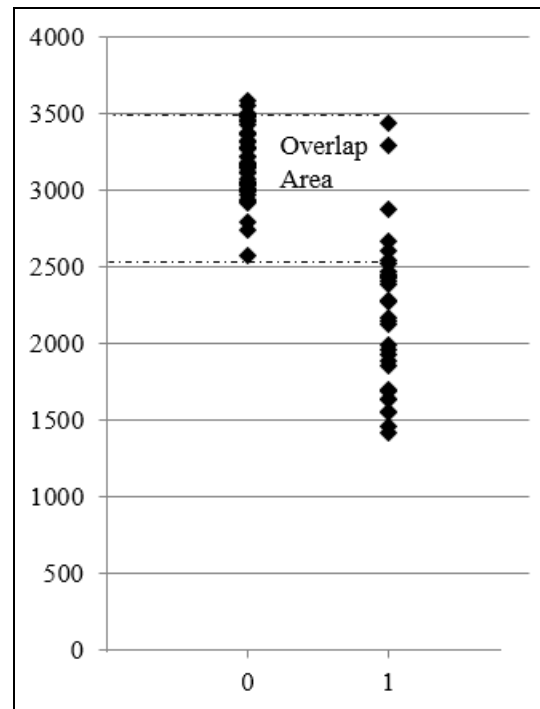
(e)



(f)



(g)



(h)

Figure 4.9: Wavelet feature vector element values corresponding to unfavorable (“0” binary code) or favorable (“1” binary code) chip forms for the following selected wavelet feature vectors: (a) $\sigma^2[\text{DAA}]F_x$, (b) $\sigma_3[\text{DAD}, F_x]$, (c) $\sigma_2[\text{DDD}, F_x]$, (d) $\sigma_4[\text{DADD}, F_x]$, (e) $E[\text{AAD}, F_y]$, (f) $E[\text{AAD}, F_y]$, (g) $E[\text{AADA}, F_y]$, and (h) $E[\text{AADD}, F_y]$.

4.1.5 Decision making and results

The wavelet feature vectors can be used as inputs in a NN based pattern recognition procedure for chip form classification [142]. However, not all the available wavelet feature vectors are suitable for this purpose. In many instances, they can introduce excessive noise into the pattern recognition system, particularly in the case of lower ranked wavelet feature vectors characterized by a high number of elements with overlapping values for favorable or unfavorable chip forms.

To markedly reduce this source of noise, only the 8 higher ranked wavelet feature vectors, displaying a maximum of 7 cutting tests with overlapping element values, were selected and used to set up the training set for NN learning. These 8 wavelet feature vectors are: $\sigma^2[\text{DAA}]F_x$, $\sigma^3[\text{DAD}]F_x$, $\sigma^2[\text{DDD}]F_x$, $\sigma^4[\text{DADD}]F_x$, $E[\text{AAD}]F_y$, $E[\text{AAAA}]F_y$, $E[\text{AADA}]F_y$, $E[\text{AADD}]F_y$.

Thus, the NN input matrix is a 77×8 matrix composed of the above 8 high ranked 77-elements wavelet feature vectors. The NN output matrix is a 77×1 matrix composed of the binary values that identify the chip form generated by each of the 77 cutting tests (0 = unfavorable and 1 = favorable chip form). Therefore, the NN architecture has the following structure: input layer with 8 nodes, output layer with 1 node, and hidden layer with either 32 or 64 nodes, heuristically set.

The NN results consist of a set of success rates (SR): the training SR, the validation SR, the testing SR, and the overall SR. Table 4.6 reports all the obtained SR for the two NN configurations used for favorable/ unfavorable chip form classification: 8-32-1 and 8-64-1.

Table 4.6: NN chip form identification success rate.

Success Rate	NN Configuration	
	8-32-1	8-64-1
Training SR	96.2 %	79.2 %
Validation SR	83.3 %	100.0 %
Testing SR	83.3 %	75.0 %
Overall SR	92.2 %	81.8 %

All obtained NN SR values are higher than 75%. By considering the overall SR, given by the ratio of correctly classified cases over the total number of cases, as the most significant to assess the NN results, the 8-32-1 NN configuration is seen to provide a performance in chip form classification as high as 92.2%. To further reduce the already limited number of misclassification cases, a data refinement approach was implemented [73][151][152]. Examining the cutting tests causing uncertainty due to overlapping element values in the wavelet feature vectors used for NN pattern recognition (Table 4.7), it can be noted that these tests are the same for several of the selected wavelet feature vectors. Data refinement was carried out by eliminating, from the total 77 valid cutting tests, the 6 cutting tests responsible

for uncertainty that are present in five or more wavelet feature vectors (grey shadowed cutting tests in Table 4.7).

The 71 remaining cutting tests were used to re-construct the 8 selected feature vectors now composed of 71 elements (“refined wavelet feature vectors”).

Figure 4.10 shows the element values of the refined wavelet feature vector made of the variance of decomposition packet DAA for cutting force component F_x . Comparing Figures 4.9 (a) and 4.10, it can be seen that the number of overlapping element values is greatly reduced in the case of the refined wavelet feature vector (2 vs. 7). This decrease overlapping element values is expected to improve the NN SR for chip form classification.

Table 4.7: Cutting tests responsible for uncertainty in the 8 selected wavelet feature vectors reported under the corresponding wavelet vector: the grey shadowed cutting tests are eliminated from the training set for data refinement.

σ^2 [DAA, F_x]	σ^3 [DAD, F_x]	σ^2 [DDD, F_x]	σ^4 [DADD, F_x]
T0001301	T0001301	T0001356	T0001301
T0001356	T0001356	T0001357	T0001356
T0001357	T0001357	T0001358	T0001357
T0001358	T0001358	T0001372	T0001358
T0001373	T0001373	T0001373	T0001373
T0001386	T0001377	T0001386	T0001376
T0001388	T0001386	T0001387	T0001387

E [AAD, F_y]	E [AAAA, F_y]	E [AADA, F_y]	E [AADD, F_y]
T0001301	T0001324	T0001301	T0001301
T0001324	T0001361	T0001324	T0001324
T0001357	T0001373	T0001358	T0001373
T0001373	T0001387	T0001373	T0001387
T0001377	T0001388	T0001379	T0001388
T0001387		T0001387	
T0001388		T0001388	

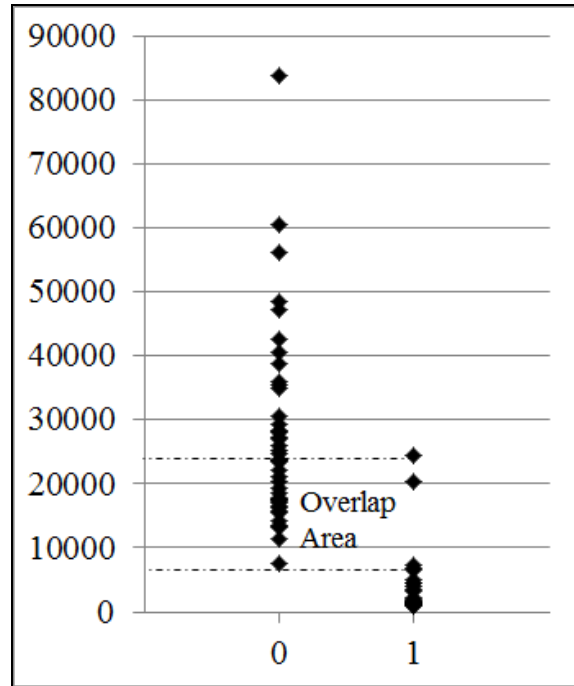


Figure 4.10: Refined wavelet feature vector element values given by the variance of decomposition packet DAA of cutting force component F_x for unfavorable (“0” binary code) and favorable (“1” binary code) chip forms.

After data refinement, the previously built 8-32-1 NN and 8-64-1 NN were trained and tested with the refined wavelet feature vectors and the NN SR for two configurations are summarized in Table 4.5.

Table 4.8: NN success rates after data refinement.

Success Rate	NN Configuration	
	8-32-1	8-64-1
Training SR	98.0 %	95.9 %
Validation SR	100.0 %	90.9 %
Testing SR	90.9 %	100.0 %
Overall SR	97.2 %	95.8 %

By comparing Tables 4.5 and 4.8, in the case of the refined training set all obtained NN SR values are higher than 90%, i.e. much higher than the 75% lower limit verified before data refinement. By considering the overall SR as the most significant to assess the NN results, the 8-32-1 NN configuration provides a performance equal to 97.2%, significantly improved in comparison with the already high 92.2% overall SR achieved before data refinement.

4.2. Residual stress assessment

Industries aim to machine parts that satisfy both functional and quality requirements. There are several factors to take into consideration that may affect the functionality and quality of the machined part. These factors are directly related to the surface integrity (including topological factors parameters such as surface roughness), mechanical properties (residual stress, hardness, etc.), and metallurgical states of the work material during processing (phase transformation, microstructure, and related property variations) [153].

Residual stress is induced in the work material by the cutting process and is classified as unacceptable or acceptable based on a critical value defined by the work material characteristics and the service requirements. Creating an on-line residual stress assessment system is highly desirable due to the fact that unacceptable levels affect the fatigue life of the machined part [154].

For the purpose of investigating into residual stress level assessment, experimental turning tests were performed on Inconel 718 cylindrical shafts by varying the cutting conditions and using a multiple sensor monitoring system for the acquisition of sensor signals:

- 3 components of cutting force: F_x, F_y, F_z
- acoustic emission RMS: AE_{RMS}
- 3 components of vibration acceleration: A_x, A_y, A_z

The detected signals were processed using the wavelet packet transform (WPT) to extract characteristic features obtained from the WPT coefficients [52] [144]. The extracted wavelet packet features were used, within a sensor fusion approach, as input to diverse neural network architectures for decision making on machined surface integrity in terms of residual stress level [52].

4.2.1 Generalities: residual stress in machining

It is probably true to say that all engineering components contain stresses (of variable magnitude and direction) even before being subjected to service loading conditions. This is due to the history of the material prior to putting it in service. These stresses, produced as a result of mechanical working and machining of the material, heat treatment, chemical treatment, joining procedure, etc., are called residual stresses and they can have a very significant effect on the fatigue life of the final components. These residual stresses are “locked into” the component also in the absence of external loading and represent a datum stress over which the service load stresses are subsequently superimposed.

If the resulting residual stresses are of opposite direction to the service stresses, then part of the service load goes to reduce the residual stress to zero before the combined stress can once again rise towards any likely failure value. Thus, such residual stresses are extremely beneficial to the strength of the component and significantly higher fatigue strengths can result. If, however, the residual stresses are of the same direction as the applied stress. Taking

an example where applied stress and residual stress are both tensile, a smaller service load is required to produce failure than would have been the case for a component with a zero stress level initially. The strength and fatigue life in this case is hence reduced. Thus, both the magnitude and direction of the residual stresses are important for fatigue life considerations, and methods for determining these quantities are introduced below [155].

4.2.2 X-ray diffraction technique

[PAUL S. PREVÉY, LAMBDA RESEARCH, INC]

In x-ray diffraction residual stress measurement, the strain in the crystal lattice is measured, and the residual stress producing the strain is calculated, assuming a linear elastic distortion of the crystal lattice. Although the term stress measurement is commonly used, stress is an extrinsic property that is not directly measurable. All methods of stress determination require measurement of some intrinsic property, such as strain or force and area, and then, the calculation of the related stress. Mechanical methods, better known as dissection techniques, and nonlinear elastic method, usually ultrasonic and magnetic techniques, are limited techniques in their applicability to residual stress determination. Mechanical methods are limited by assumptions concerning the nature of the residual stress field and sample geometry. Mechanical methods, which are basically destructive, cannot be directly checked by repeated measurement. Spatial and depth resolution and all nonlinear elastic methods are subject to major error from preferred orientation, cold work, temperature, and grain size. All require stress-free reference samples, which are otherwise identical to the sample under investigation. Generally, near elastic methods are not suitable for routine residual stress determination at their current state of development. In addition, their spatial and depth resolutions are orders of magnitude less than those of x-ray diffraction.

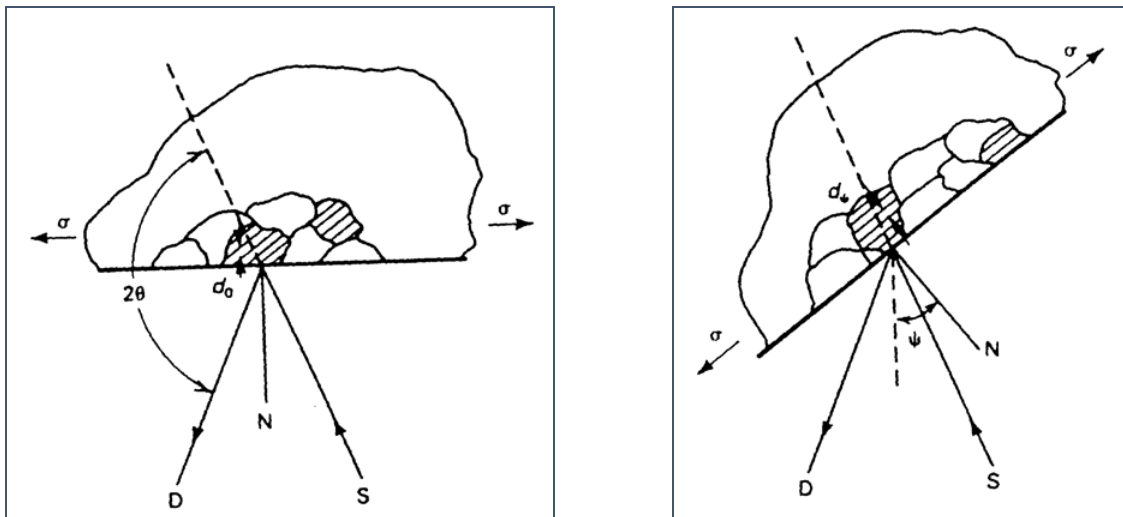
To determine the stress, the strain in the crystal lattice must be measured in at least two precisely known orientations relative to the sample surface. Therefore, x-ray diffraction residual stress measurement is applicable to materials that are crystalline, relatively fine grained, and produce diffraction for any orientation of the sample surface. Samples may be metallic or ceramic, provided a diffraction peak of suitable intensity and free of interference from neighboring peaks can be produced in the high back-reflection region with the radiations available. X-ray diffraction residual stress measurement is unique in that macroscopic and microscopic residual stresses can be determined nondestructively 0

Macroscopic stresses, or macrostresses, which extend over distances that are large relative to the grain size of the material, are of general interest in design and failure analysis. Macrostresses are tensor quantities, with magnitudes varying with direction at a single point in a body. The macrostress for a given location and direction is determined by measuring the strain in that direction at a single point. When macrostresses are determined in at least three known directions, and a condition of plane stress is assumed, the three stresses can be combined using Mohr's circle for stress to determine the maximum and minimum residual stresses, the maximum shear stress, and their orientation relative to a reference direction.

Macro stresses strain many crystals uniformly in the surface. This uniform distortion of the crystal lattice shifts the angular position of the diffraction peak selected for residual stress measurement.

Microscopic stresses, or micro stresses, are scalar properties of the sample, such as percent of cold work or hardness, that are without direction and result from imperfections in the crystal lattice. Micro stresses are associated with strains within the crystal lattice that traverse distances on the order of or less than the dimensions of the crystals. Micro stresses vary from point to point within the crystal lattice, altering the lattice spacing and broadening the diffraction peak. Macro stresses and micro stresses can be determined separately from the diffraction peak position and breadth.

Figure 4.11 shows the diffraction of a monochromatic beam of x-rays at a high diffraction angle (2θ) from the surface of a stressed sample for two orientations of the sample relative to the x-ray beam. The angle ψ , defining the orientation of the sample surface, is the angle between the normal of the surface and the incident and diffracted beam bisector, which is also the angle between the normal to the diffracting lattice planes and the normal to sample surface [156].



(a)

(b)

**Figure 4.12: (a) $\psi = 0$. (b) $\psi = \psi$ (sample rotated through some known angle ψ).
D, x-ray detector; S, x-ray source; N, normal to the surface.**

Diffraction occurs at an angle 2θ , defined by Bragg's Law:

$$n\lambda = 2d \sin \theta$$

where:

n: integer denoting the order of diffraction

λ : x-ray wavelength

d: lattice spacing of crystal planes

θ : diffraction angle.

For the monochromatic x-rays produced by the metallic target of an x-ray tube, the wavelength is known to 1 part in 10⁵. Any change in the lattice spacing, d, results in a corresponding shift in the diffraction angle 2θ .

Figure 4.12 (a) shows the sample in the $\psi = 0$ orientation. The presence of a tensile stress in the sample results in a Poisson's ratio contraction, reducing the lattice spacing and slightly increasing the diffraction angle, 2θ . If the sample is then rotated with a known angle ψ (Figure 4.12(b)), the tensile stress present in the surface increases the lattice spacing over the stress-free state and decreases 2θ . Measuring the change in the angular position of the diffraction peak for at least two orientations of the sample defined by the angle ψ enables the calculation of the stress present in the sample surface lying in the plane of diffraction. This plane which contains the incident and diffracted x-ray beams. To measure the stress at the same point but in different directions, the sample is rotated about its normal surface to coincide the direction of interest with the diffraction plane.

Because only elastic strain alters the mean lattice spacing, only elastic strains are measured using x-ray diffraction for the determination of macrostresses. When the elastic limit is exceeded, further strain results in dislocation motion, disruption of the crystal lattice, and the formation of microstresses, but no additional increase in macroscopic stress. Although residual stresses result from non-uniform plastic deformation, all residual macrostresses remaining after deformation are necessarily elastic.

The residual stress determined using x-ray diffraction is the arithmetic average stress in a volume of material defined by the irradiated area, which may vary from square centimeters to square millimeters, and the depth of penetration of the x-ray beam. The linear absorption coefficient of the material for the radiation used governs the depth of penetration, which can vary considerably.

However, in iron, nickel, and aluminum-base alloys, 50% of the radiation is diffracted from a layer approximately 0.005 mm (0.0002 in.) deep for the radiations generally used for stress measurement. This shallow depth of penetration allows the determination of macro and microscopic residual stresses as function of depth, with a depth resolution approximately 10 to 100 times the resolution possible using other methods. Although, in general, virtually any interplanar spacing may be used to measure strain in the crystal lattice, availability of the wavelengths produced by commercial x-ray tubes limits the choice to a few possible planes.

The choice of a diffraction peak selected for residual stress measurement impacts significantly on the precision of the method. The higher the diffraction angle, the greater the precision. Practical techniques generally require diffraction angles, 2θ , greater than 120° .

Table 4.9 lists recommended diffraction techniques for Nickel base alloys. The relative sensitivity is shown by the value of K_{45} , the magnitude of the stress necessary to cause an apparent shift in diffraction-peak position of 1° for a $45^\circ\psi$ tilt. As K_{45} increases, sensitivity decreases.

Table 4.9: Inconel 718 Diffraction technique.

Alloy	Radiation	Lattice Plane (hkl)	Angle (2θ), degrees	Elastic constants(a) (E/I= ν) GPa (10^6 psi)		Bulk Error (%)	K_{45} (b)		Linear Absorption Coeff. (μ)
				(hkl)	Bulk		MPa	ksi	cm^{-1}
Nickel-base alloys									
Inconel 718	Cu $K\alpha$	(420)	145.0	140.0\pm2.1	156.5	-8.9	772	112.0	1232
(a) Constants determined from four-point bending tests. (b) K_{45} is the magnitude of the stress necessary to cause an apparent shift in diffraction-peak position of 1° for 45° angle tilt									

Plane-Stress Elastic Model

X-ray diffraction stress measurement is confined to the surface of the sample. Electro polishing is used to expose new surfaces for subsurface measurement. In the exposed surface layer, a condition of plane stress is assumed to exist. That is, a stress distribution described by principal stresses σ_1 and σ_2 exists in the plane of the surface, and no stress is assumed perpendicular to the surface, $\sigma_3 = 0$. However, a strain component perpendicular to the surface ϵ_3 exists as a result of the Poisson's ratio contractions caused by the two principal stresses (Figure 4.13).

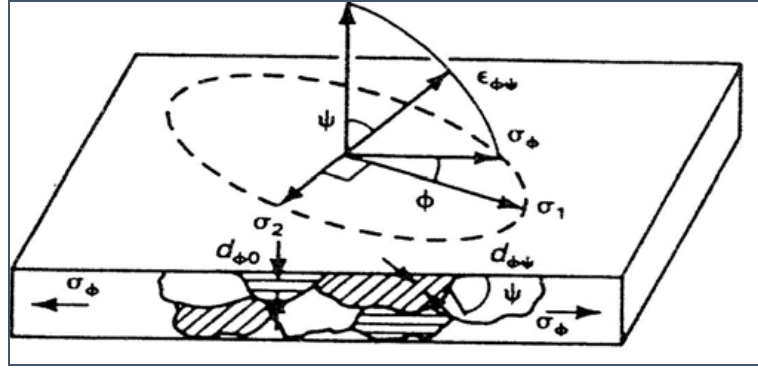


Figure 4.13: Plane stress elastic model.

The strain, $\epsilon_{\phi\psi}$ in the direction defined by the angles ϕ and ψ is:

$$\epsilon_{\phi\psi} = \left[\frac{1+\nu}{E} (\sigma_1 \sigma_1^2 + \sigma_2 \sigma_2^2) \right] - \left[\frac{\nu}{E} (\sigma_1 + \sigma_2) \right]$$

where E is the modulus of elasticity, ν is the Poisson's ratio, and α_1 and α_2 are the angle cosines of the strain vector:

$$\alpha_1 = \cos \phi \sin \psi$$

$$\alpha_2 = \sin \phi \sin \psi$$

Substituting for the angle cosines and simplifying enables expressing the strain in terms of the orientation angles:

$$\epsilon_{\phi\psi} = \left[\frac{1+\nu}{E} (\sigma_1 \cos^2 \phi + \sigma_2 \sin^2 \phi) \sin^2 \psi \right] - \left[\frac{\nu}{E} (\sigma_1 + \sigma_2) \right]$$

If the angle ψ is taken to be 90° , the strain vector lies in the plane of the surface, and the surface stress component, σ_ϕ is:

$$\sigma_\phi = (\sigma_1 \cos^2 \phi) + (\sigma_2 \sin^2 \phi)$$

Substituting the equation of the surface stress into the strain equation yields the strain in the sample surface at an angle ϕ from the principal stress σ_1 :

$$\varepsilon_{\phi\psi} = \left[\frac{1+\nu}{E} (\sigma_{\phi}) \sin^2 \psi \right] - \left[\frac{\nu}{E} (\sigma_1 + \sigma_2) \right]$$

The above equation relates the surface stress σ_{ϕ} , in any direction defined by the angle ψ , to the strain, ε , in the direction (ϕ, ψ) and the principal stresses in the surface.

If $d_{\phi\psi}$ is the spacing between the lattice planes measured in the direction defined by ϕ and ψ , the strain can be expressed in terms of changes in the linear dimensions of the crystal lattice:

$$\varepsilon_{\phi\psi} = \frac{\Delta d}{d_0} = \frac{d_{\phi\psi} - d_0}{d_0}$$

where d_0 is the stress-free lattice spacing. Substitution into the strain equation yields:

$$\frac{d_{\phi\psi} - d_0}{d_0} = \left[\left(\frac{1+\nu}{E} \right)_{(hkl)} \sigma_{\phi} \sin^2 \psi \right] - \left[\left(\frac{\nu}{E} \right)_{(hkl)} (\sigma_1 + \sigma_2) \right]$$

where the elastic constants $\left(\frac{1+\nu}{E} \right)_{(hkl)}$ and $\left(\frac{\nu}{E} \right)_{(hkl)}$ are not the bulk values but the values for the crystallographic direction normal to the lattice planes in which the strain is measured as specified by the Miller indices (hkl) . Because of elastic anisotropy, the elastic constants in the (hkl) direction commonly vary significantly from the bulk mechanical values, which are an average over all possible directions in the crystal lattice.

The lattice spacing for any orientation, then, is:

$$d_{\phi\psi} = \left[\left(\frac{1+\nu}{E} \right)_{(hkl)} \sigma_{\phi} d_0 \sin^2 \psi \right] - \left[\left(\frac{\nu}{E} \right)_{(hkl)} d_0 (\sigma_1 + \sigma_2) \right] + d_0$$

The above equation describes the fundamental relationship between lattice spacing and the biaxial stresses in the surface of the sample. The lattice spacing $d_{\phi\psi}$, is a linear function of $\sin^2 \psi$.

Figure 4.14 shows the actual dependence of $d(311)$ on ψ , ranging from 0 to 45° for shot peened 5056-O aluminum having a surface stress of -148 MPa (-21.5 ksi), to which a straight line has been fitted by least squares regression.

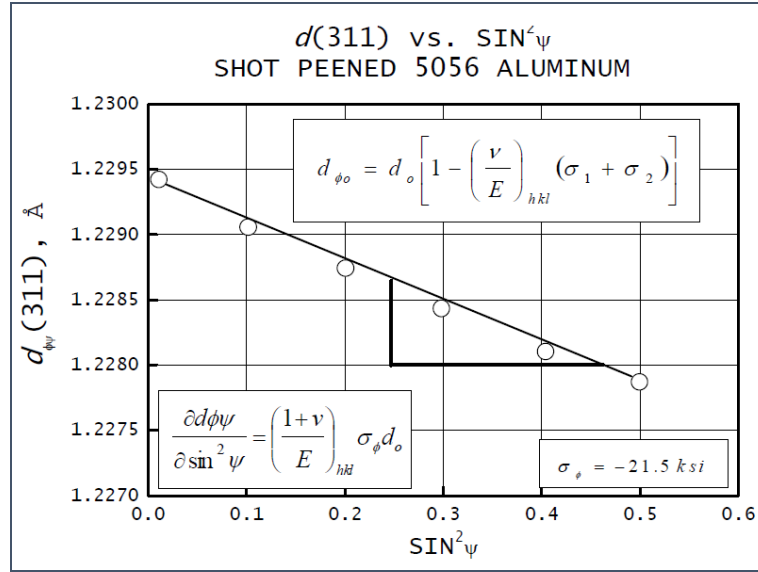


Figure 4.14: A $d(311)$ versus $\sin^2\psi$ plot for a shot peened 5056-O aluminum alloy having a surface stress of -148 MPa.

The intercept of the plot at $\sin^2\psi = 0$ is:

$$d_{\phi\psi} = d_0 - \left(\frac{\nu}{E}\right)_{(hkl)} d_0 (\sigma_1 + \sigma_2) = d_0 \left[1 - \left(\frac{\nu}{E}\right)_{(hkl)} (\sigma_1 + \sigma_2) \right]$$

which equals the unstressed lattice spacing, d_0 , minus the Poisson's ratio contraction caused by the sum of the principal stresses.

The slope of the plot is:

$$\frac{\partial d_{\phi\psi}}{\partial \sin^2\psi} = \left(\frac{1+\nu}{E}\right)_{(hkl)} \sigma_{\phi} d_0$$

which can be solved for the stress σ_{ϕ} :

$$\sigma_{\phi} = \left(\frac{E}{1+\nu}\right)_{(hkl)} \frac{1}{d_0} \left(\frac{\partial d_{\phi\psi}}{\partial \sin^2\psi}\right)$$

The x-ray elastic constants can be determined empirically, but the unstressed lattice spacing, d_0 , is generally unknown. However, because $E \gg (\sigma_1 + \sigma_2)$, the value of $d_{\phi 0}$ differs from d_0 by not more than $\pm 1\%$, and σ_{ϕ} may be approximated to this accuracy using:

$$\sigma_{\phi} = \left(\frac{E}{1+\nu} \right)_{(hkl)} \frac{1}{d_{\phi 0}} \left(\frac{\partial d_{\phi\psi}}{\partial \sin^2 \psi} \right)$$

The method then becomes a differential technique, and no stress-free reference standards are required to determine d_0 for the biaxial stress case. The three most common methods of x-ray diffraction residual stress measurement, the single-angle, two-angle, and $\sin^2\psi$ techniques, assume plane stress at the sample surface and are based on the fundamental relationship between lattice spacing and stress.

The $\sin^2\psi$ technique

The $\sin^2\psi$ technique [157] is identical to the two-angle technique, except lattice spacing is determined for multiple ψ tilts, a straight line is fitted using the least square method, and the stress is calculated from the slope of the best fit line. The method, a standard procedure in Japan and Germany, provides no significant improvement in precision over the two-angle technique if the two data points are selected at the extreme ends of the $\sin^2\psi$ range.

The primary advantage of the $\sin^2\psi$ technique, considering the additional time required for data collection, is in establishing the linearity of d as a function of $\sin^2\psi$ to demonstrate that x-ray diffraction residual stress measurement is possible on the sample of interest.

4.2.3 Basic procedure

Sample preparation

If the geometry of the sample does not interfere with the incident or diffracted x-ray beams, is generally minimal. Preparation of the sample surface depends on the nature of the residual stresses to be determined. If the stresses of interest are produced by such surface treatments as machining, grinding, or shot peening, then the residual stress distribution is usually limited to less than 500 μm of the sample surface. Therefore, the sample surface must be carefully protected from secondary abrasion, corrosion, or etching. Samples should be oiled to prevent corrosion and packed to protect the surface during handling. Secondary abrasive treatment, such as wire brushing or sand blasting, radically alters the surface residual stresses, generally producing a shallow, highly compressive layer over the original residual stress distribution.

If the stresses of interest are those produced by carburizing or heat treatment, it may be advisable to electropolish the surface of the sample, which may have undergone finish grinding or sand blasting after heat treatment. Electropolishing eliminates the shallow, highly stressed surface layer, exposing the subsurface stresses before measurement.

To measure the inside surface of tubing, in bolt holes, between gear teeth, and other restrictive geometries, the sample must be sectioned to provide clearance for the incident and diffracted x-ray beams. Unless prior experience with the sample under investigation indicates that no significant stress relaxation occurs upon sectioning, electrical resistance strain-gage rosettes

should be applied to the measurement area to record the strain relaxation that occurs during sectioning. Unless the geometry of the sample clearly defines the minimum and maximum directions of stress relaxation, a full rectangular strain-gage rosette should be used to calculate the true stress relaxation in the direction of interest from the measured strain relaxation.

Following x-ray diffraction residual stress measurements, the total stress before sectioning can be calculated by subtracting algebraically the sectioning stress relaxation from the x-ray diffraction results. If only near-surface layers are examined on a massive sample, a constant relaxation correction can be applied to all depths examined. If a significant volume of material is removed, as in determination of the stress distribution through the carburized case of a thin bearing race, a more accurate representation of sectioning relaxation can be achieved by applying strain-gage rosettes to the inner and outer surfaces and by assuming a linear relaxation of stress through the sample.

Sample Positioning

Because the diffraction angles must be determined with an accuracy of approximately $\pm 0.01^\circ$, the sample must be positioned under the x-ray beam at the true center of rotation of both angles ψ and 2θ axes. In addition, the angle ψ must be constant throughout the irradiated area.

Therefore, extremely precise positioning of the sample with accuracies of approximately 0.025 mm (0.001 in.) is critical. Further, the size of the irradiated area must be limited to an essentially flat region on the sample surface. Samples with small diameters or complex sample geometries such as small-radius fillets, the roots of threads, and fine-pitched gears may contribute to major sources of error if the x-ray beam is not confined to an essentially flat region at a known ψ tilt on the curved surface. If the irradiated area is allowed to span a curved surface, ψ will not be constant during determination of lattice spacing. These restrictions imposed by the sample geometry may prohibit x-ray diffraction residual stress measurement in many areas of primary concern, such as the roots of notches.

Irradiated Area and Measurement Time

The residual stress determined by x-ray diffraction is the arithmetic average stress in the area defined by the dimensions of the x-ray beam. Considerations must be given to choose an appropriate beam size depending on the nature of the stress to be investigated. If average stresses over significant areas are of interest, the maximum beam size allowed by the geometry of the sample would be an appropriate choice. If local variations in residual stress, such as those produced by individual passes of a grinding wheel, are of interest, a smaller irradiated area with a geometry appropriate for the investigation should be selected. Practical dimensions of the irradiated area may range from circular zones 1.25 mm in diameter to a range of rectangular geometries from approximately 0.5 to 13 mm. The maximum irradiated area generally feasible is approximately 13×8 mm.

As the irradiated area is increased, the data collection time necessary to achieve adequate precision for residual stress measurement diminishes. The precision with which the diffracted

intensity can be determined varies as the inverse of the square root of the number of x-rays collected. To determine the intensity to an accuracy of 1% at a single point on the diffraction peak, 104 x-rays must be counted, regardless of the time required. With diffracted intensities typically available on a fixed slit diffractometer system, this may require collection time of approximately 30 seconds for each point on the diffraction peak. If seven data points are collected on each diffraction peak for a two-angle technique, total measurement time may be 10 to 15 min. Reducing the irradiated area sufficiently to decrease the diffracted intensity by an order of magnitude increases the data collection time proportionally for the same precision in measurement. If fluorescence is not a problem, position-sensitive detectors can be used to collect data simultaneously at numerous points across the diffraction peak, with some sacrifice in angular precision, reducing data collection time by an order of magnitude [156].

Diffraction-Peak Location

The transition metal target x-ray tubes used for stress measurement produce a continuous spectrum of white radiation and three monochromatic high-intensity lines. The three lines are the $K_{\alpha 1}$, $K_{\alpha 2}$, and K_{β} characteristic radiations with wavelengths known to high precision. The $K_{\alpha 1}$ and $K_{\alpha 2}$ lines differ too little in wavelength to allow separation of the diffraction peaks produced. The $K_{\alpha 1}$ line, the highest intensity, is nominally twice that of the $K_{\alpha 2}$ line. The K_{β} line is produced at a substantially shorter wavelength and can generally be separated from the K_{α} lines by filtration, the use of high-energy resolution detectors, or crystal monochromators. The K_{β} line is typically one-fifth the intensity of the $K_{\alpha 1}$ line and is generally too weak for practical x-ray diffraction residual stress measurement on plastically deformed surfaces.

Because the K_{α} doublet is generally used for residual stress measurement, the diffraction peaks produced consist of a superimposed pair of peaks, as shown in Figure 4.15 for four cases, indicating the various degrees of broadening that may be encountered. The variable blending of the K_{α} doublet typical of an annealed sample is indicated by curve A; a fully hardened or cold-worked sample, curve D. Because the accuracy of x-ray diffraction residual stress measurement depends on the precision with which the diffraction peak can be located, the method used to locate broadened doublet peaks is of primary importance.

Precise determination of the position of the diffraction peak at each ψ tilt begins with collection of raw intensity data at several points on the peak. The diffracted intensity (x-rays counted per unit time) or inverse intensity (time for a fixed number of x-rays to be counted) is determined to a precision exceeding 1% at several fixed diffraction angles, 2θ , spanning the diffraction peak. Depending on the method to be used for peak location, 3 to 15 individual data points and 2 background points are measured using standard diffractometer techniques. If data are collected using a position-sensitive detector, the diffracted intensity can be determined at dozens of data points spanning the diffraction peak. Sharp diffraction peaks, such as those shown in curve A in Figure 4.15, may be located using intensity data of lower precision than that required for broad peaks, as shown in curve D. The number of x-rays to be collected, and therefore the time required for stress measurement to a fixed precision, increases as the diffraction peaks broaden.

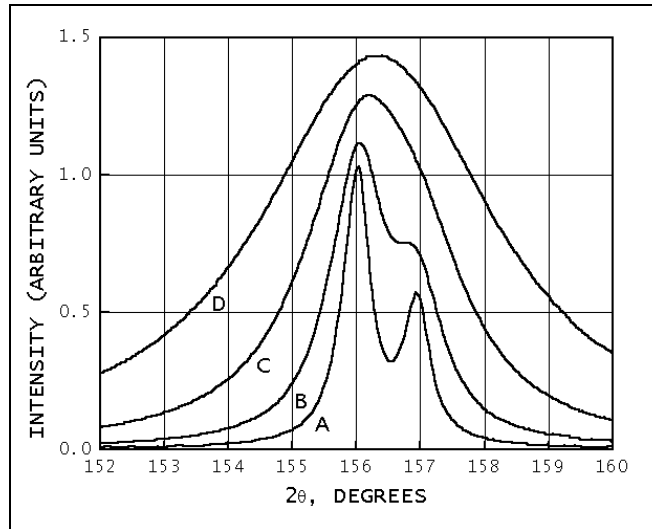


Figure 4.15: Range of $K\alpha$ doublet blending for a simulated steel (211) Cr $K\alpha$ peak at 156.0° . A, fully annealed, B and C, intermediate hardness; D, fully hardened.

Before determining a diffraction-peak position, the raw measured intensities must be corrected for Lorentz polarization and absorption. A sloping background intensity is then corrected by subtracting the background, assuming a linear variation beneath the diffraction peak. Various numerical methods are available to calculate the position of the diffraction peak. The simplest method, incorporated in early automated diffraction equipment, is to locate 2θ positions on either side of the peak at which the intensity is equal and assume the peak position to be at the midpoint. A straight line can be fitted to the opposing sides of the diffraction peak and the point of intersection of the two lines taken as a peak position [158]. Early SAE literature recommends calculating the vertex of the parabola defined by three points confined to the top 15% of the peak [159]. A significant improvement in precision can be achieved, approaching the 0.01° resolution of most diffractometers, by collecting 5 to 15 data points in the top 15% and fitting a parabola by least squares regression before calculation of the peak vertex.

If the intensity is measured at many points ranging across the entire $K\alpha$ doublet, the peak position can be calculated as the centroid of the area above the background or by autocorrelation. Both of these area-integration methods are independent of the peak shape, but are extremely sensitive to the precision with which the tails of the diffraction peak can be determined.

All the above methods are effective, regression fit parabola being superior, if applied to a single symmetrical diffraction peak profile, such as the simple $K\alpha_1$ peak shown in curve A in Figure 4.10 or the fully combined doublet shown in curve D. All can lead to significant error in the event of partial separation of the doublet, as shown in curve B (Figure 4.10). Partial separation commonly results from defocusing as the sample is tilted through a range of ψ angles. If residual stresses are measured as a function of depth, diffraction peaks can vary from breadths similar to curve D (Figure 4.10) at the cold-worked surface through a

continuous range of blending to complete separation beneath the cold-work layer, as shown in curve A. All the techniques of peak location discussed can lead to significant error in stress measurement as the degree of doublet separation varies. The Rachinger correction [160] can be applied to separate the K_{α} doublet before fitting parabolas, but the precision of the correction diminishes on the $K_{\alpha 2}$ side of the combined profile and is generally inadequate for precise residual stress measurement. Fitting Pearson VII distribution functions (Cauchy to Gaussian bell-shaped, as described in [161 and [162]) separately to the $K_{\alpha 1}$ and $K_{\alpha 2}$ diffraction peaks, assuming a doublet separation based on the difference in wavelength, provides a method of peak location that overcomes most of the problems outlined above.

Figures 4.16 and 4.17 show the effect of the peak-location method on the results obtained. Figure 4.16 illustrates comparison of the same data reduced using Pearson VII distribution functions and a five-point least squares parabolic fit for ground Ti-6Al-4V using the (21.3) planes for residual stress measurement. Apparent nonlinearities in d versus $\sin^2\psi$ for the parabola fit are due to inaccurate diffraction-peak location in the presence of partial blending of the K_{α} doublet. Figure 4.17 shows the errors in stress measurement by the two methods of peak location applied to the identical data for the entire stress profile. The errors for the distribution function fit are smaller than the plotting symbols at all depths.

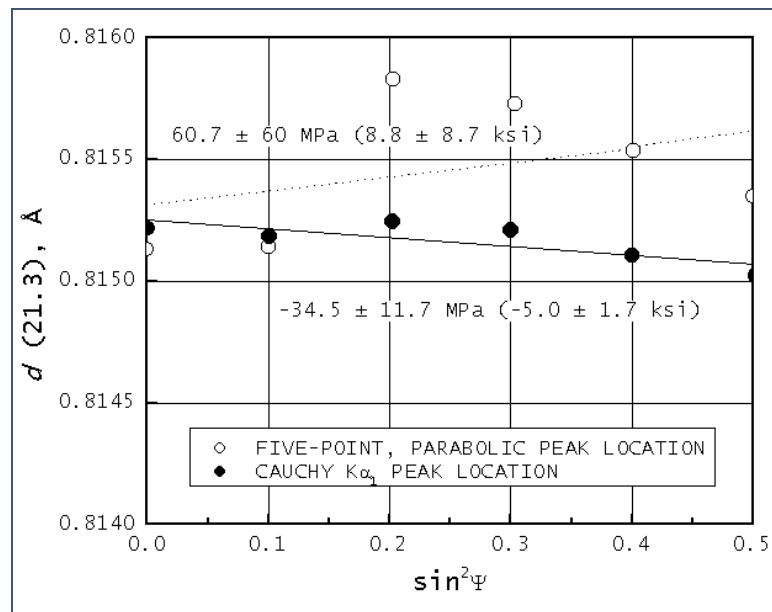


Figure 4.16: Comparison of d (21.3) versus $\sin^2\psi$ data taken 0.176 mm below the surface for a ground Ti-6Al-4V sample using two diffraction peak location methods.

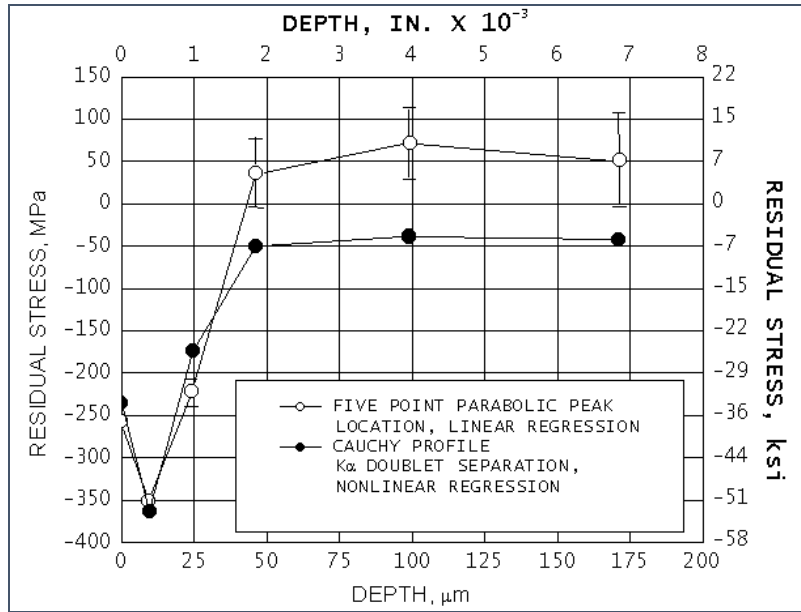


Figure 4.17: Comparison of residual stress patterns derived using Cauchy and parabolic peak location for a ground Ti-6Al-4V sample using a six-angle $\sin^2\psi$ technique. Errors in stress measurement by two methods of diffraction-peak location are shown.

Microstress Determination and line Broadening

Diffraction peak broadening caused by microstresses in the crystal lattice can be separated into components due to strain in the crystal lattice and crystallite size. Separation of the broadening, which is of instrumental origin, from that due to lattice strain and crystallite size is performed using Fourier analysis of the diffraction-peak profile and data collection sufficient to define precisely the shape of the entire diffraction peak. Analysis of the Fourier series terms allows separation of the components of the broadening attributable to lattice strain from that caused by reduction in the crystallite size. However, this method requires extensive data collection and depends on the precision with which the tails of the diffraction peak can be separated from the background intensity.

For most routine analyses of microstresses associated with cold working or heat treatment for which separation of the strain and size components is not necessary, much simpler determinations of diffraction-peak breadth are adequate. The diffraction-peak width can be quantified precisely as the integral breadth (total area under the peak divided by diffraction-peak height) or the width at half the height of the diffraction peak. The width of the diffraction peak can be measured directly from strip-chart recordings or calculated from the width of the function fitted to the diffraction-peak profile during macrostress measurement. Microstresses and macrostresses can then be determined simultaneously from the peak breadth and position.

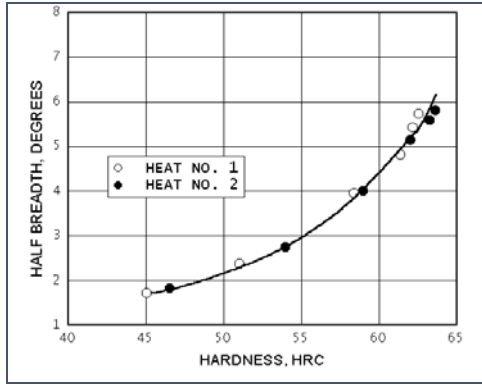


Figure 4.18: Diffraction-peak breadth at half height for the (211) peak for M50 high-speed tool steel as a function of Rockwell hardness.

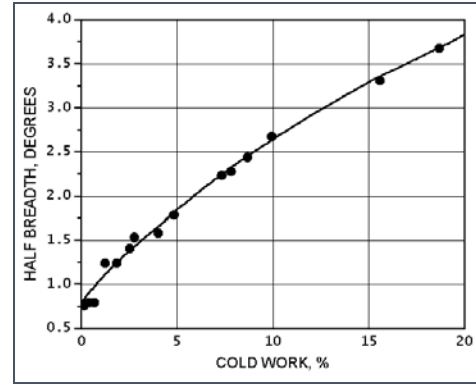


Figure 4.19: Diffraction-peak breadth at half height for the (420) peak for Rene 95 as a function of cold-working percentage.

Figures 4.18 and 4.19 show empirical relationships established between diffraction-peak breadth at half height for the (211) peak for M50 high-speed tool steel as a function of hardness and for the (420) peak breadth as a function of percent cold work for Rene 95, respectively. These empirical curves can be used to calculate the hardness or cold work in conjunction with macroscopic residual stress measurement. For the preparation of the hardness curve, a series of coupons are quenched and tempered to known hardness. The peak breadth is then measured using the same slit system and peak-location method used for macrostress measurement. For the percent cold work curve, samples are heat treated, then pulled in tension to produce a series of coupons with various known amounts of cold work. Because the initial heat treatment may alter significantly the initial peak breadth before cold work, the coupons must receive the same heat treatment as the samples to be measured before inducing known amounts of cold work [156].

Sample fluorescence

Sample fluorescence complicates the selection of radiation to be used for residual stress measurement. The radiation necessary for the highest precision techniques may cause fluorescence of the elements present in the sample under investigation. The use of Cu K_{α} radiation for residual stress measurement in alloys containing iron, chromium, or titanium can result in fluorescent background intensities many times as intense as the diffracted radiation, greatly reducing the signal-to-noise ratio. Problems with fluorescence may be overcome in some cases by use of metal foil filters, but generally require use of a crystal monochromator or high energy resolution solid-state detector. Failure to eliminate fluorescence can degrade severely the precision with which the diffraction peak can be located accurately, increasing random experimental error significantly. Diffracted beam monochromators and solid-state detectors can be used only on standard laboratory diffractometers. The position-sensitive detectors available for residual stress measurement are the gas-filled proportional counter or

fluorescence screen type and have insufficient energy resolution to overcome fluorescence [156].

4.2.4 X-ray stress analyzer

The instrument used for the residual stress measurement is an “XSTRESS 3000” X-ray stress analyzer produced by Stresstech, as shown in Figure 4.20.

The most important features are reported below [163].



Figure 4.20: Stresstech XSTRESS3000.

Technical Specifications

MAIN UNIT X3000

- High voltage power supply (generator) for X-ray tube continuously variable within 5 to 30 kV / 0 up to 10 mA.
- Ultra-compact design.
- Electrical
- 90 to 260 VAC, 48 to 62 Hz, 600 VA
- Cooling
- Self-contained recirculating water cooling with heat exchanger for X-ray tube and
- power supply. No external water supply needed.

GONIOMETER

- Xstress 3000 goniometer type G2 mounted on a tripod with magnetic anchoring as a standard.
- χ -inclination: Programmable -45° to $+45^\circ$ (standard)
- χ -oscillation: Programmable 0° to $\pm 6^\circ$.
- Distance between goniometer and the measurement point automatically adjusted to ± 0.003 mm accuracy.

DETECTORS

- Dual position sensitive MOS Linear Image Sensors in symmetrical modified χ (side inclination) geometry.
- Angular resolution: $0.029^\circ/\text{pixel}$, 512 pixels/0.5 in.
- 2θ -angle is instantly adjustable by sliding the detectors manually to the desired angular position along arc-shaped detector holder.
- 2θ -range of the detectors is continuously adjustable within $+100^\circ$ to 165°

X-RAY TUBE

- Miniature, 30 kV, 10 mA, 300 W, Cr, Cu, Co, Fe, V, Ti, Mn. Cr-tube provided as a standard. Tube can be replaced in less than 10 minutes without special tools.

CABLES

- 5 meters standard.

COLLIMATOR

- Replaceable, to provide 1, 2, 3, 4, and 5 millimeter spot sizes. Special collimators available as an option.

4.2.5 Experimental setup and procedure

Machine Tool

The machine tool employed for experimental campaign is a VDF CNC horizontal lathe as reported in Figure 4.21.



Figure 4.21: VDF CNC Horizontal Lathe machine tool.

Work material

The material used for the experimental activities is INCONEL 718.

Inconel 718 is a precipitation-hardenable nickel-chromium alloy containing significant amounts of iron, niobium, and molybdenum along with lesser amounts of aluminum and titanium. It combines corrosion resistance and high strength with outstanding weldability, including resistance to post-weld cracking. The alloy has excellent creep-rupture strength at temperatures up to 700 °C. Used in gas turbines, rocket motors, spacecraft, nuclear reactors, pumps, and tooling [163].

Table 4.10: Typical analysis in percent.

Ni(+Co):	50 - 55	Cr:	17 - 21
Fe:	bal	Co:	1
Mo:	2.3 – 3.3	Nb (+Ta)	4.75 – 5.5
Ti	0.65 – 1.15	Al:	0.2 – 0.8
C:	0.08	Mn	0.35
Si:	0.35	B:	0.006
Cu:	0.3		

Table 4.11: Inconel 718 physical properties.

Density	8.19 g/cm ³
Melting point range:	1260 – 1336 °C
Specific heat:	435 J/kg·K
Average Coefficient of Thermal Expansion:	13.0 μm/m·K
Thermal Conductivity:	11.4 W/m·K
Electrical Resistivity:	1250 n·m
Curie Temperature:	-112 °C

Table 4.12: Inconel 718 mechanical properties.

At room temperature	
Ultimate tensile strength	1240 MPa
Yield strength	1036 MPa
Elongation in 50 mm	12 %
Elastic modulus (Tension)	211 GPa
Hardness	36 HRC

Workpiece

The experimental campaign was carried out by turning an Inconel 718 cylindrical shaft, as shown in Figure 4.22.



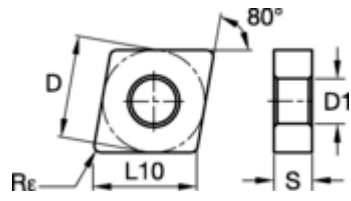
Figure 4.22: Inconel 718 Cylindrical shaft utilized as work material.

Cutting tools

The cutting tools utilized for the experimental tests are Kennametal CNMG120408-K313 rhombic uncoated carbide tools as the one shown in Figure 4.23 below.



Figure 4.23: Kennametal cutting tool.



D	L10	S	R _ε	D1
12.70	12.90	4.76	0.8	5.16

dimensions in millimeters

Figure 4.24: Cutting tool dimensions.

The tool holder is a customized compatible holder as shown in Figure 4.24.

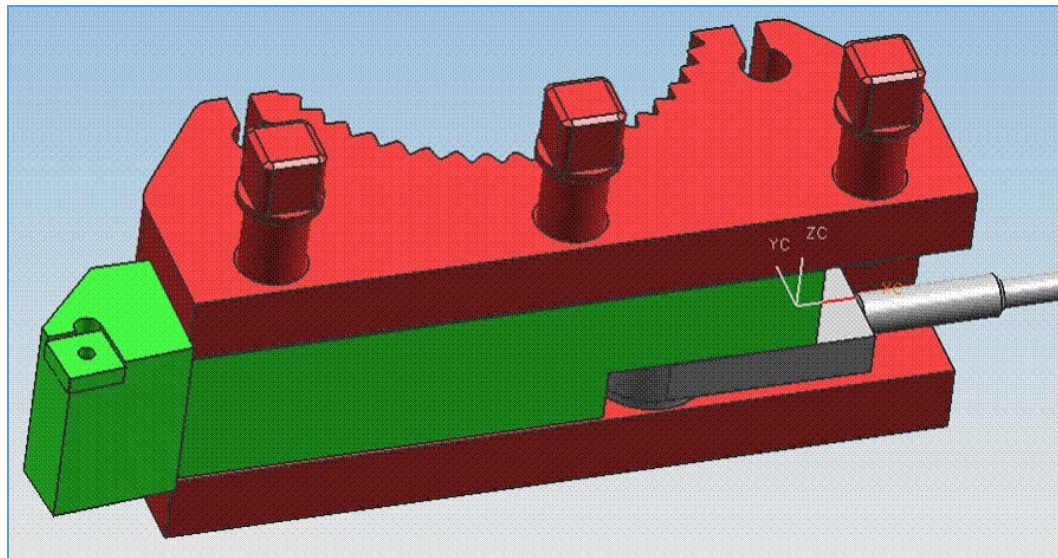


Figure 4.24: Customized tool holder.

Experimental tests program

On the basis of common cutting parameters adopted for turning of Inconel 718 workpieces, three cutting speed values were considered for the experimental program, respectively 45, 50 and 55 m/min, this last value is close to the maximum acceptable cutting speed, fixed at 56 m/min in case of cutting with carbide inserts.

Three feed rates were considered: 0.10, 0.125 and 0.15 mm/rev according to the literature and the common shop floor values.

Table 4.13: Standard Tests experimental program.

Test ID	V (m/min)	f (mm/rev)
#1	45	0.10
#2	45	0.125
#3	45	0.15
#4	50	0.10
#5	50	0.125
#6	50	0.15
#7	55	0.10
#8	55	0.125
#9	55	0.15

The depth of cut (a_p) is kept constant and is equal to 0.3 mm for every cutting test.

An additional experimental program has been carried out in order to increase the probabilities in generating surface defects.

For this purpose, severe cutting conditions were chosen, increasing both the cutting speed (up to 80 – 100 m/min) and the feed rate (up to 0.30 mm/rev). The turning tests were carried out both in cooled and in dry conditions as reported in the following table (Table 4.14).

Table 4.14: Severe cutting conditions tests experimental program.

Test ID	V (m/min)	f (mm/rev)	Cutting Fluid
#1H	80	0.15	On
#2H	80	0.30	On
#3H	100	0.15	On
#4H	100	0.30	On
#5H	80	0.15	Off
#6H	80	0.30	Off
#7H	100	0.15	Off
#8H	100	0.30	Off

Experimental tests procedure

The experimental tests began with turning the external diameter for 120 seconds setting a depth of cut equal to 0.3 mm. In this way, the external diameter was reduced by 0.6 mm at every step.

After every step, the tool wear measurement by a profile projector was carried out. If the tool wear has reached the 0.3 mm value, considered the maximum recommended acceptable value, then the test is completed otherwise there will be another 120 seconds turning step.

For the severe cutting conditions tests, the single turning step lasts 30 seconds while the tool wear threshold value is 0.5 mm. The experimental procedures can be summarized by the following flow charts reported (Figures 4.25 and 4.26).

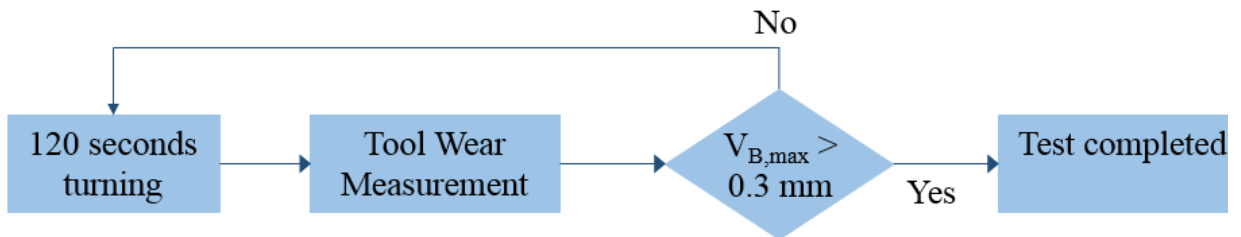


Figure 4.25: Experimental procedure flow chart for standard tests.

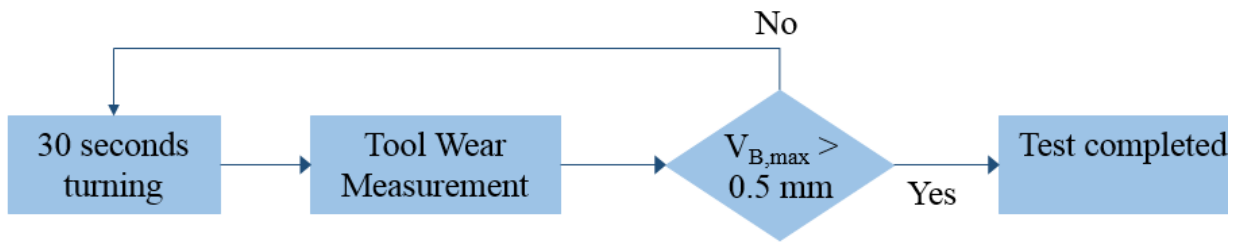


Figure 4.26: Experimental procedure flow chart for Severe Cutting Conditions tests.

In order to have 2 minutes step (or 30 seconds for Severe Cutting Conditions Tests) regardless the several cutting speeds, the cutting length Z (illustrated in Figure 4.27), was calculated as follows:

V_c	Cutting Speed	m/min
T	Cutting Time	min
D	Diameter	mm
f	Feed Rate	mm/rev
n	Number of revolutions	

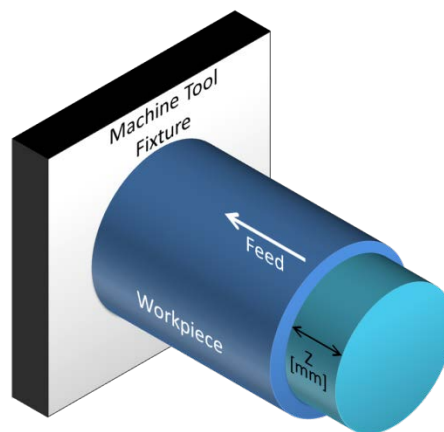


Figure 4.27: Cutting length.

$$T = \frac{Z}{n \cdot f}$$

$$Z = T \cdot n \cdot f$$

$$n = \frac{V_c \cdot 1000}{\pi \cdot D}$$

$$Z = T \cdot \frac{V_c \cdot 1000}{\pi \cdot D} \cdot f$$

At every step, the workpiece diameter decreases by 0.6 mm ($2 \cdot a_p$), consequently the cutting length increases. Hence, after calculating Z for every step, an average value was considered and used in the CNC code.

$$\tilde{Z} = \frac{\sum Z_{step}}{\text{number of steps}}$$

4.2.6 Residual stress measurement results

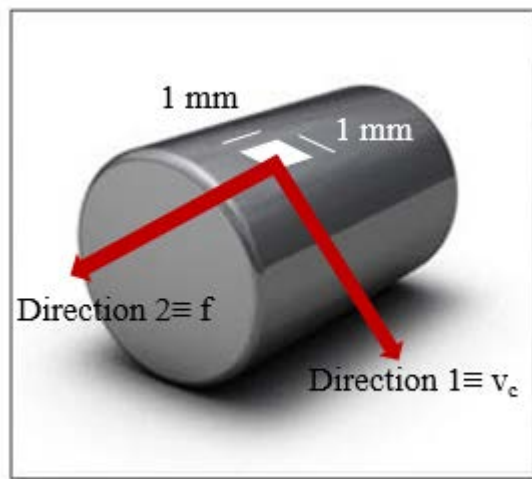


Figure 4.28: Residual stress measurement directions on a test sample.

In Figure 4.28, a residual stress measurement scheme is reported. The grey cylinder represent the test workpiece, and the white square is representative of the test surface ($1 \text{ mm} \times 1 \text{ mm}$). The two red arrows show the two measurement directions: the cutting speed direction and the feed direction respectively.

In Table 4.15, the residual stress measurements are reported, for all the tests and for both the measurement directions. In red are the values that exceed the acceptable threshold value, set at 850 MPa.

Table 4.15: Residual stress measurement results.

	Test ID	RS (MPa) direction 1	RS (MPa) direction 2	Lubrication
Standard Tests	T_1	379	-176	Cooled
	T_2	182	-287	Cooled
	T_3	455	-65	Cooled
	T_4	309	-111	Cooled
	T_5	644	35	Cooled
	T_6	767	205	Cooled
	T_7	378	-9	Cooled
	T_8	662	252	Cooled
	T_9	1009	725	Cooled
Severe Cutting Condition Tests	T_1H	1228	635	Cooled
	T_2H	1515	1206	Cooled
	T_3H	1376	882	Cooled
	T_4H	1521	1172	Cooled
	T_5H	1387	934	Dry
	T_6H	1473	965	Dry
	T_7H	1277	689	Dry
	T_8H	1412	1187	Dry

4.2.7 Sensor signal data analysis

Signal pre-processing

The sensor signals obtained during the last step of every turning test of each of the 26 test cases were subjected to sensor signal processing. For each detected sensor signal, 5 segments of 3000 samples were extracted at regular intervals so that the obtained 5 signal specimens were uniformly distributed along the original signal. Thus, a total of 130 signal specimens (9 standard cutting conditions tests \times 2 repetitions \times 5 segments + 8 severe cutting conditions tests \times 5 segments = 130 signal specimens) were obtained for each sensor signal type (F_x , F_y , F_z , AE_{RMS} , A_x , A_y , A_z).

To apply the WPT to the sensor signal specimens, a 3000×130 sensorial data table was constructed for each of the 7 sensor signal types (F_x , F_y , F_z , AE_{RMS} , A_x , A_y , A_z), where the 3000 rows represent the number of signal specimen samplings and the 130 columns contain the 130 signal specimens of the considered sensor signal type.

Wavelet Packet Transform Feature Extraction

In this sensor signal analysis process, the employed mother wavelet is a Daubechies 3 denoted by “db3” [13]. The decomposition was performed up to the 3rd level, yielding 14 packets for each of the 7 sensor signal types, for a total of 98 packets. For each packet, 5 statistical features were calculated for each of the 130 signal specimens: Standard Deviation, Skewness, Kurtosis, Root Mean Square, and Energy (Table 4.16) [145].

Table 4.16: Five statistical features for the seven sensor signal types calculated from the coefficients of each wavelet packet.

Statistical Features	Sensor Signals
Standard Deviation	$F_x, F_y, F_z, AE, A_x, A_y, A_z$
Skewness	$F_x, F_y, F_z, AE, A_x, A_y, A_z$
Kurtosis	$F_x, F_y, F_z, AE, A_x, A_y, A_z$
Root Mean Square (RMS)	$F_x, F_y, F_z, AE, A_x, A_y, A_z$
Energy	$F_x, F_y, F_z, AE, A_x, A_y, A_z$

Starting from the 3000×130 sensorial data table force cutting force component F_y (Figure 4.29, (a) table), the WPT was applied to the 130 F_y signal specimens to obtain the corresponding 130 A_1 packets, each composed of 1503 coefficients (Figure 4.29, (b) table).

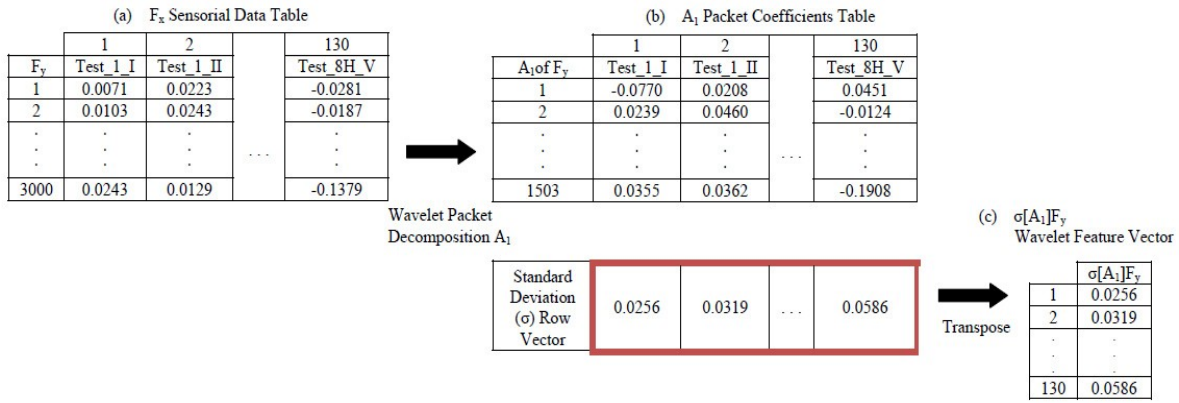


Figure 4.29: WPT feature extraction to construct the Standard Deviation (σ) feature vector for packet A_1 and cutting force component F_y : $\sigma[A_1]F_y$.

The standard deviation values of the coefficients of each A_1 packet were calculated (Figure 4.29, row vector under the (b) table). The row vector containing the 130 standard deviation values was transposed to obtain the column vector representing the Standard Deviation feature vector for packet A_1 of cutting force component F_y , denoted by $\sigma[A_1]F_y$ (Figure 4.29, (c) column vector). This type of 130-elements column vector is called shortly “wavelet feature vector”.

For each packet, the same procedure was applied to each sensor signal type, extracting a total of 5 (statistical features) \times 7 (sensor signal types) = 35 wavelet feature vectors per packet (Table 4.13).

Overall, 14 packets \times 35 wavelet feature vectors per packet = 490 total wavelet feature vectors were obtained. These wavelet feature vectors were utilized as inputs to a sensor fusion approach based on neural network data processing [96].

4.2.8 Decision making and results

The 130-elements wavelet feature vectors extracted from the sensor signal specimens through WPT were combined to implement a sensor fusion decision making approach via neural network (NN) data processing [3][99][164][165][166][167]. For each of the 14 packets, the following sensor fusion wavelet feature vectors matrices were set up to be utilized in turn as training sets for NN learning (Table 4.17):

- one 130×35 sensor fusion wavelet feature vectors matrix, where the rows refer to the 130 signal specimens and the columns are the 35 wavelet feature vectors for the concerned packet;
- five 130×7 sensor fusion wavelet feature vectors matrices, where the rows refer to the 130 signal specimens and the columns are, in turn, one of the five statistical column feature vectors (Standard Deviation, Skewness, Kurtosis, Root Mean Square, or Energy) of the 7 sensor signal types (F_x , F_y , F_z , AE , A_x , A_y , A_z) for the concerned packet.

Table 4.17: NN input wavelet feature vector matrices and NN configurations.

Statistical Feature	Wavelet Feature Vector Matrix	#Matrix Columns	NN. Configs.
All statistical features	[Stdev of $F_x, F_y, F_z, AE, A_x, A_y, A_z$; Skewness of $F_x, F_y, F_z, AE, A_x, A_y, A_z$; Kurtosis of $F_x, F_y, F_z, AE, A_x, A_y, A_z$; RMS of $F_x, F_y, F_z, AE, A_x, A_y, A_z$; Energy of $F_x, F_y, F_z, AE, A_x, A_y, A_z$]	35	35-105-1
Standard deviation	[Stdev of $F_x, F_y, F_z, AE, A_x, A_y, A_z$]	7	7-21-1
Skewness	[Skewness of $F_x, F_y, F_z, AE, A_x, A_y, A_z$]	7	7-21-1
Kurtosis	[Kurtosis of $F_x, F_y, F_z, AE, A_x, A_y, A_z$]	7	7-21-1
Root Mean Square (RMS)	[RMS of $F_x, F_y, F_z, AE, A_x, A_y, A_z$]	7	7-21-1
Energy	[Energy of $F_x, F_y, F_z, AE, A_x, A_y, A_z$]	7	7-21-1

Two different three-layer feed forward back propagation neural network (FF BP NN) architectures were implemented (Table 4.14) by varying the number of input nodes (either 35 or 7) and the number of hidden layer nodes (105 in the case of 35 input nodes and 21 in the case of 7 input nodes, i.e. triple the number of the input nodes). The output layer had only 1 node, yielding a binary value associated with the residual stress condition: 0 = acceptable residual stress and 1 = unacceptable residual stress.

For each of the 14 WPT packets, the NN learning procedures were carried out by using, in turn, the training sets formed by the 130×35 and the five 130×7 sensor fusion wavelet feature vectors matrices as NN input and, as desired NN output, the corresponding 130×1 matrix composed of the binary values identifying the residual stress level (0 = acceptable; 1 = unacceptable) for each of the 130 signal specimens.

In Table 4.18, the NN overall SR is reported for each wavelet packet of the first three WPT levels and each sensor fusion wavelet feature vectors matrix (i.e. each training data set).

As regards the behavior of the 35-elements and 7-elements sensor fusion wavelet feature

vectors, the highest average SR is achieved for the Energy 7-elements wavelet feature vector ($SR_{ave} = 99.67\%$), the second best performance is verified for the 35-elements wavelet feature vector ($SR_{ave} = 98.26\%$), and the Standard Deviation and RMS 7-elements wavelet feature vectors both provide average SR values higher than 94% ($SR_{ave} = 95.06\%$ and 94.27% , respectively). On the contrary, the Skewness and Kurtosis 7-elements wavelet feature vectors display an unsatisfactory performance both in terms of SR_{ave} (66.88% and 71.76% , respectively) and single packet SR values that are never higher than 88% and can fall off as low as 58%.

Thus, although three 7-elements wavelet feature vectors (Energy, Standard Deviations, RMS) provide high NN performance degrees in the sensor fusion based identification of residual stress acceptability, the other two (Skewness, Kurtosis) evidence rather low performance values. This calls for the necessity to examine the behavior of all five 7-elements wavelet feature vectors in order to determine the best performing one (Energy, in the present case).

Finally, by examining the overall NN SR values obtained for the three wavelet packet levels, it can be noticed that the 3rd level packets for each wavelet feature vector type never provide higher SR values than the corresponding 1st and 2nd levels packets, indicating it is unnecessary to proceed to the 3rd level of packet decomposition for the identification of the highest performing packet, thus shortening the WPT feature extraction procedure and related wavelet feature vector selection.

Table 4.18: Overall NN SR for all sensor fusion wavelet feature vectors matrices and wavelet packets: Stdev = Standard Deviation, Sk = Skewness, Ku = Kurtosis, RMS = Root Mean Square, En = Energy.

	130 × 35		130 × 7 matrices			Packet	
	matrix	Stdev	Sk	Ku	RMS	En	average
	(%)	(%)	(%)	(%)	(%)	(%)	(%)
A	99.21	98.75	88.17	84.61	99.29	99.84	94.98
D	88.92	92.60	66.38	73.17	94.83	99.60	85.92
AA	99.69	97.92	83.29	78.38	95.78	99.76	92.47
DA	99.28	97.68	67.84	79.77	97.29	99.76	90.27
AD	99.46	94.31	64.70	71.62	92.22	99.53	86.97
DD	99.76	93.92	61.99	74.31	97.52	99.30	87.80
AAA	99.60	95.37	76.38	69.23	96.52	99.82	89.50
DAA	99.15	93.92	61.99	74.31	97.52	99.30	87.70
ADA	99.46	98.99	59.05	64.54	96.83	99.68	86.43
DDA	99.52	99.29	58.06	67.90	97.82	99.53	87.02
AAD	99.07	92.01	58.38	59.69	90.95	99.76	83.31
DAD	99.46	89.24	63.93	70.93	91.45	99.76	85.80
ADD	99.39	94.37	60.47	68.04	80.24	99.84	83.73
DDD	93.61	92.45	65.63	68.13	91.53	99.84	85.20
Feature average (%)	98.26	95.06	66.88	71.76	94.27	99.67	

4.3. Surface roughness assessment

Many engineering surfaces are manufactured to have functional properties such as bearing and sealing, or to have high fluid retention capabilities. According to the requirements of the engineering application, a functional surface has to have some specific topographic features that are beneficial to the application. Structural properties in particular are strongly related to functional requirements, and the measurement of such surfaces is very important, not only for the functionality of the products, but also as a feedback for the manufacturing units.

The development of surface metrology is traditionally based on tactile methods, which gather data by physical contact with the surface. Although this type of analysis is adequate for most applications, tactile methods are generally time-consuming and can damage the workpiece. Furthermore, the shape and the size of the stylus can limit its capacity to penetrate into surface structures and show their properties.

4.3.1 Generalities

Surface metrology is the measurement of miniature-scale features of the surface of a work piece. These measured features are used to study the deviations of the work piece surface from its desired shape. These features include deviations from roundness, straightness, flatness, cylindrical ... [168].

The output of measuring a work piece surface is a set of geometrical details and are considered to be the topography of the surface. The topography characterization process is composed of three stages: measurement, visualization, and quantification.

After measuring the surface, the surface topography analysis starts with visualization, in order to have a realistic representation of the surface. Following that is the quantitative assessment of surface texture. This stage can be very useful for process control, tolerance verification, and functional analysis.

Surface topography is composed of the basic components obtained from the breakdown of the surface geometry. Three types of deviations can be identified [168] as follows and are shown in Figure 4.30:

- *Roughness*: irregularities resulting from manufacturing process.
- *Waviness*: irregularities resulting from improper manufacture.
- *Very long waves*: irregularities resulting from errors in sideways or thermal distortion

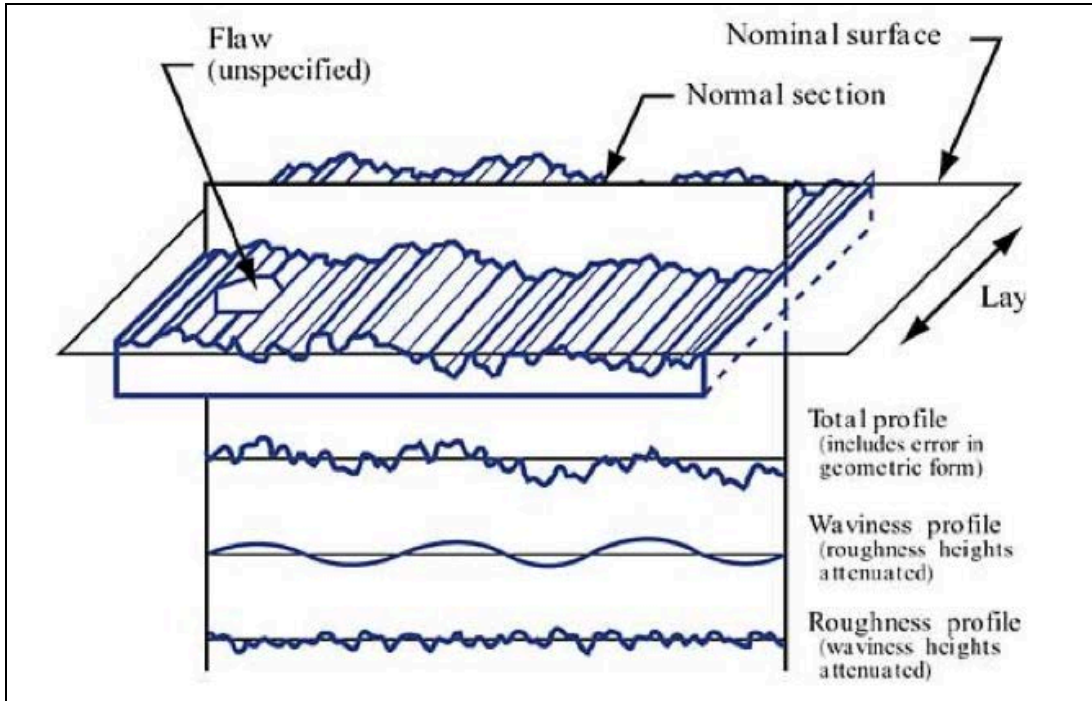


Figure 4.30: Geometric deviations on the workpiece surface [168].

There are several techniques for surface measurements. The principal methods are stylus profilometry, optical scanning techniques as well as other techniques, i.e. atomic force microscopy. Furthermore, the surface measurements instruments can be classified as contact and non-contact surface measurement instruments. Stylus instruments are contact measuring instruments and, instead, optical instruments are non-contact measuring instruments. Using these instruments, it is possible to get 2D as well as 3D measurements.

Roughness parameters

Roughness is the deviation caused by the action of the cutting tool or the machining and results as process marks. The resulting surface roughness is the outcome of the process parameters such as the used cutting parameters and the chosen tool geometry.

There are several parameters of surface roughness are described in the standards ISO 4287 and ISO 4288. The most common parameters in the manufacturing industry are the following [169] and are illustrated in Figure 4.31 [170].

R_a : the arithmetical mean deviation of the assessed profile.

$$R_a = \frac{1}{n} \sum_{i=1}^n |y_i|$$

R_q : root mean square of the measured profile heights.

$$R_q = \sqrt{\frac{1}{n} \sum_{i=1}^n y_i^2}$$

R_v : Maximum depth of the profile below the mean line with the sampling length.

$$R_v = \min_i y_i$$

R_p : Maximum height of the profile above the mean line within the sampling length.

$$R_p = \max_i y_i$$

R_t : maximum height of the profile.

$$R_t = R_p - R_v$$

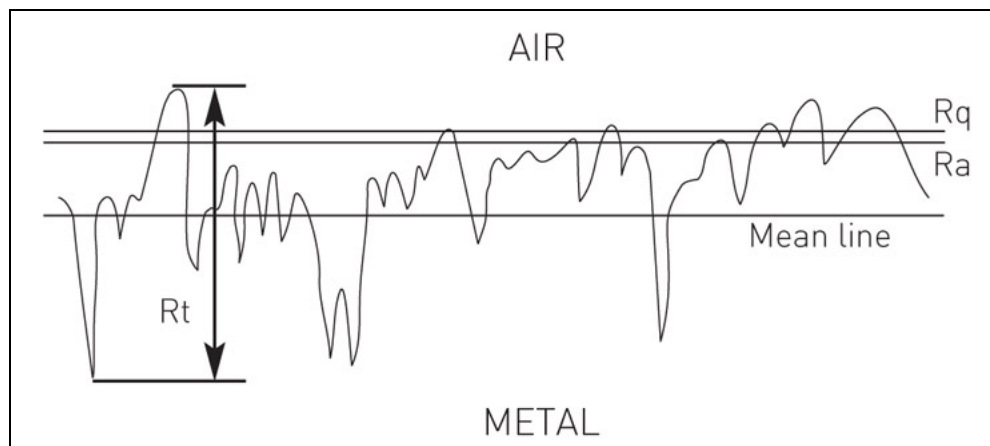


Figure 4.31: A scheme illustrating the surface roughness parameters [170].

Filters are needed to separate roughness from waviness and form. Such filter is called a phase correct filter or better known as the so-called Gaussian filter [171].

The Gaussian filter takes into consideration the following assumptions:

- The measured profile is cut at the boundaries from both sides to remove the effect of boundary distortion.
- The form has been removed before filtering.
- The surface texture is assumed to be almost symmetric [172].

The weighing function $s(x)$ of the filter is symmetrical and has the characteristics of the Gaussian distribution:

$$s(x) = \frac{1}{\alpha \lambda_c} \cdot \exp \left[-\pi \left(\frac{x}{\alpha \lambda_c} \right)^2 \right]$$

where λ_c is the cut – off wavelength and is constant equal to 0.4697 [173].

Modern filters operate with digital Gaussian cut-off filters based on a cut-off length and express the transmission properties in nominal wavelengths, which are:

- λ_s “s” refers to sampling and defines the intersection between the roughness and the even shorter wave components present in a surface;
- λ_c “c” refers to cut-off and defines the intersection between the roughness and waviness components;
- λ_f “f” refers to form and defines the intersection between the waviness and the even longer wave components present in a surface (Figure 4.32) [173].

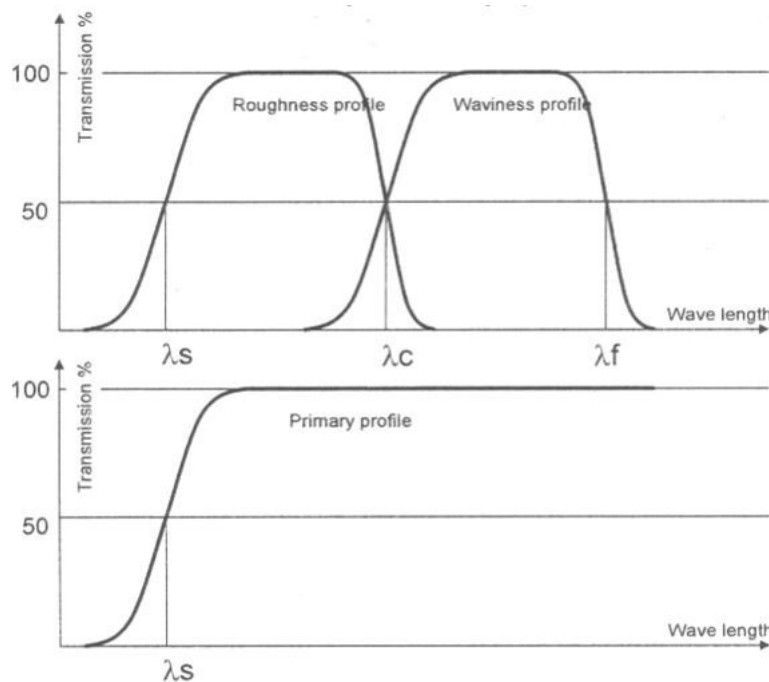


Figure 4.32: Transmission characteristic for roughness, waviness and primary profile [173].

The filtering process is illustrated in Figure 4.33 and summarized below:

- A form fit is applied to the data to remove the form.
- The ultrashort wave component is then removed using the λ_s filter.
- The Primary profile is then passed through a λ_c filter, which separates the waviness form from the roughness [174].

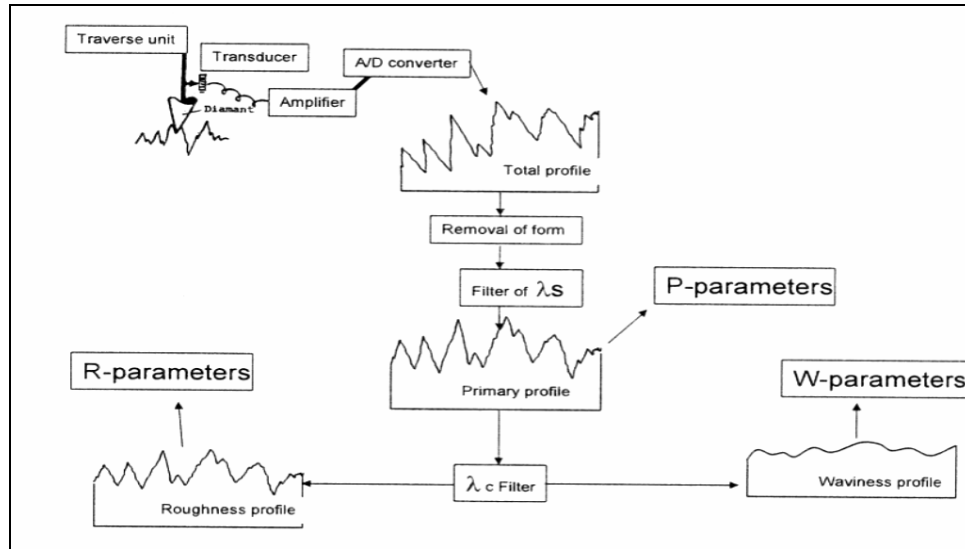


Figure 4.33: Filtering process [174].

4.3.2 Surface roughness measurement techniques

The techniques used for roughness measurements can be divided into two types of techniques: profiling and area averaging.

Profiling techniques measure surface heights point by point with a high-resolution probe. Some examples of high-resolution probes are a stylus or a focused optical beam. These techniques are accurate and quantitative. The measured surface profiles can be used to generate statistical parameters and find surface functions that characterize the average peak to height or peak spacing [175].

Part 6 of the standard ISO 25178 [171] defines three classes of methods for surface texture measuring instruments (Figure 4.34):

- *Line profiling method* produces a 2D profile of the surface irregularities represented as a height function.
- *Areal Topography method* produces a topographical image of the surface represented mathematically as a height function.
- *Area – integrating method* measures a representative area of a surface and produce numerical results that depend on area-integrated properties of the surface texture [175].

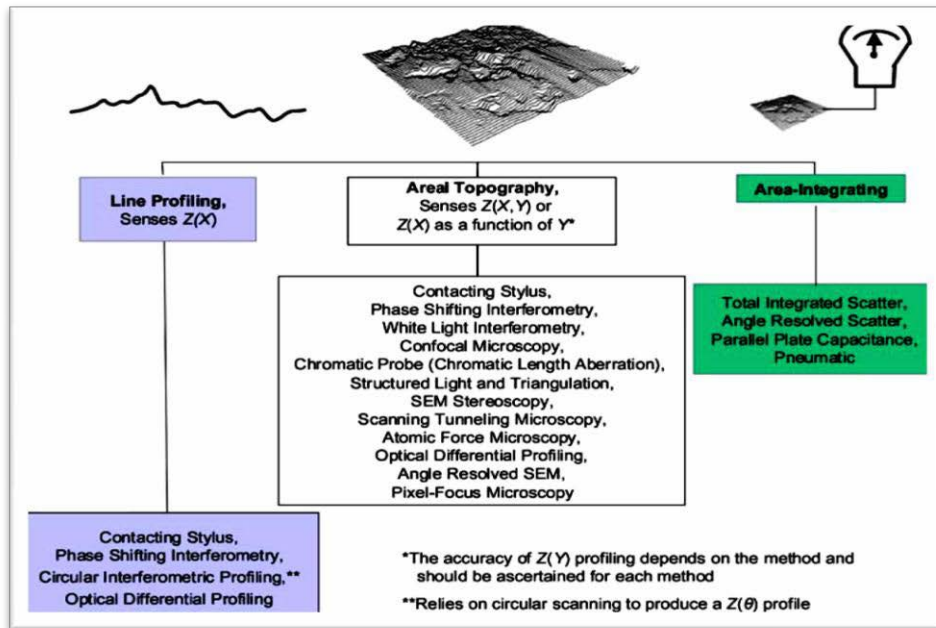


Figure 4.34: A classification of surface texture measurement methods with example [175].

The so-called “traced profile” [178] recorded by the stylus instrument is the locus of the center of the stylus (Figure 4.36). If the contacting portion of the stylus is assumed spherical, the effective profile will correspond to the contacting envelope. The stylus tip is unable to follow the surface when the radius of curvature is exaggerated and a valley is represented as a cusp (Figure 4.36).

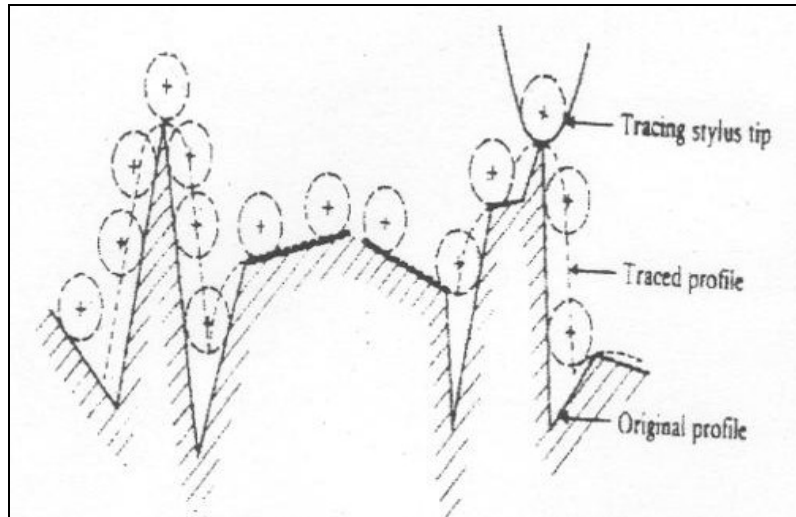


Figure 4.36: Influence of tip radius and angles [178].

Optical techniques

Optical profilers are not contact methods and avoid the potential of surface damage associated with the stylus that comes into contact with the surface. The following summarize the important issues in all optical methods:

- *Material response:* optical probing is only possible when a signal above the threshold of the detector is received. Therefore, the material’s reflectivity is extremely important.
- *Lateral resolution:* this is limited by light diffraction. Given a numerical aperture NA and a light wavelength λ , the limit d is given by:

$$d = \frac{1.22\lambda}{NA}$$

- *Maximum detectable slope:* this depends on the kind of reflection (specular or diffused), which in turn depends on the surface topography and material, as well as on the objective working distance and numerical aperture.
- *Wavelength of full amplitude modulation:* This quantity is intended as the maximum aspect ratio of a measurable surface structure.

One of the more commonly known and used instrument is the optical stylus profilometer [179].

An **Optical Stylus Profilometer** (Figure 4.36) is based on the idea of an auto-focusing signal of a laser beam detector. This laser beam with a spot diameter of about $1\ \mu\text{m}$ and is focused into a point on the surface through a lens which collects the scattered light on a focus detector. The detector operates a control system, modifying the distance of the lens from the surface so as to keep the beam focused. Consequently, the movement of the lens follows the surface at a constant distance and its trajectory describes the surface profile.

The measurements obtained with the auto/focusing method do not always correlate very well with those obtained with stylus method. In fact, this method tends to overestimate the peak heights; whereas the stylus method underestimates the valley heights of the surface.

The maximum detectable slope using an autofocusing stylus instrument is approximately 15° [179].

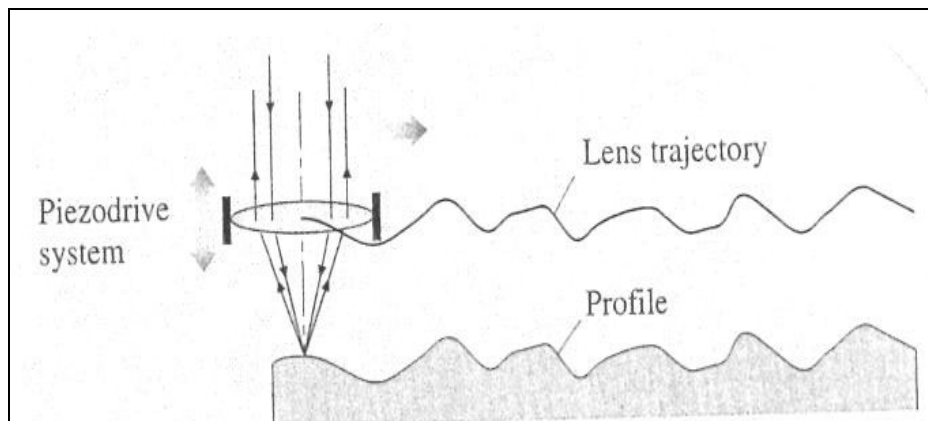


Figure 4.36: Operating principle of the auto-focusing method [179].

Comparison between stylus profilometer and optical stylus

Table 4.19 shows the significant differences between stylus profilometer and optical stylus.

Table 4.19: Comparison of two techniques.

Stylus Profilometer	Optical Stylus
Contact	Non-contact
Not suitable for fine surface	Suitable for fine surface
Not suitable for soft surface	Suitable for soft surface
Not depends from material's reflectivity	Not suitable for material with low

Recent Optical technique

Focus variation instruments represent another technique, which has been recently introduced in the field of surface metrology. In focus variation instruments, white light is emitted from a source and transmitted through the semi – transparent mirror and the objective lens to the specimen. Depending on the topography of the specimen, the light is reflected in different direction. The reflected light is partly collected by the objective in different direction. Due to the small depth of field of the optics, only small regions of the object are sharply imaged; therefore, in order to completely detect surface information, the optical arrangement is moved along the vertical direction while continuously capturing data. One example of the optical instruments is Alicona Infinite Focus shown in Figure 4.37 [179].



Figure 4.37: Focus variation instrument (Alicona Infinite Focus) [175].

Recent techniques

For high resolution surface investigations, two commonly used techniques are Atomic Force Microscopy (AFM) and Scanning Electron Microscopy (SEM). Each of these techniques detects surface features at a nanometer scale.

Scanning Electron Microscope (SEM)

The working principle of the SEM (Figure 4.38) consists of applying a voltage between a conductive sample and filament, resulting in electron emission from the filament to the sample. This occurs in a vacuum environment ranging from to Torr (1torr = 133.3Pa).

The resolution and depth of field of the image are determined by the beam current and the final spot size, which are adjusted with one or more condenser lenses and the final, probe forming objective lenses. The lenses are also used to shape the beam to minimize the effects of spherical aberration, chromatic aberration or diffraction [180].

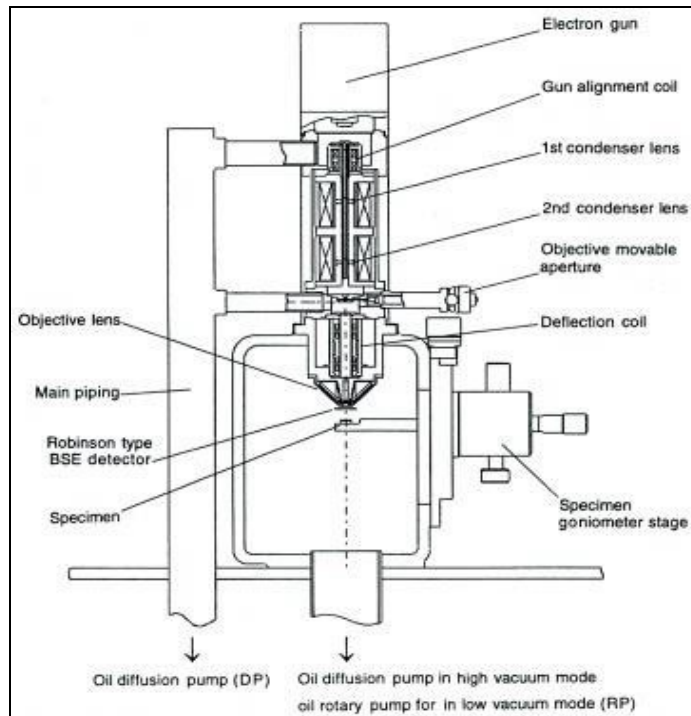


Figure 4.38: Scanning Electron Microscope [180].

Atomic Force Microscopy (AFM)

The working principle of the AFM (Figure 4.39) consists in a scanning sharp tip at the end of a flexible cantilever across a sample surface while maintaining a small force constant.

The scanning motion is conducted by a piezoelectric tube scanner, which scans the tip in a raster pattern with respect to the sample. The tip-sample interaction is monitored by reflecting a laser off the back of the cantilever into a split photodiode detector. By detecting the difference in the photodiode detector output voltage, changes in the cantilever deflection or oscillation are determined [180].

Comparison of two techniques: Atomic Force Microscope and Scanning Electron Microscope

In the SEM, image changes in slope can result in an increase in electron emission from the sample surface, producing a higher intensity in the image. However, it can sometimes be difficult to determine whether a feature is sloping up or down.

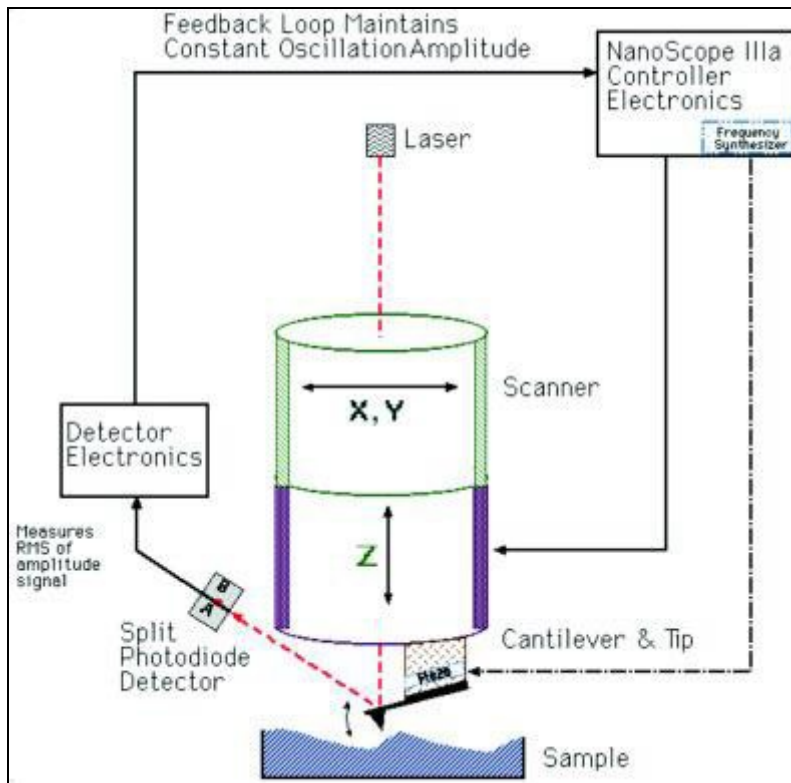


Figure 4.39: Atomic Force Microscope [180].

In Figure 4.40, in the left figure, it is difficult to determine whether the small round structures are bumps or pits. The AFM (Figure 4.40 on the right) data contains instead height information.

One of the key advantages of the SEM with respect to other types of microscopy is its large depth fields (Figure 4.40). This ability makes it possible to image very rough surfaces with millimeters of vertical information within a single image. This ability also makes it possible to measure very rough surfaces over larger lateral areas as well.

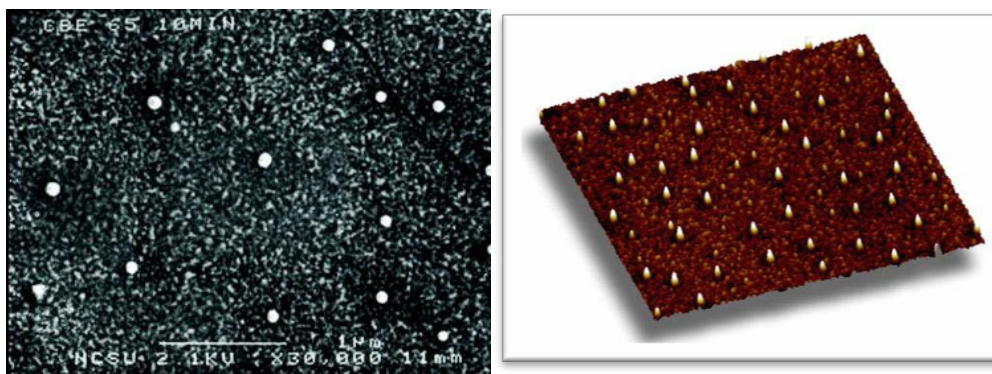


Figure 4.40: on the left: SEM Image, on the right: AFM image [180].

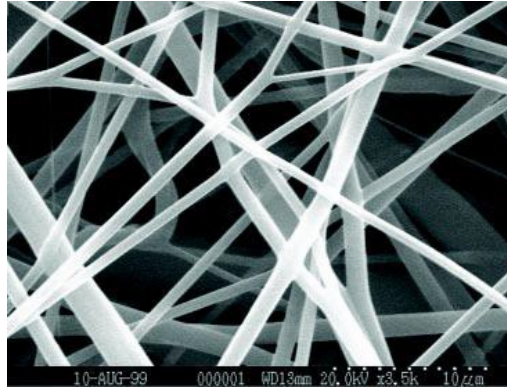


Figure 4.41: SEM image [180].

Both SEM and AFM are associated with techniques which can provide compositional information through analyzing materials and physical properties of the sample [180].

Consideration when choosing a Method

There are many factors that need to be considered when choosing a method for measuring surface texture. The list below illustrates these factors.

- **What type of surfaces is needed to be measured.** It may be needed a specific instrument to measure a single type of surface in production, or a generic instrument to measure a whole range of surfaces.
- **What surface geometries are needed to be measured.** For spatial wavelengths less around 500 nm only SEM can be used, but such methods will only have limited height ranges.
- **What surface materials are measured.** This includes the material hardness, optical characteristic, electrical and chemical characteristic. For example, if the surface is soft, then this may prohibit the use of a stylus instrument.
- **The overall size of an object.** Some instruments have a limited size of object that can be placed on the measurement table for example some optical instrument will have limited object height due to the finite stand-off of the objective lenses
- **How fast must be the measurement.** Optical methods tend to have shorter measurement times than stylus instrument, especially where areal measurements are required. The time to prepare the sample may also be important, for example, when using an SEM, it is necessary to apply a conducting coating to a dielectric sample and allow time to pump the instrument down to the required level of vacuum.
- **The financial budget.** Surface texture measuring instruments can range from a few thousand euros for a simple hand/held stylus instrument to a several hundred thousand euros for optical instruments with product support and characterization software [175].

4.3.3 Experimental setup and procedure

The desired surface roughness is usually obtained by polishing the product work piece. Polishing experiments were conducted at Strecon A/S under the FP7 European project IFaCOM (FoF NMP – 285489), Intelligent Fault Correction and self-Optimizing Manufacturing systems.

Machine tool

The machine tool employed for the polishing experiment is the ABB Robot Assisted Polishing Machine, RAP, shown in Figure 4.45 below.

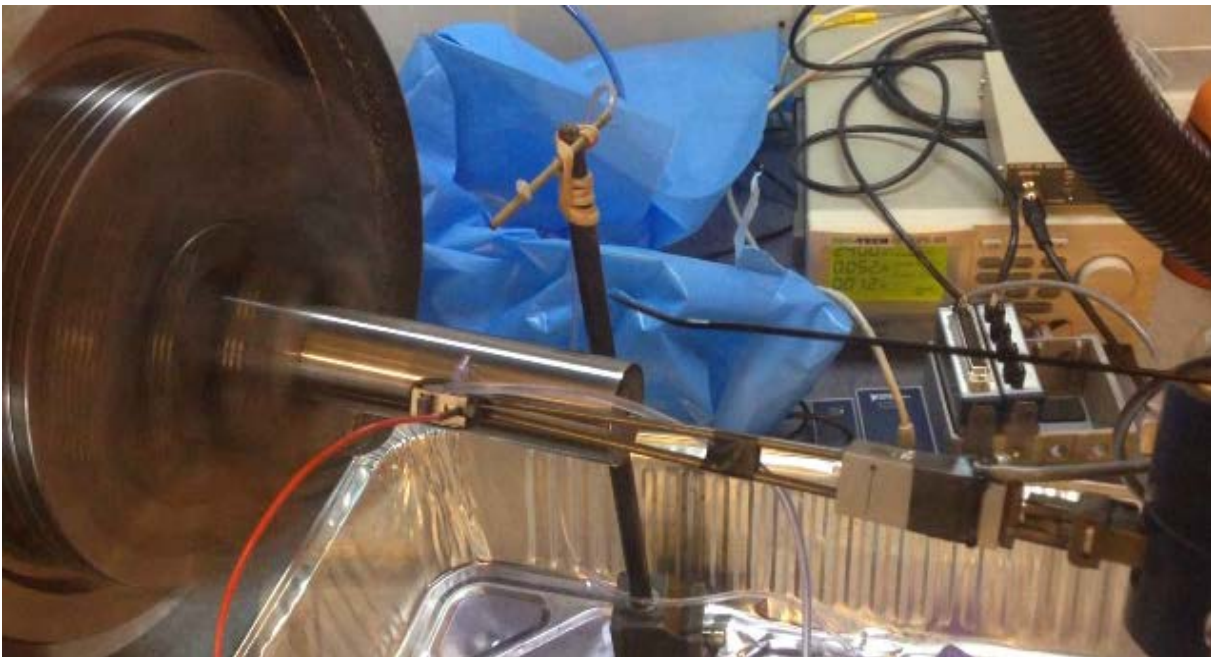


Figure 4.42: Strecon's RAP machine.

Work Material

The work material is AISI 52100 alloy steel, also called high performance bearing steel.

Table 4.20: Typical analysis in percent.

Fe:	96.5-97.32
Cr:	1.3-1.6
C:	0.98-1.1
Mn:	0.25-0.45
Si:	0.15-0.3
S:	≤ 0.025
P:	≤ 0.025

Table 4.21: 52100 Alloy Steels physical properties.

Density	7.81 g/cm ³
Melting point:	1424°C
Specific heat:	475 J/kg·K
Average Coefficient of Thermal Expansion:	11.9 μm/m·K
Thermal Conductivity:	46.6 W/m·K
Electrical Resistivity:	2190 n·m

Table 4.22: 52100 Alloy Steels mechanical properties.

At room temperature	
Ultimate tensile strength	1748 MPa
Yield strength	1394 MPa
Elongation in 50 mm	11 %
Elastic modulus (Tension)	200 GPa
Hardness	60-67 HRC

Workpiece

The workpiece, called Unimax roll 1, is made of AISI 52100 alloy steel. It is a 75 mm long cylinder that was turned and is ready for polishing. Figure 4.43 shows several samples of unimax rolls including unimax roll 1 used in this experiment.



Figure 4.43: Test rolls.

Polishing stone

The stone used for polishing is a Gesswein #800 polishing stone (MP800) (Figure 4.44).



Figure 4.44: Set of polishing stones.

Sensor Monitoring System

The sensors are mounted on the machine as shown in the Figure 4.45 below:



Figure 4.45: Sensors mounted on the RAP machine.

The current sensor is in the electrical cabinet so it is not seen here. The drop system is controlling the amount of lubrication on the surface, it is controlled by the RAP software. The sensors are listed in the table below.

Table 4.23: Sensor list.

	Sensor type
Acoustic Emission	Fuji Ceramics Corporation R-CAST M304A sensor + A1200 pre-amplifier
Strain	strain gauge sensor
Voltage	Voltage sensor is in the electrical cabinet

The sensor data obtained during the experiment were exported into .txt files and are listed in Table 4.24 below.

Table 4.24: Sensor signal file titles.

SensorData.AE	Raw AE	cDAQ9184-18968C9Mod2.ai0	AE signal +-10v, 1 msp, 16bit
SensorData.Strain_Rms	RMS of strain signal	cDAQ9184-18968C9Mod1.ai0	Strain raw value 50 ksp, 24bit
SensorData.Voltage_Avg	Avg of the voltage flowing into the pulse motor	cDAQ9191Mod1.ai0	Current (scale vars) 50 ksp +-10v

Polishing sessions

Cutting parameters: Main spindle = 300 rpm, Feed = 5mm/s, Polishing force = 1800 or 1000g, Oscillation = 500 pulses pr. min, Stroke = 1mm

The full length of Unimax roll U1 was polished over and over using:

- 1800 grams 1 × 60passes
- 1000 grams 3 × 60 passes
- 1800 grams 1 (2) × 60 passes

Six polishing sessions of 60 passes were carried out; the duration of each polishing session was about 15 minutes and 50 seconds. For each polishing session the AE, Strain and Current sensor signals were detected and stored as txt file. Each txt file contains a number of samplings per file variable according to the sensor signal type (Table 4.25).

Table 4.25: Number of samplings for each sensor signal data type.

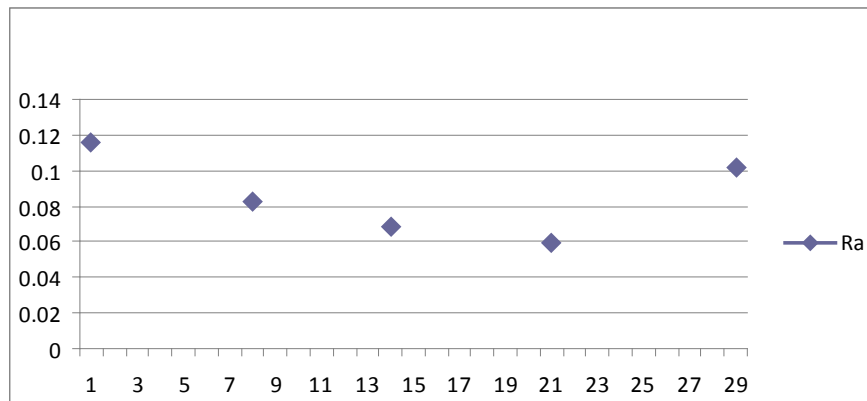
Sensor data	Number of samplings per file
AE	131.072
Current	100
Strain	16.384

Roughness Measurements

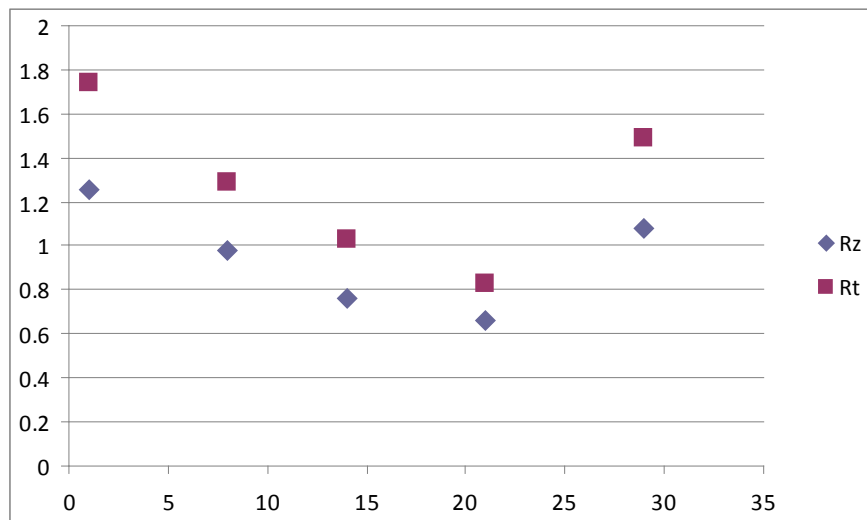
The roughness values (R_a , R_z , R_t) were measured at the end of each set of 60 polishing passes (except the last one) and their medium values are reported (Table 4.23) and are plotted in Figure 4.46.

Table 4.26: Roughness measurements.

Polishing Force	Roughness Values		
	R_a	R_z	R_t
1800g	0.111	1.131	1.684
1000g	0.081	0.984	1.582
1000g	0.083	0.908	1.065
1000g	0.053	0.603	0.742
1800g	0.107	1.076	1.643



(a)



(b)

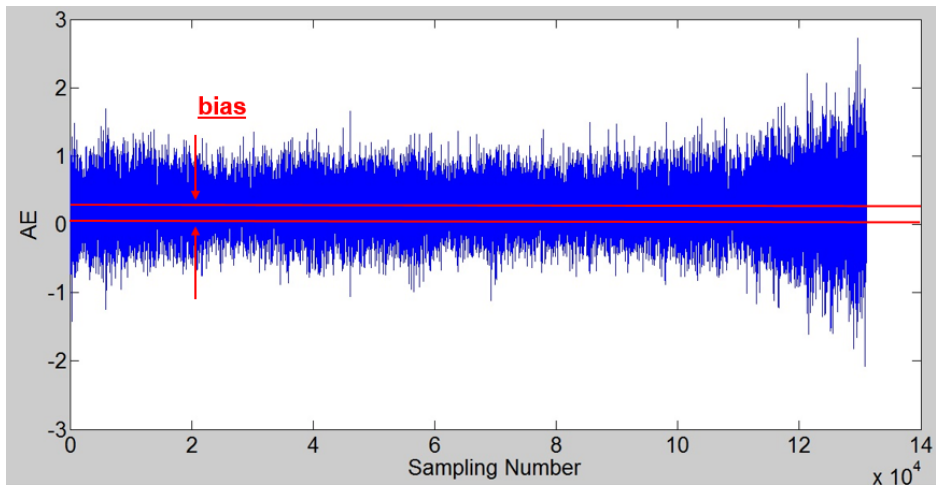
Figure 4.46: Roughness measurements plotted.

4.3.4 Sensor signal data analysis

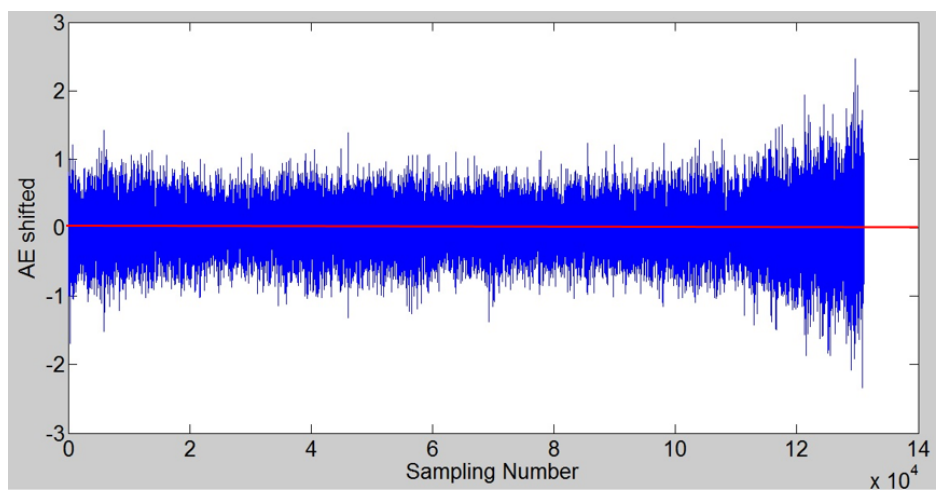
The sensor signal processing procedure was carried out in Matlab ®.

The following was applied only to AE sensor signal because the received AE sensor signals showed an offset that needed to be removed. The procedure shown in Figure 4.47 consisted in:

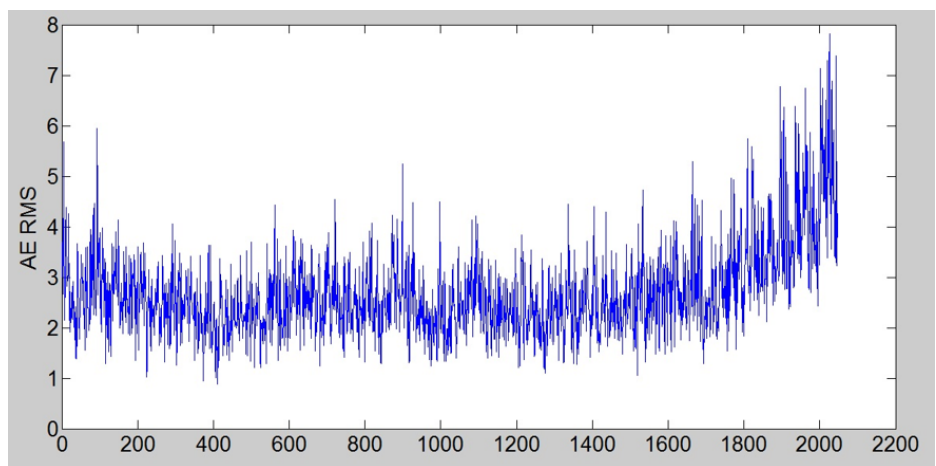
- Plotting of AE raw signal
- Shifting of AE raw signals: for each AE raw signal a mean value was calculated and this value was subtracted from the entire signal in order to obtain the typical AE signal oscillating around zero (the AE raw signal presented an offset)
- Calculating the AE RMS signals



(a)



(b)



(c)

Figure 4.47: (a) Acoustic Emission Raw Signal; (b) Acoustic Emission Level Shifted Raw Signal; (c) Acoustic Emission RMS signal.

Sensor Signal Features Extraction

For each sensor signal (AE, Strain, Current) two signal features extraction procedures were applied.

- Statistical features
- Wavelet features

Statistical Features Extraction

The statistical features extracted for each sensor signals were:

- Mean
- Variance
- Skewness
- Kurtosis
- Energy

Wavelet Features Extraction

A wavelet packet transform (WPT) was used for feature extraction. The WPT of a sensor signal generates packets of coefficients calculated by scaling and shifting a chosen mother wavelet, which is a prototype function. In this way, at the 1st level of WPT the original sensor signal S is split into two frequency band packets, called approximation A_1 and detail D_1 . At the 2nd level, each approximation and detail packet are again split into further approximations, AA_2 and AD_2 , and details, DA_2 and DD_2 , and the process is repeated generating other decomposition packets of the same tree.

The employed mother wavelet is a Daubechies 3 denoted by “db3”. The decomposition was performed up to the 3rd level, yielding 14 packets. For each packet, 5 packet features.

Sensor Features Pattern Vector

In all, 20 statistical features were extracted from them. These features were used to construct sensor fusion pattern vectors which are vectors used for decision making combining features from different sensor signal types. In the construction of sensor fusion pattern vectors, however, only one type of AE signals was used at a time to avoid sensorial data redundancy: either AE_{raw} or AE_{rms} . Thus, two kinds of sensor fusion pattern vectors were constructed including conventional features from either (a) strain, voltage and AE_{raw} ; or (b) strain, voltage and AE_{rms} . Figures 4.48 and 4.49 illustrate the two kinds of constructed sensor fusion pattern vectors.

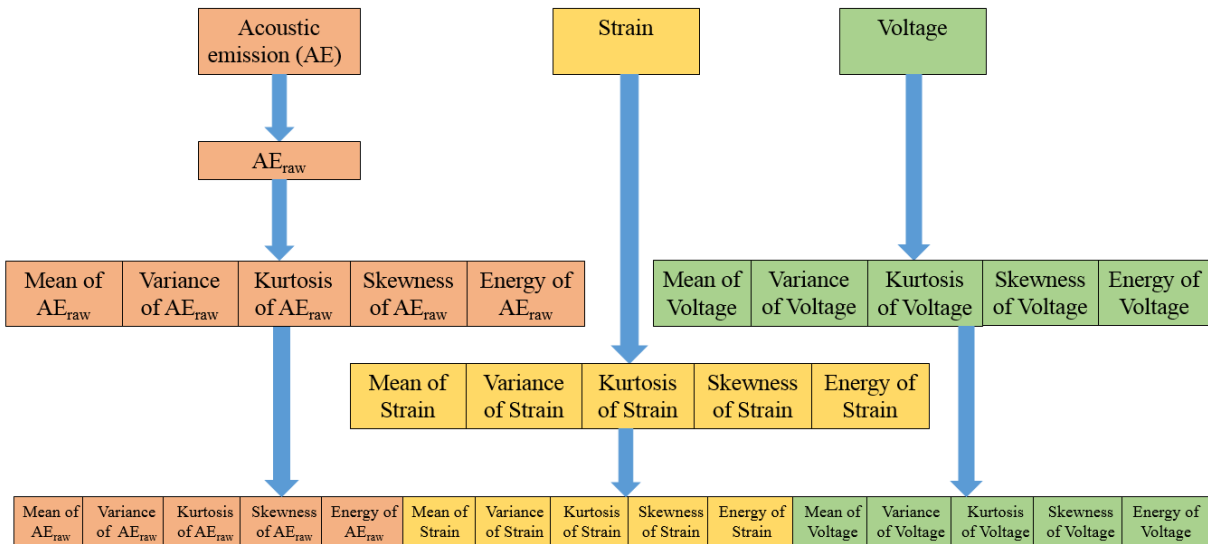


Figure 4.48: Sensor fusion pattern vector construction using AE_{raw} .

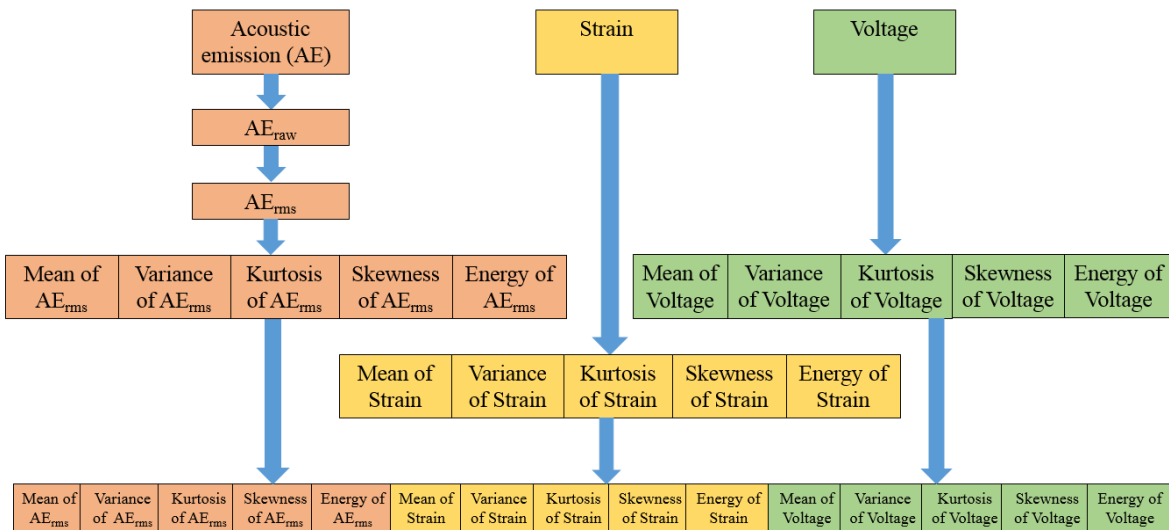


Figure 4.49: Sensor fusion pattern vector construction using AE_{rms} .

An overall of 20 wavelet packet transform feature vectors is obtained. Using a sensor fusion approach, the 20 wavelet packet transform feature vectors are used for the construction of 2 different sensor fusion patterns. The figures (Figure 4.50 and 4.51) below illustrates the 2 types of sensor fusion patterns obtained from packet A.

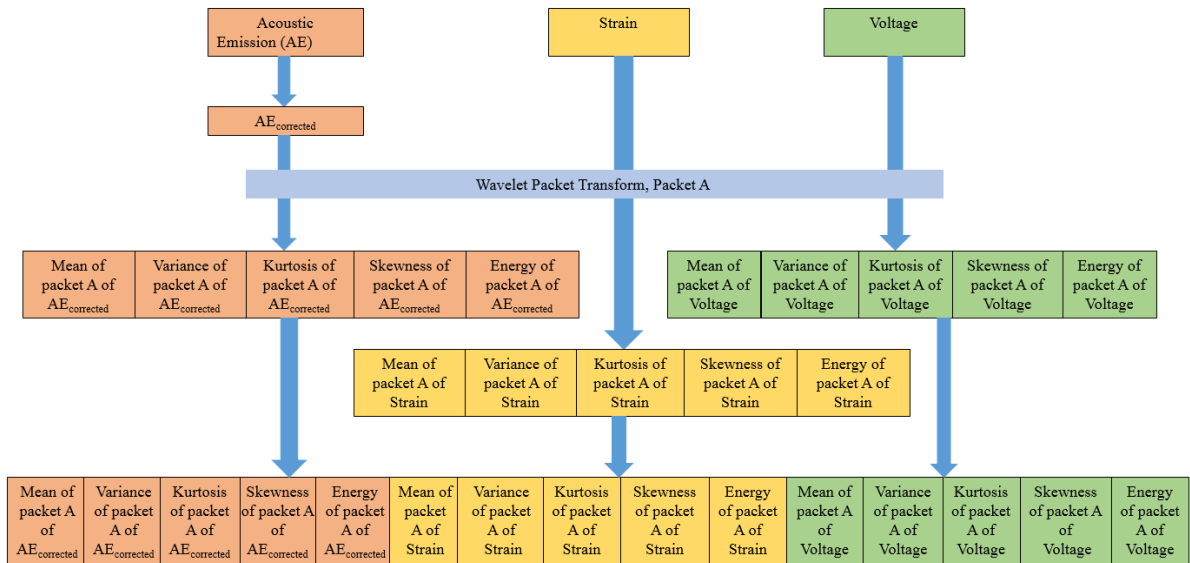


Figure 4.50: Sensor fusion pattern construction using the AE_{raw} and packet A.

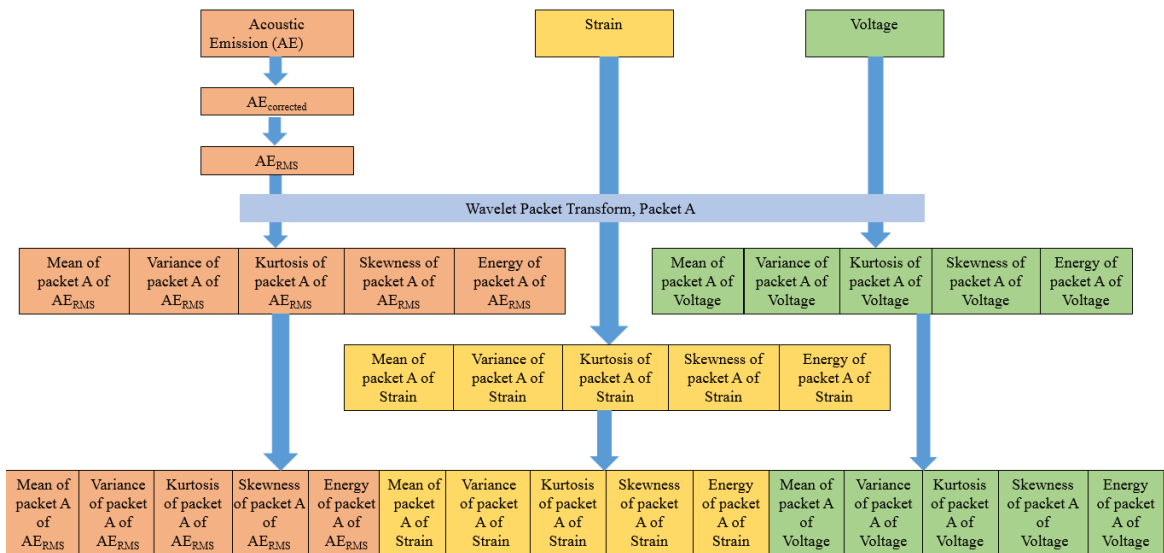


Figure 4.51: Sensor fusion pattern construction using the AE_{RMS} and packet A.

In table 4.27, sensor fusion pattern vectors resulting from the statistical features are listed.

Table 4.27: Sensor fusion pattern vectors using statistical features.

	AE	Strain	Voltage
AE_{raw}	Mean, Variance, Skewness, Kurtosis, and Energy.	Mean, Variance, Skewness, Kurtosis, and Energy.	Mean, Variance, Skewness, Kurtosis, and Energy.
AE_{RMS}	Mean, Variance, Skewness, Kurtosis, and Energy.	Mean, Variance, Skewness, Kurtosis, and Energy.	Mean, Variance, Skewness, Kurtosis, and Energy.

In table 4.28, all possible combinations of the sensor fusion pattern vectors resulting from the wavelet packet transform (WPT) analysis are listed.

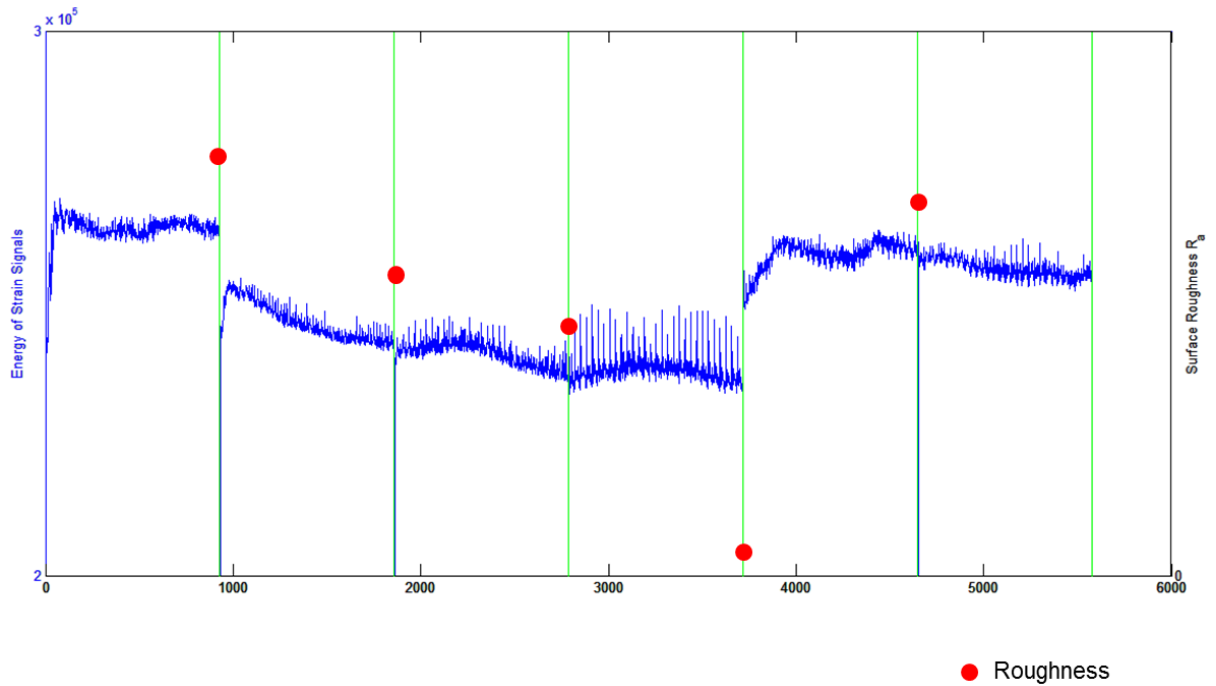
All in all, 30 sensor fusion pattern vectors were constructed and were used for knowledge based decision making.

Table 4.28: WPT sensor fusion pattern vectors.

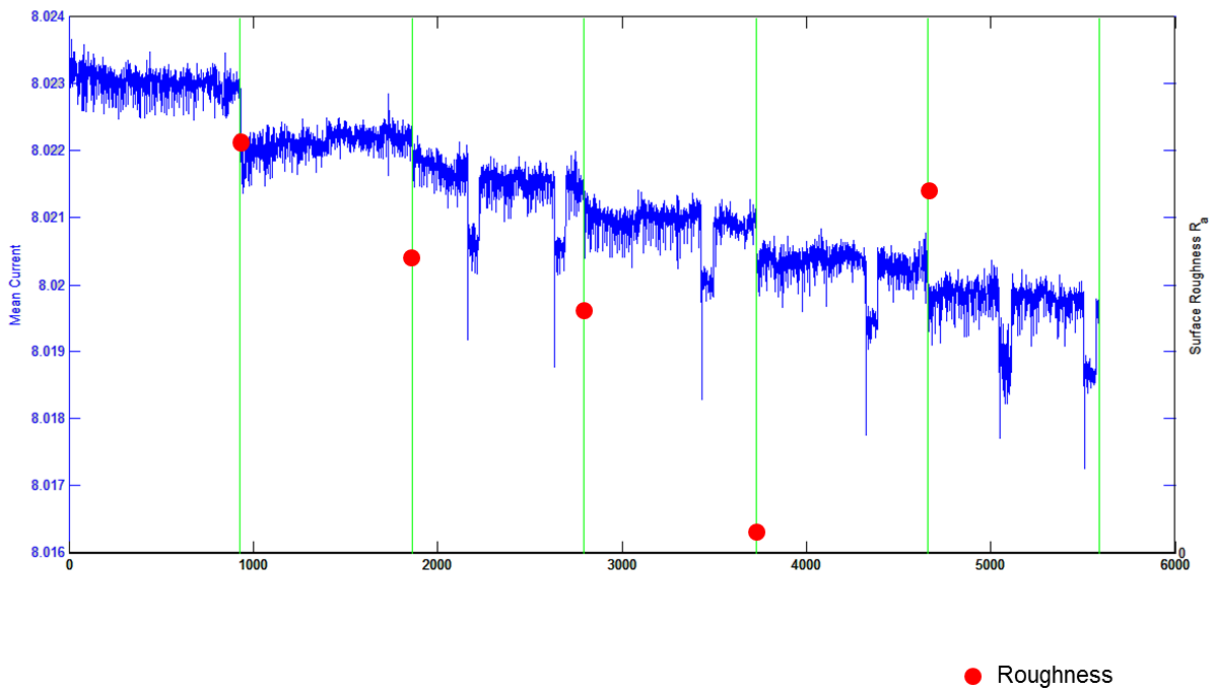
	AE_{raw}/AE_{RMS}	Strain	Voltage
A	Mean, Variance, Skewness, Kurtosis, and Energy.	Mean, Variance, Skewness, Kurtosis, and Energy.	Mean, Variance, Skewness, Kurtosis, and Energy.
D	Mean, Variance, Skewness, Kurtosis, and Energy.	Mean, Variance, Skewness, Kurtosis, and Energy.	Mean, Variance, Skewness, Kurtosis, and Energy.
AA	Mean, Variance, Skewness, Kurtosis, and Energy.	Mean, Variance, Skewness, Kurtosis, and Energy.	Mean, Variance, Skewness, Kurtosis, and Energy.
AD	Mean, Variance, Skewness, Kurtosis, and Energy.	Mean, Variance, Skewness, Kurtosis, and Energy.	Mean, Variance, Skewness, Kurtosis, and Energy.
DA	Mean, Variance, Skewness, Kurtosis, and Energy.	Mean, Variance, Skewness, Kurtosis, and Energy.	Mean, Variance, Skewness, Kurtosis, and Energy.
DD	Mean, Variance, Skewness, Kurtosis, and Energy.	Mean, Variance, Skewness, Kurtosis, and Energy.	Mean, Variance, Skewness, Kurtosis, and Energy.
AAA	Mean, Variance, Skewness, Kurtosis, and Energy.	Mean, Variance, Skewness, Kurtosis, and Energy.	Mean, Variance, Skewness, Kurtosis, and Energy.
DAA	Mean, Variance, Skewness, Kurtosis, and Energy.	Mean, Variance, Skewness, Kurtosis, and Energy.	Mean, Variance, Skewness, Kurtosis, and Energy.
ADA	Mean, Variance, Skewness, Kurtosis, and Energy.	Mean, Variance, Skewness, Kurtosis, and Energy.	Mean, Variance, Skewness, Kurtosis, and Energy.
ADD	Mean, Variance, Skewness, Kurtosis, and Energy.	Mean, Variance, Skewness, Kurtosis, and Energy.	Mean, Variance, Skewness, Kurtosis, and Energy.
AAD	Mean, Variance, Skewness, Kurtosis, and Energy.	Mean, Variance, Skewness, Kurtosis, and Energy.	Mean, Variance, Skewness, Kurtosis, and Energy.
DAD	Mean, Variance, Skewness, Kurtosis, and Energy.	Mean, Variance, Skewness, Kurtosis, and Energy.	Mean, Variance, Skewness, Kurtosis, and Energy.
ADD	Mean, Variance, Skewness, Kurtosis, and Energy.	Mean, Variance, Skewness, Kurtosis, and Energy.	Mean, Variance, Skewness, Kurtosis, and Energy.
DDD	Mean, Variance, Skewness, Kurtosis, and Energy.	Mean, Variance, Skewness, Kurtosis, and Energy.	Mean, Variance, Skewness, Kurtosis, and Energy.

4.3.5 Decision making and results

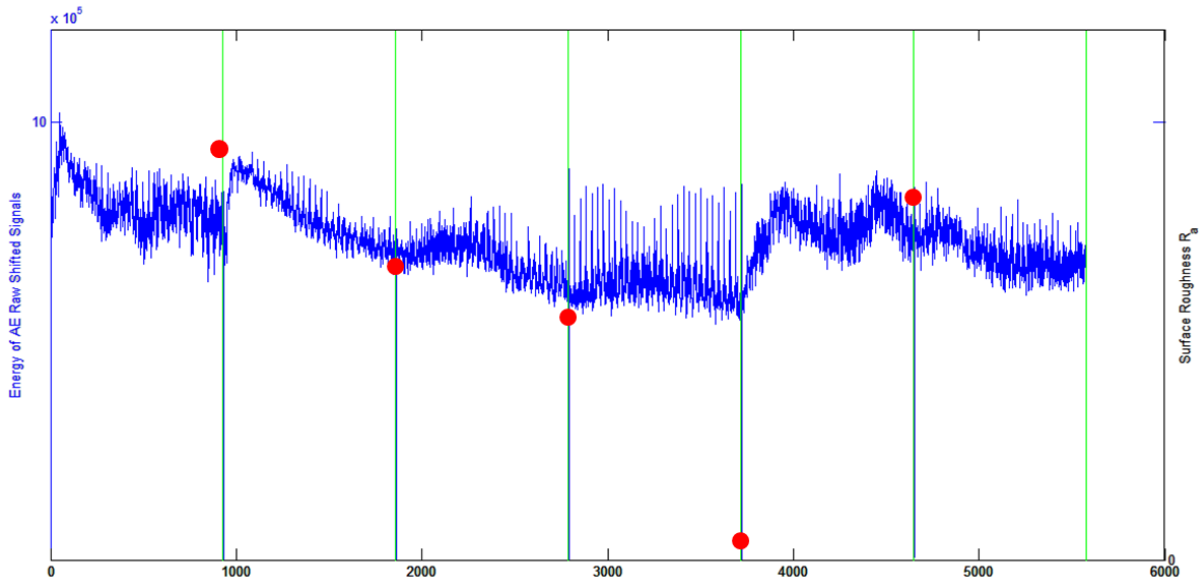
The surface roughness measurements were correlated to the extracted feature vector. The aim is to be able to predict when the required surface roughness has reached. A similar trend between the surface roughness and the extracted feature vector has been noted. In figure 4.52, some examples illustrating the extracted feature vector with the associated surface roughness measurements are shown. The green lines divide the sensor signals into the 6 sets of passes. The red dots represent the surface roughness measured after a given set of passes is over.



(a)

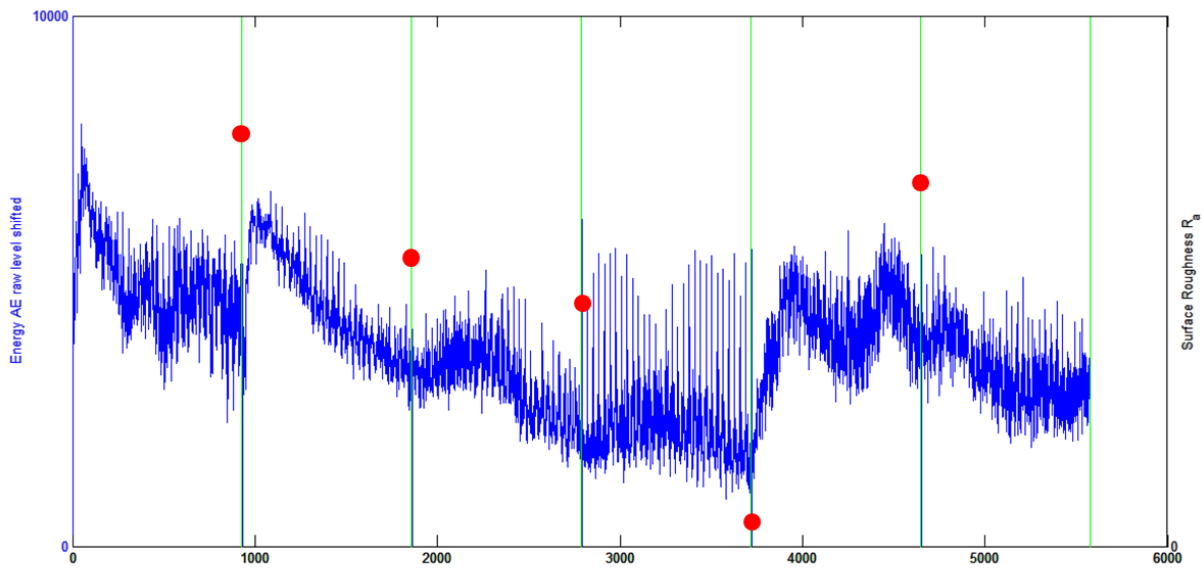


(b)



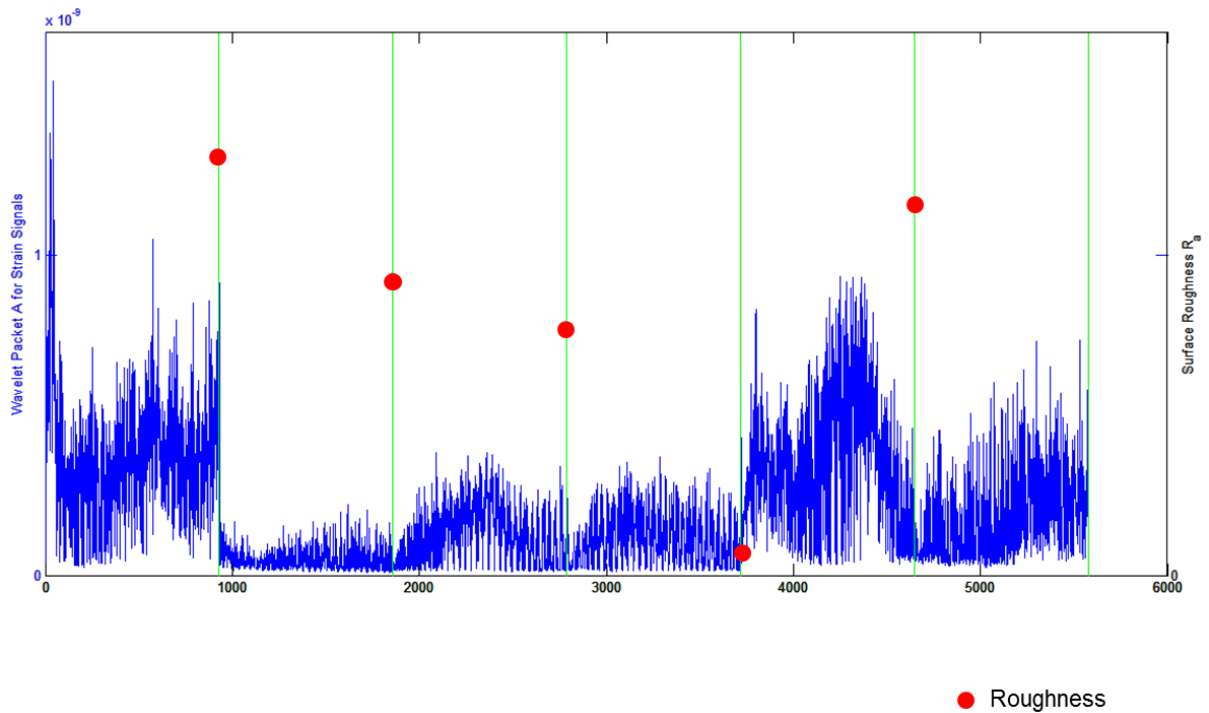
● Roughness

(c)



● Roughness

(d)



(e)

Figure 4.52: (a) Energy of strain signals; (b) Mean of current signals; (c) Energy of the AE_{raw} signals; (d) Energy of the AE_{rms} signals; (e) Mean of the wavelet packet A of strain signals.

Drawing a straight line between the subsequent surface roughness, the notice the trend that is shown below in Figure 4.53. The yellow lines are used to divide the signals into the sets of 60 passes.

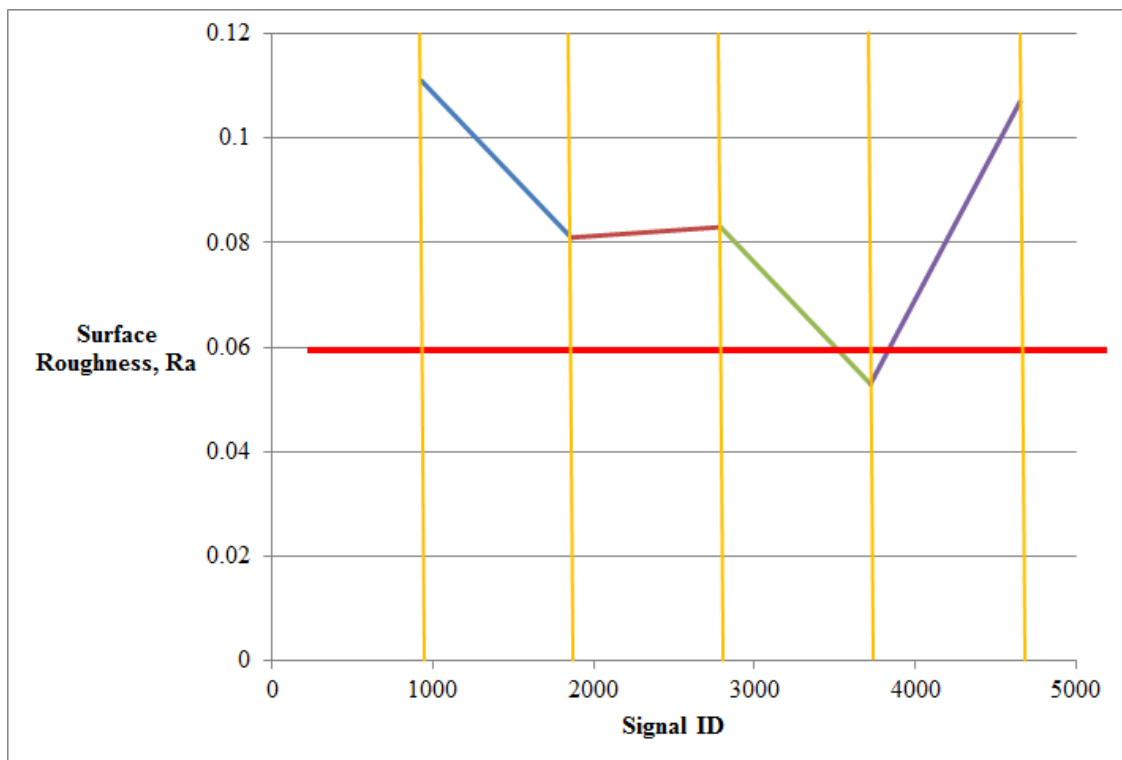


Figure 4.53: Surface Roughness, R_a , trend along the detected sensor signals with a threshold of 0.06.

A surface roughness was obtained for each sensor signal file through interpolation as shown in Figure 4.53. No information is available concerning the initial surface roughness as well as the final surface roughness measurement. In order to be able to correlate the surface with the features obtained, the first and last set of passes have been eliminated. It was assumed that the desired surface roughness to be less than 0.06. The red line is the threshold line. All sensor signals that have an surface roughness value that falls below the red line were considered to have an acceptable surface roughness. Those falling above the red line were considered to have an unacceptable value of surface roughness. So, in correspondence with the graph in Figure 4.53, every sensor signal file was associated with a surface roughness value. In its turn, this surface roughness value was given a “binary” value either 0 or 1, 0 for an unacceptable value of surface roughness and 1 for an acceptable value of surface roughness.

One three-layer feed forward back propagation neural network (FF BP NN) architecture was implemented, 15 input nodes, 45 hidden ones, and 1 output node, i.e. a 15-45-1 architecture. The output layer had only 1 node, yielding a binary value associated with the residual stress condition: 0 = acceptable residual stress and 1 = unacceptable residual stress.

For each of the 30 sensor fusion feature vectors, the NN learning procedures were carried out by using, in turn, the training sets that were formed by the 15 types of sensor fusion pattern vectors as NN input and, as desired NN output, the corresponding one-dimensional vector composed of the binary values identifying the surface roughness value (0 = acceptable; 1 = unacceptable).

In Table 4.29, the NN overall success rate (SR) is reported for each sensor fusion pattern vectors (i.e. each training data set).

By examining the overall NN SR values obtained for all sensor fusion pattern vector, it can be noticed that all SR obtained are high (> 90%) indicating that the assessment process of the surface roughness of a workpiece during the polishing process through the extraction of conventional and WPT features is a reliable method.

Table 4.29: Overall NN SR for all 30 sensor fusion pattern vectors, threshold= 0.06.

SR (%)	
AE_{raw} sensor fusion pattern vectors	
Stat. features	93.56
A	92.85
D	91.58
AA	91.23
DA	92.56
AD	93.85
DD	92.58
AAA	93.12
DAA	91.47
ADA	90.57
DDA	91.56
AAD	91.23
DAD	92.91
ADD	91.19
DDD	93.61
AE_{RMS} sensor fusion pattern vectors	
Stat. features	91.18
A	90.63
D	91.52
AA	92.45
DA	91.56
AD	90.75
DD	91.23
AAA	90.32
DAA	91.23
ADA	92.65
DDA	93.44
AAD	91.81
DAD	90.88
ADD	92.26
DDD	92.85

Another approach was to increase the value of the threshold surface roughness to 0.07 instead of 0.06 (Figure 4.54), thus increasing the number of sensor signal files with an acceptable value of surface roughness. In addition, the first set and the last of polishing passes were also considered for decision making. These sets were considered to have an acceptable value of surface, i.e. the sensor signal files corresponding to these sets were associated with a binary output of “0”.

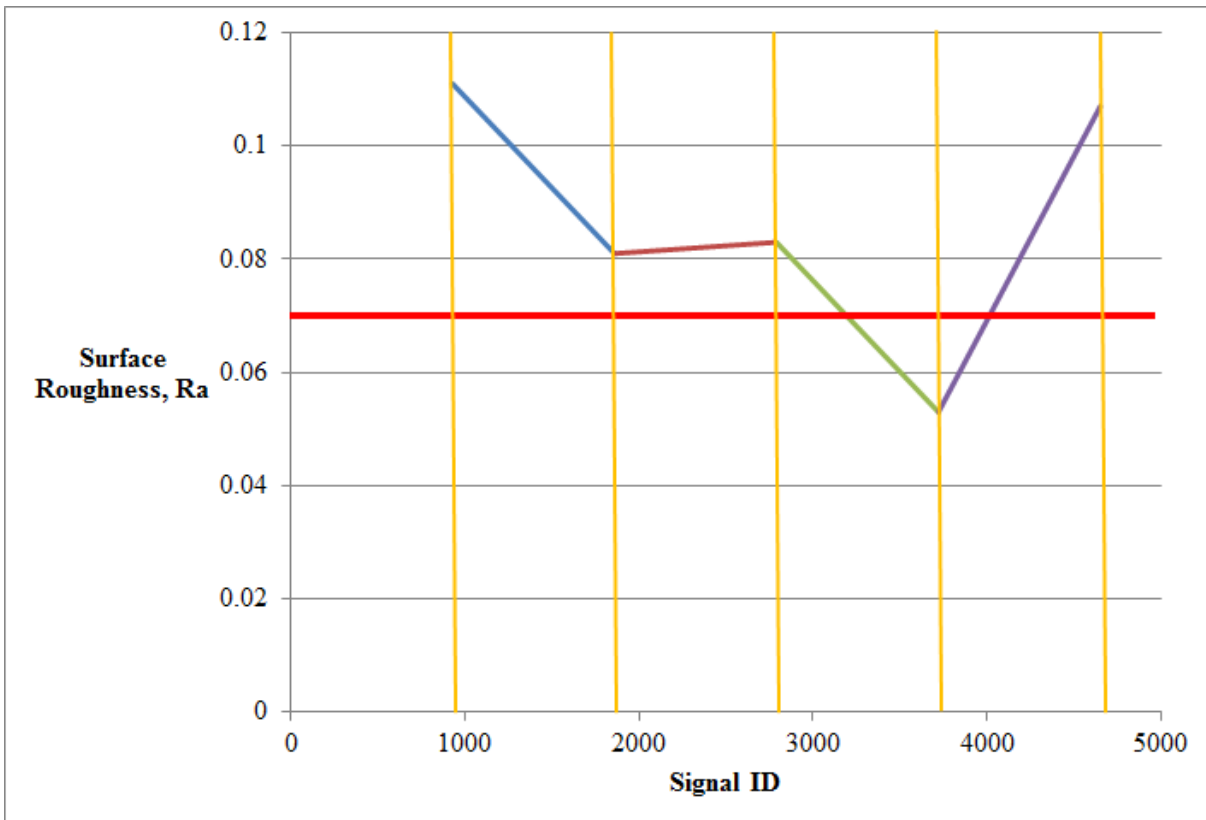


Figure 4.54: Surface Roughness, R_a , trend along the detected sensor signals with a threshold of 0.07.

The NN was trained again using the adjusted sensor fusion pattern vectors and the adjusted binary output vector that now include all the sensor files. Also, for these training datasets, the NN configuration used was 15-45-1. The new resulting SRs are listed in Table 4.30.

The SRs obtained from training the dataset at a threshold of surface roughness of 0.07 are lower than the SRs obtained for the training the dataset at a threshold of surface roughness of 0.06. This is due to the fact that increasing the threshold increases the number of cases, i.e. sensor signals that have an acceptable, ‘1’, corresponding value of surface roughness, which means there is an increase in the probability of error. However, the SRs, in the second training session, are relatively high ranging between 80% and 85%.

Table 4.30: Overall NN SR for all 30 sensor fusion pattern vectors, threshold=0.07.

SR (%)	
AE_{raw} sensor fusion pattern vectors	
Stat. features	82.12
A	81.71
D	80.62
AA	82.52
DA	83.32
AD	81.40
DD	82.21
AAA	83.32
DAA	82.46
ADA	82.59
DDA	80.11
AAD	82.65
DAD	83.56
ADD	82.32
DDD	81.12
AE_{RMS} sensor fusion pattern vectors	
Stat. features	82.82
A	83.82
D	82.53
AA	81.91
DA	80.41
AD	84.46
DD	82.36
AAA	80.12
DAA	81.46
ADA	82.37
DDA	80.34
AAD	82.14
DAD	81.12
ADD	80.12
DDD	81.53

5. Conclusion

The future enhancement of machining systems and their operation performance will vitally depend upon the development and implementation of innovative sensor monitoring systems. These novel systems will need to be robust, reconfigurable, reliable, intelligent and inexpensive in order to meet the demands of advanced manufacturing technology. These demands include increasingly small, precision and complex products for applications in biomedicine, transportation, MEMs devices, etc., as well as ubiquitous sensor systems for machine and system monitoring to reduce resource requirements and insure that manufacturing systems operate efficiently with minimal energy consumption and environmental impact. Luckily, today's sensor systems are becoming increasingly dependable and low-priced and the signal processing capabilities of advanced algorithms and decision making strategies are also rapidly progressing.

There are numerous techniques and methods of signal processing (feature extraction, selection and refinement) and feature integration (decision making) developed in laboratories worldwide, most of them really effective for sensor monitoring of machining operations: the main achievements were reported in sections 3 and 5. Despite industrial data availability or industrial conditions adoption in many studies, very few of these achievements found actual application in the shop floor or in commercially available tool and process conditions monitoring systems. The main reason seems to be the difficult, sophisticated usage of these techniques and methods. Usually, author's tuning of "handmade" configuration is inevitable, making the procedure hardly applicable in industry. Accordingly, one of the main challenges in future machining process monitoring systems is the development of algorithms and paradigms really autonomous from machine tool operators, who are not required to know about methods like wavelet transform, neural networks, etc., with signal feature extraction and decision making performed without intervention of the operator, who should provide only very simple (the lesser, the better) input and information.

Case 1

Cutting force sensor signals were detected during experimental turning tests carried on 1045 carbon steel with variable cutting conditions, generating different chip forms, in a machining sensor monitoring implementation for chip form identification.

The three cutting force component signals, F_x , F_y , and F_z , underwent wavelet packet transform up to the 4th level decomposition using Daubechies 4 as mother wavelet. The output of this decomposition was represented by thirty wavelet packets for each cutting force component signal. From each wavelet packet, five statistical features were calculated to construct wavelet packet statistical feature vectors. A ranking criterion based on the number of overlapping favourable/ unfavourable chip form cases was used to select the 8 highest ranked wavelet feature vectors to input to feed-forward back-propagation neural networks (NN) for unfavourable/favourable chip form pattern recognition.

The overall NN success rate in chip form classification was always greater than 80%, constituting a significant high performance. Nevertheless, a data refinement approach was

carried out to sort out and reject the turning tests conveying high noise into the system. NN training and testing was performed again using the refined data set and the corresponding overall NN success rate in chip form identification attained values higher than 95%.

The very high NN performance achieved confirm that signal analysis and feature extraction based on wavelet packet transform is an effective and powerful method for the implementation of pattern recognition procedures in practical machining sensor monitoring applications such as chip form identification.

Case 2

Experimental turning tests were performed on Inconel 718 cylindrical shafts by varying the cutting conditions and using a multiple sensor monitoring system for the on-line assessment of machined surface integrity in terms of allowable residual stress value.

The cutting force, acoustic emission and vibration sensor signals were processed using the wavelet packet transform technique for the extraction of statistical features from the packet coefficients and the construction of sensor fusion wavelet feature vectors. The latter were selected for feeding into diverse neural network architectures for sensor fusion based decision making on machined surface integrity grounded on X-ray diffraction residual stress measurements.

To facilitate the wavelet feature vector selection, it was suggested to limit the wavelet decomposition process to the 2nd level of wavelet packet transform. The most suitable wavelet feature vector was considered to be the 35-elements wavelet feature vector capable to take into account the contributions from all the extracted features while yielding at the same time a very high, though not the highest, neural network performance in the sensor fusion based classification of residual stress level acceptability.

Case 3

Several sensors have been mounted on the RAP machine at Strecon. The signals detected during the polishing experiments are: acoustic emission, strain, voltage, and current. Furthermore, the surface roughness was measured after a number of passes defined during the performance of the experiment.

The aim was to extract relevant features from the detected signals and relate them relevant to the surface roughness of the polished part. Through the online analysis of the sensor signals, the polishing process should be stopped when the required surface roughness is reached, i.e. the features extracted from the sensor signals will be used to make a decision on when to stop the polishing process. Extracting features through the conventional feature method and wavelet packet transform method proved to reliable in assessing the surface roughness of the workpiece being polished.

References

- [1] Segreto, T., Karam, S., Simeone, A., Teti, R., 2013, Residual Stress Assessment in Inconel 718 Machining Through Wavelet Sensor Signal Analysis and Sensor Fusion Pattern Recognition, 2nd CIRP Global Web Conference (CIRPe2013), Procedia CIRP, Volume 9, ISSN 2212-8271, pp. 103-108.
- [2] Karam, S., Teti, R., 2012, Wavelet Transform Feature Extraction for Pattern Recognition of Chip Form in C Steel Turning, 8th CIRP Int. Conference on Intelligent Computation in Manufacturing Engineering – CIRP ICME '12, 18-20 July, Ischia, Italy, pp. 97-102.
- [3] Teti, R., Jemielniak, K., O'Donnell, G., Dornfeld, D., 2010, Advanced Monitoring of Machining Operations, STC-C Keynote Paper, Annals of the CIRP, Vol. 59/2, ISSN 0007-8506 (CIRP Annals), ISSN 1660-2773 (CD Rom): pp. 717-739.
- [4] Gregory, R.L., 1972. Seeing as Thinking – An Active Theory of Perception. Times Literary Supplement: pp. 707–708.
- [5] Gregory, R.L., 1997. Knowledge in Perception and Illusion. Philosophical Transaction of Royal Society of London B 352: pp. 1121–1128.
- [6] Baicsy, R., 1995. From Active Perception to Active Cooperation: Fundamental Processes of Intelligent Behaviour, in Zangenmeister WH, et al. (Eds.) Visual Attention and Cognition: pp. 309–321.
- [7] Mikell, P. G., 1996. Fundamental of Modern Manufacturing, Prentice Hall International Edition: pp.
- [8] Byrne, G., Dornfeld, D., Denkena, B., 2004. Advancing Cutting Technology. CIRP Annals 52(2): pp. 483–507.
- [9] Gautschi, G., 2002. Piezoelectric sensorics. Springer Berlin, Heidelberg, New York. pp. 3.
- [10] Byrne, G., O'Donnell, G., 2007. An Integrated Force Sensor Solution for Process Monitoring of Drilling Operations. CIRP Annals 56(01): pp. 89–92.
- [11] Rogers, L.M., 1979. The Application of Vibration Analysis and Acoustic Emission Source Location to On-line Condition Monitoring of Anti-friction Bearings. Tribology International: pp. 51–59.
- [12] Park, S., 2004. High Frequency Bandwidth Cutting Force Measurements in Milling Using the Spindle Force Sensor System, PhD Thesis, University of British Columbia, Vancouver, Canada.
- [13] Shull, L. C., 1992. "Basic Circuits", Hannah, R.L. and Reed, S.E. (Eds.). Strain Gage Users' Manual. Society for Experimental Mechanics. ISBN 0-912053-36-4: pp. 122.

- [14] Bruce, M., 2013. Measure it on the machine. In Manufacturing Engineering Media. Retrieved from http://www.sme.org/uploadedFiles/Publications/ME_Magazine/2013/January_2013/January%202013%20f2%20Measurement.pdf.
- [15] ASTM. (1996) E 1316 Terminology for Non-destructive Testing, Annual Book of ASTM Standards; Non-destructive Testing, 03/03.
- [16] Karpuschewski, B., 2001. Sensoren zur Prozeßüberwachung beim Spanen, Habilitationsschrift. University of Hannover, Germany.
- [17] Hundt, W., Leuenberger, D., Rehsteiner, F., 1994. An Approach to Monitoring of the Grinding Process Using Acoustic Emission Techniques. CIRP Annals 43(1): pp. 295–298.
- [18] Nebeß, C., Pflug, C., 1996 Real Time Monitoring and Control of Chip Form in Turning with Acoustic Emission Using Thin Film Sensors, NAMRC XXIV, SME. University of Michigan, Ann Arbor, Michigan.
- [19] Caralon, T.A., Kidd, S.R., Hand, D.P., Wilcox, S.J., Wilkinson, P., Barton, J.S., Jones, J.D.C., Reuben R.L., 1997. AE Monitoring of Tool Wear During the Face Milling of Steels and Aluminium Alloys Using a Fibre Optic Sensor, Part 1: Energy Analysis. IMechE 211: pp. 299–309.
- [20] Caralon, T.A., Kidd, S.R., Hand, D.P., Wilcox, S.J., Wilkinson, P., Barton, J.S., Jones, J.D.C., Reuben, R.L., 1997. AE Monitoring of Tool Wear During the Face Milling of Steels and Aluminium Alloys Using a Fibre Optic Sensor, Part 2: Frequency Analysis. IMechE 211: pp. 311–319.
- [21] Inasaki, I., 1998. Application of Acoustic Emission Sensor for Monitoring Machining Processes. Ultrasonics 36: pp. 273–281.
- [22] Hutton, D.V., Hu, F., 1999. AE Monitoring of Tool Wear in End Milling Using Time Domain Averaging. Journal of Manufacturing Science and Engineering 121: pp. 8–12.
- [23] Jemielniak, K., 2001. Some Aspects of Acoustic Emission Signal Pre-processing. Journal of Material Processing Technology 109: pp. 242–247.
- [24] Woulfe, M., 2000. On the Relationship Between Acoustic Emission and Surface Integrity in Machining, PhD Thesis, University of College Dublin, Eire.
- [25] Dimla, D.E., 2000. Sensor Signals for Tool-wear Monitoring in Metal Cutting: A Review of Methods. International Journal of Machine Tools and Manufacture 40: pp. 1073–1098.
- [26] Li, X., 2002. A Brief Review—Acoustic Emission Method for Tool Wear Monitoring in Turning. International Journal of Machine Tools and Manufacture 42: pp. 157–165.

- [27] Sick, B., 2002. On-line and Indirect Tool Wear Monitoring in Turning with Artificial Neural Networks: A Review of More Than a Decade of Research. *Mechanical Systems and Signal Processing* 16(4): pp. 487–546.
- [28] D'Addona, D., Segreto, T., Simeone, A., Teti, R., 2011. ANN Tool Wear Modelling in the Machining of Nickel Superalloy Industrial Products, *CIRP Journal of Manufacturing Science and Technology, Special Section on Innovative and Cognitive Manufacturing Engineering*, DOI: 10.1016/j.cirpj.2011.07.003, 4/1: pp. 33-37.
- [29] Jemielniak, K., 2000. Some Aspects of AE Application in Tool Condition Monitoring. *Ultrasonics* 38: pp. 604–608.
- [30] Altintas, Y, Park, S.S., 2004. Dynamic Compensation of Spindle-integrated Force Sensors. *CIRP Annals* 53(1): pp. 305–308.
- [31] Ghosh, N., Ravi, A., Patra, S., Mukhopadhyay, S., Mohanty, A., Chattopadhyay, A., 2007. Estimation of Tool Wear During CNC Milling Using NN-based Sensor Fusion. *Mechanical Systems and Signal Processing* 21: pp. 466–479.
- [32] Li, X., Ouyang, G., Liang, Z., 2008. Complexity Measure of Motor Current Signals for Tool Flute Breakage Detection in End Milling. *International Journal of Machine Tools and Manufacture* 48: pp. 371–379.
- [33] Bhattacharyya, P., Sengupta, D., Mukhopadhyay, S., 2007. Cutting Force-based Real-time Estimation of Tool Wear in Face Milling Using a Combination of Signal Processing Techniques. *Mechanical Systems and Signal Processing* 21: pp. 2665–2683.
- [34] Marinescu, I., Axinte, D., 2008. A Critical Analysis of Effectiveness of Acoustic Emission Signals to Detect Tool and Workpiece Malfunctions in Milling Operations. *International Journal of Machine Tools and Manufacture* 48: pp. 1148–1160.
- [35] Dong, J., Subrahmanyam, K.V.R., Wong, Y.S., Hong, G.S., Mohanty, A.R., 2006. Bayesian- inference-based Neural Networks for Tool Wear Estimation. *International Journal of Advanced Manufacturing Technology* 30: pp. 797–807.
- [36] Jemielniak, K., Bombinski, S., Aristimuno, P.X., 2008. Tool Condition Monitoring in Micromilling Based on Hierarchical Integration of Signal Measures. *CIRP Annals* 57(1): pp. 121–124.
- [37] Sick, B., 2002 On-line and Indirect Tool Wear Monitoring in Turning with Artificial Neural Networks: A Review of More Than a Decade of Research. *Mechanical Systems and Signal Processing* 16(4): pp. 487–546.
- [38] Kim, H.Y., Ahn, J.H., 2002. Chip Disposal State Monitoring in Drilling Using Neural Network Based Spindle Motor Power Sensing. *International Journal of Machine Tools and Manufacture* 42: pp. 1113–1119.

- [39] Salgado, D., Alonso, F., 2006. Tool Wear Detection in Turning Operations Using Singular Spectrum Analysis. *Journal of Materials Processing Technology* 171: pp. 451–458.
- [40] Scheffer, C., Heyns, P.C., 2001. Wear Monitoring in Turning Operations Using Vibration and Strain Measurements. *Mechanical Systems and Signal Processing* 15(6): pp. 1185–1202.
- [41] Sun, J., Hong, G.S., Rahman, M., Wong, Y.S., 2004 Identification of Feature Set for Effective Tool Condition Monitoring by AE Sensing. *International Journal of Production Research* 42(5): pp. 901–918.
- [42] Zhu, K., Wong, Y.S., Hong, G.S., 2009. Multi-category Micro-milling Tool Wear Monitoring with Continuous Hidden Markov Models. *Mechanical Systems and Signal Processing* 23: pp. 547–560.
- [43] Binsaeid, S., Asfoura, S., Chob, S., Onarc, A., 2009. Machine Ensemble Approach for Simultaneous Detection of Transient and Gradual Anomalies in Milling Using Multisensor Fusion. *Journal of Materials Processing Technology* 209: pp. 4728–4738
- [44] Huang, B., Chen, J.C., 2003. An In-process Neural Network-based Surface Roughness Prediction System Using a Dynamometer in End Milling Operations. *International Journal of Advanced Manufacturing Technology* 21: pp. 339–347.
- [45] Guo, Y., Ammula, S., 2005. Real-time AE Monitoring for Surface Damage in Hard Machining. *International Journal of Machine Tools and Manufacture* 45: pp. 1622–1627.
- [46] Kwak, J.S., Song, J.B., 2001. Trouble Diagnosis of the Grinding Process by Using AE Signals. *International Journal of Machine Tools and Manufacture* 41: pp. 899–913.
- [47] Al-Habaibeh, A., Gindy, N., 2000. A New Approach for Systematic Design of Condition Monitoring Systems for Milling Processes. *Journal of Materials Processing Technology* 107: pp. 243–251.
- [48] El-Wardany, T.I., Gao, D., Elbestawi, M.A., 1996. Tool Condition Monitoring in Drilling Using Vibration Signature Analysis. *International Journal of Machine Tools and Manufacture* 36: pp. 687–711.
- [49] Rene de Jesus, R.T., Gilberto, H.R., Ivan, T.V., Carlos, J.C.J., 2004. FPGA Based On-line Tool Breakage Detection System for CNC Milling Machines. *Mechatronics* 14: pp. 439–454.
- [50] Jemielniak, K., Kwiatkowski, L., Wrzosek, P., 1998. Diagnosis of Tool Wear Based on Cutting Forces and AE Measures as Inputs to Neural Network. *Journal of Intelligent Manufacturing* 9: pp. 447–455.
- [51] Govekar, E., Gradisek, J., Grabec, I., 2000. Analysis of AE Signals and Monitoring of Machining Processes. *Ultrasonics* 38: pp. 598–603.

- [52] Teti R., Jawahir I.S., Jemielniak, K., Segreto, T., Chen, S., Kossakowska, J., 2006. Chip Form Monitoring through Advanced Processing of Cutting Force Sensor Signals. *CIRP Annals* 55(1): pp. 75–80.
- [53] Jemielniak, K., Teti, R., Kossakowska, J., Segreto, T., 2006 Innovative Signal Processing for Cutting Force Based Chip Form Prediction. 2nd Virtual Int Conf. on IPROMS, 3–14 July, pp. 7–12.
- [54] D'Addona, D., Keshari, A., Teti, R., 2008. Spectrum Estimation and Processing of Cutting Force Sensor Signals for Chip Form Monitoring and Classification. 4th Virtual Int. Conf. on IPROMS, 1–14 July, pp. 555–560.
- [55] Venuvinod, P.K., Djordjevich, A., 1996. Towards Active Chip Control. *CIRP Annals* 45(1): pp. 83–86.
- [56] Andreasen, J.L., De Chiffre, L., 1998. An Automatic System for Elaboration of Chip Breaking Diagrams. *CIRP Annals* 47(1): pp. 35–40.
- [57] Outeiro, J.C., Pina, J.C., M'Saoubi, R., Pusavec, F., Jawahir, I.S., 2008. Analysis of residual stresses induced by dry turning of difficult-to-machine materials, *CIRP Annals* 57(1): pp. 77-80.
- [58] Tönshoff, H.K., Jung, M., Männel, S., Rietz, W., 2000. Using acoustic emission signals for monitoring of production processes, *Ultrasonics*, 37(10): pp. 681-686.
- [59] Azouzi, R., Guillot, M., 1997. On-line Prediction of Surface Finish and Dimensional Deviation in Turning Using Neural Network Based Sensor Fusion. *International Journal of Machine Tools and Manufacture* 37(9): pp. 1201–1217.
- [60] Abouelatta, O., Madl, J., 2001. Surface Roughness Prediction Based on Cutting Parameters and Tool Vibration in Turning. *Journal of Materials Processing Technology* 118: pp. 269–277.
- [61] Salgado, D.R., Alonso, F.J., Cambero, I., Marcelo, A., 2009. In-Process Surface Roughness Prediction System Using Cutting Vibrations in Turning. *International Journal of Advanced Manufacturing Technology* 43: pp. 40–51.
- [62] Song, D.Y., Otani, N., Aoki, T., Kamakoshi, Y., Ohara, Y., Tamaki, H., 2005. A New Approach to Cutting State Monitoring in End-mill Machining. *International Journal of Machine Tools and Manufacture* 45: pp. 909–921.
- [63] Axinte, D., Gindy, N., Fox, K., Unanue, I., 2004. Process Monitoring to Assist the Workpiece Surface Quality in Machining. *International Journal of Machine Tools and Manufacture* 44: pp. 1091–1098.

- [64] Chang, H.K., Kim, J.H., Kim, H., Jang, D.Y., Han, D.C., 2007. In-process Surface Roughness Prediction Using Displacement Signals from Spindle Motion. *International Journal of Machine Tools and Manufacture* 47: pp. 1021–1026.
- [65] Axinte, D., Boud, F., Penny, J., Gindy, N., Williams, D.J., 2005. Broaching of Ti-6-4 – Detection of Workpiece Surface Anomalies on Dovetail Slots Through Process Monitoring. *CIRP Annals* 54(1): pp. 87–90.
- [66] Marinescu, I., Axinte, D., 2009. A Time–frequency Acoustic Emission-based Monitoring Technique to Identify Workpiece Surface Malfunctions in Milling with Multiple Teeth Cutting Simultaneously. *International Journal of Machine Tools and Manufacture* 49(1): pp. 53–65.
- [67] Axinte, D., 2007. An Experimental Analysis of Damped Coupled Vibrations in Broaching. *International Journal of Machine Tools and Manufacture* 47(14): pp. 2182–2188.
- [68] Marinescu, I., Axinte, D., 2008. A Critical Analysis of Effectiveness of AE Signals to Detect Tool and Workpiece Malfunctions in Milling Operations. *International Journal of Machine Tools and Manufacture* 48(10): pp. 1148–1160.
- [69] Axinte, D., Natarajan, D., Gindy, N.N., 2005. An Approach to Use an Array of Three AE Sensors to Locate Uneven Events in Machining-Part 1: Method and Validation. *International Journal of Machine Tools and Manufacture* 45(14): pp. 1605–1613.
- [70] Rawat, S., Attia, H., 2009. Characterization of the Dry High Speed Drilling Process of Woven Composites Using Machinability Maps Approach. *CIRP Annals* 58(1): pp. 105–108.
- [71] Teti, R., Kumara, S.R.T., 1997. Intelligent Computing Methods for Manufacturing Systems, STC-O KN Paper. *CIRP Annals* 46(2): pp. 629–652.
- [72] Rumelhart, D.E., Hinton, G.E., Williams, R.J., 1986. Learning Internal Representations by Error in Propagation, in McClelland, Rumelhart, and the PDP Research Group (Eds.) *Parallel Distributed Processing: Exploration in the Microstructures of Cognition*, Foundations, (1).
- [73] Levenberg, K., A Method for the Solution of Certain Non-linear Problems in Least Squares. *Quarterly of Applied Mathematics* 1944. 2(2): pp. 164–168.
- [74] Dreyfus, G., 2005. *Neural nets: Methodology & Applications*. Springer.
- [75] Haykin, S., 2008. *Neural Networks & Learning Machines*. Prentice-Hall.
- [76] Specht, D.F., 1990. Probabilistic NN. *Neural Networks* 3(1): pp. 109–118.
- [77] Schmidhuber, J., Wierstra, D., Gagliolo, M., Gomez, F., 2007. Training Recurrent Networks by Evolino. *Neural Computation* 19(3): pp. 757–779.

- [78] Schuster, M., Paliwal, K.K., 1997. Bidirectional Recurrent Neural Networks. *IEEE Transactions on Signal Processing* 45: pp. 2673–2681.
- [79] Pearlmutter, B.A., 1995. Gradient Calculations for Dynamic Recurrent Neural Networks: A Survey. *IEEE Transactions on NNs* 6(5): pp. 1212–1228.
- [80] Daisuke, H., Tomoharu, N., 2001. 2-D Artificial Cellular NN and Its Application to Chase Game. *Transactions on Institute of Electrical Engineers of Japan* 6: pp. 1071–1079.
- [81] Halgamuge, S.K., Glesner, M., 1984. NNs in Designing Fuzzy Systems for Real World Applications. *Fuzzy Sets and Systems* 65: pp. 1–12.
- [82] Kohonen, T., 1984. *Self-organisation and Associative Memory*. Springer-Verlag, Berlin.
- [83] Axinte, D., 2006. Approach into the Use of Probabilistic Neural Networks for Automated Classification of Tool Malfunctions in Broaching. *International Journal of Machine Tools and Manufacture* 46(12-13): pp. 1445–1448.
- [84] Kamarthi, S.V., Kumara, S.R.T., Cohen, P.H., 2000. Flank Wear Estimation in Turning through Wavelet Representation of Acoustic Emission Signals. *Journal of Manufacturing Science and Engineering* 122(1): pp. 12–19.
- [85] Kamarthi, S.V., Sankar, G.S., Cohen, P.H., Kumara, S.R.T., 1991. On-line Tool Wear Monitoring Using a Kohonen's Feature Map. *Int. Conf. on ANNIE'91, St. Louis, MO, November 10–13, 1*, pp. 639–644.
- [86] Bukkapatnam, S., Kumara, S., Lakhtakia, A., 2000. Fractal Estimation of Flank Wear in Turning. *Journal of Dynamic System Measurements & Control*. 122(1): pp. 89–94.
- [87] Bukkapatnam, S.T.S., Kumara, S.R.T., Lakhtakia, A., 1994. Fractal Estimation of Flank Wear in Turning Using Time-delay Neural Networks. *ASME Press, New York*. pp. 575–580.
- [88] Bukkapatnam, S.T.S., Kumara, S.R.T., Lakhtakia, A., Srinivasan, P., (2002) Neighborhood Method and Its Coupling with the Wavelet Method for Nonlinear Signal Separation of Contaminated Chaotic Time-series Data. *Signal Processing* 82(10): pp. 1351–1374.
- [89] Kim, H.Y., Ahn, J.H., 2002. Chip Disposal State Monitoring in Drilling Using Neural Network Based Spindle Motor Power Sensing. *International Journal of Machine Tools and Manufacture* 42(10): pp. 1113–1119.
- [90] Lu, M.C., Kannatey, A.Jr., 2000. Analysis of Sound Signal Generation Due to Flank Wear in Turning. *Int ME Congr & Exp, Orlando*.
- [91] Kim, H., Ahn, J., Kim, S., Takata, S., 2002. Real Time Drill Wear Estimation Based on Spindle Motor Power. *Journal of Materials Processing Technology* 124(3): pp. 267–273.

- [92] Rubio, E.M., Teti, R., 2009. Cutting Parameters Analysis for the Development of a Milling Process Monitoring System Based on Audible Energy Sound. *Journal of Intelligent Manufacturing* 20(1): pp. 43–54.
- [93] Teti, R., Baciù, I.L., Rubio, E.M., 2005. Sensor Monitoring of Machining Based on Audible Sound Detection and Analysis. 18th Int. Conf. on Production Research – ICPR 18, Salerno, 1–4 Ago, 47.
- [94] Teti, R., Baciù, I.L., Rubio, E.M., 2004. Neural Network Classification of Audible Sound Signals for Process Monitoring During Machining. 15th Int. DAAAM Symp. on Intelligent Manufact. Systems, pp. 459–460.
- [95] Klein, L.A., 2004. *Sensor and Data Fusion: A Tool for Information Assessment and Decision Making*. SPIE Press Book.
- [96] Hall, D., Llinas, J., 2001. *Handbook of Multisensor Data Fusion*. CRC.
- [97] Mitchell, H.B., 2007. *Multi-sensor Data Fusion: An Introduction*. Springer-Verlag, Berlin/Heidelberg.
- [98] Segreto, T., Neugebauer, R., 2009- Sensor Fusion of Sensor Signals during Machining of Difficult-to-machine Metal Alloys. AITeM 2009, Torino, 7–9 September, 199.
- [99] Teti, R., Segreto, T., 2008. Sensor Monitoring for Cutting Process Optimisation of Low Machinability Materials. 5th Chemnitz Colloq. on Prod. Techn. – CPK, Chemnitz, pp. 237–256.
- [100] Segreto, T., Teti, R., 2008. Sensor Fusion of Acoustic Emission and Cutting Force for Tool Wear Monitoring during Composite Materials Machining. 6th CIRP Int. Conf. on ICME, Naples, 23–25 July, pp. 221–226.
- [101] Teti, R., Segreto, T., Neugebauer, R., Harzbecker, C., 2008. Sensor Monitoring Based Optimisation during Turning of Titanium Alloys. 4th Virtual Int. Conf. on IPROMS, 1–14 July, pp. 547–554.
- [102] Teti, R., Segreto, T., Neugebauer, R., Harzbecker, C., 2008. Process Acceptability in Turning of Ti alloys based on Cutting Force Sensor Monitoring. 3rd Int. Conf. High Perf. Cutt, Dublin, 12–13 June, pp. 241–250.
- [103] Byrne, G., Dornfeld, D., Inasaki, I., König, W., Teti, R., 1995. Tool Condition Monitoring – The Status of Research and Industrial Application. *CIRP Annals* 44(2): pp. 541–567.
- [104] Stearns, S.D., Hush, D.R., 1990. *Digital Signal Analysis*. Prentice-Hall.
- [105] Rabiner, R.L., Shafer, R.W., 1978. *Digital Signal Processing of Speech Signals*. Prentice-Hall, Englewood-Cliffs.

- [106] Teti, R., Buonadonna, P., 1999. Round Robin on AE Monitoring of Machining. *Annals of the CIRP* 48(3): pp. 47–69.
- [107] Duda, R.O., Hart, P.E., 1973. *Pattern Classification and Scene Analysis*. J. Wiley and Sons, New York.
- [108] Masters, T., 1993. *Practical Neural Network Recipes in C++*. Academic Press Inc., San Diego, CA.
- [109] Segreto, T., Teti, R., Neugebauer, R., Schmidt, G., 2009. Machinability Assessment in Turning of NiTi Through Acceleration Sensor Monitoring. 2nd Int. Researchers Symp. on IPROMS, Ischia, 22–24 July, pp. 75–80.
- [110] Teti, A., Segreto, T., Neugebauer, R., Schmidt, G., 2009. Vibration Signal Detection and Conditioning for Machinability Analysis of Ti alloy Turning. 2nd Int. Resear. Symp. on IPROMS, Ischia, 22–24 July, pp. 93–96.
- [111] Teti, R., 1995. A Review of Tool Condition Monitoring Literature Database. *CIRP Annals* 44(2): pp. 659–666.
- [112] Wang, W., Hong, G., Wong, Y., Zhu, K., 2007. Sensor Fusion for On-line Tool Condition Monitoring in Milling. *International Journal of Production Research* 45(21): pp. 5095–5116.
- [113] Simeone, A., Segreto, T., Teti, R., 2013. Residual Stress Condition Monitoring via Sensor Fusion in Turning of Inconel 718, *Procedia CIRP*: 12: pp. 67-72.
- [114] Addison, P.S., 2002. *The Illustrated Wavelet Transform Handbook*, Institute of Physics.
- [115] Percival, D.B., Walden, A.T., 2000. *Wavelet Methods for Time Series Analysis*, Cambridge University Press.
- [116] Misiti, M., Misiti, Y., Oppenheim, G., Poggi, J.M., 1996. “Wavelet Toolbox for Use with Matlab”, Version 1.
- [117] Graps, A., 1995. An Introduction to Wavelets. *IEEE Computational Science & Engineering*. 2(2): pp. 50-61.
- [118] Vandenhouten, R., 1998. *Analyse nichtstationärer Zeitreihen komplexer Systeme und Anwendungen in der Physiologie (Non-stationary Time Series Analysis of Complex Systems and Applications in Physiology)*. Shaker. Aachen.
- [119] Faradji, F., Faradji, F., Rabab, K., Birch, W., Birch, G.E., 2013. Using Autoregressive Models of Wavelet Bases in the Design of Mental Task-Based BCIs, *Brain-Computer Interface Systems - Recent Progress and Future Prospects*.

- [120] Amiri, G.G., Asadi, A., 2009. Comparison of Different Methods of Wavelet and Wavelet Packet Transform in Processing Ground Motion Records, *International Journal of Civil Engineering*, 7(4): pp. 248-257.
- [121] McCulloch, W., Walter, P. 1943. "A Logical Calculus of Ideas Immanent in Nervous Activity". *Bulletin of Mathematical Biophysics* 5 (4): pp. 115–133.
- [122] Hoskins, J.C., Himmelblau, D.M., 1992. "Process control via artificial neural networks and reinforcement learning". *Computers & Chemical Engineering* 16 (4): pp. 241–251.
- [123] Rosenblatt, F., 1958. "The perceptron: a probabilistic model for information storage and organization in the brain". *Psychological Review* 65 (6): pp. 386–408.
- [124] Basu, J.K., Bhattacharyya, D., Kim, T., 2010. Use of Artificial Neural Network in Pattern Recognition, *Int. Journal of Software Engineering and Its Applications*; 4(2), pp. 23.
- [125] Gurney, K., 1997. *An Introduction to Neural Networks* London.
- [126] Mohri, M., Rostamizadeh, A., Talwalkar A., 2012. "*Foundations of Machine Learning*". The MIT Press.
- [127] Jordan, M.I., Bishop, C.M., 2004. "Neural Networks". In Allen B. Tucker. *Computer Science Handbook, Second Edition (Section VII: Intelligent Systems)*. Boca Raton, FL: Chapman & Hall/CRC Press LLC.
- [128] Williams, R. J., 1987. A class of gradient-estimating algorithms for reinforcement learning in neural networks. *Proceedings of the IEEE First International Conference on Neural Networks*.
- [129] Fukunaga, K., 1990. "Introduction to Statistical Pattern Recognition", 2nd ed. Boston: Academic Press.
- [130] Bishop, C., 2006. "Pattern Recognition and Machine Learning". Berlin: Springer.
- [131] Feedforward Backpropagation Neural Networks <http://goo.gl/P9D2J>
- [132] Karsoliya, S., 2012. Approximating Number of Hidden layer neurons in Multiple Hidden Layer BPNN Architecture. *International Journal of Engineering Trends and Technology*: 31(6): pp.714 – 717.
- [133] A Feedforward Neural network: <http://goo.gl/YpQA4F>
- [134] Levenberg, K., 1944. A Method for the Solution of Certain Non-linear Problems in Least Squares. *Quarterly of Applied Mathematics*, 2(2): pp. 164–168.
- [135] Marquardt, D.W., 1963. An Algorithm for the Least-Squares Estimation of Nonlinear Parameters, *SIAM Journal of Applied Mathematics*; 11(2), pp. 431-441.

- [136] Mittelman, H.D., 2004. The Least Squares Problem. [web page] <http://plato.asu.edu/topics/problems/nlolsq.html>, [Accessed on 4 Feb. 2014.].
- [137] Lourakis, M.I.A., 2005. Brief Description of the Levenberg-Marquardt Algorithm Implemented by Levmar, *Foundation of Research and Technology*; 4, pp. 1-6.
- [138] Moller, M.F., 1993. A Scaled Conjugate Gradient Algorithm for Fast Supervised Learning. *Neural Networks*, 6: pp. 525-533.
- [139] <http://www.mathworks.it/it/help/nnet/ref/trainlm.html>
- [140] <http://goo.gl/Euca3>
- [141] Jawahir, I.S., Van Luttervelt, C.A., 1993. Recent Developments in Chip Control Research and Applications, *CIRP Annals*; 42(2), pp. 659-693.
- [142] Segreto, T., Andreasen, J. L., De Chiffre, L., Teti, R., 2005. Chip Form Monitoring in Turning Based on Neural Network Processing of Cutting Force Sensor Data, 1st Virtual Int. Conf. on Intelli-gent Production Machines and Systems - IPROMS 2005, pp. 609.
- [143] Teti, R., Jawahir, I. S., Segreto, T., Chen, S., 2006. Cutting Force Signal Pattern Recognition for Chip Form Identification, 5th CIRP Int. Sem. on Intelligent Computation in Manufacturing Engineering - CIRP ICME '06. Ischia, Italy: pp. 7.
- [143] Segreto, T., Simeone, A., Teti, R., 2012. Chip Form Classification in Carbon Steel Turning through Cutting Force Measurement and Principal Components Analysis, *Procedia CIRP*; 2: pp. 49.
- [144] Jemielnak, K., Kossakowska, J., 2006. Chip Form Recognition in Turning Based on Wavelet Transform of Cutting Force Signals, 1st Jubilee Conf. on Manufacturing Engineering in Time of Information Society. Gdansk, Poland, pp. 155.
- [145] Sifuzzaman, M., Islam, M.R., Ali, M.Z., 2009. Application of Wavelet Transform and its Advantages Compared to Fourier Transform, *Journal of Physical Sciences*; 13: pp.121.
- [146] Jemielnak, K., Kossakowska, J., 2010. Tool Wear Monitoring based on Wavelet Transform of Raw Acoustic Emission Signal, *Advances in Manufacturing Science and Technology*; 34(3): pp. 5.
- [147] Wu, Y.L., Agrawal, D., El Abbadi, A, 2000. Comparison of DFT and DWT Based Similarity Search in Time-Series Databases, 9th Int. Conf. on Information and Knowledge Management; Santa Barbara, USA: pp. 488.
- [148] Groover, M.P., 2010. *Theory of Chip Formation in Metal Machining, Fundamentals of Modern Manufacturing: Materials, Processes, and Systems*, 4th ed.: pp. 489-490.
- [149] Trent, E.M., Wright, P. K., 2000. *Metal Cutting*, 4th ed. Butterworth Heinemann, Boston.

- [150] ISO 3685, 1993. Tool-Life Testing with Single-Point Turning Tools, Annex G, pp. 44-45.
- [151] Keshari, A., Teti, R., 2009. Data Refinement and Analysis of Cutting Force Sensor Signals for the Improvement of Chip Form Identification Accuracy, 5th Virtual Int. Conf. on Intelligent Production, Machines and Systems – IPROMS 2009; pp. 149.
- [152] Keshari, A., D’Addona, D., Teti, R., 2008, “Subtraction of Inconsistence Sensor Data to Improve the Chip Form Classification and Monitoring Efficiency,” 6th CIRP Int. Conf. on Intelligent Computation in Manufacturing Engineering - CIRP ICME ’08. Naples, Italy, pp. 205.
- [153] Outeiro, J.C., Pina, J.C., M’Saoubi, R., Pusavec, F., Jawahir, I.S., 2008. Analysis of residual stress induced by dry turning of difficult-to-machine materials, CIRP Annals: 57(1), pp. 77.
- [154] Matsumoto, Y., Hashimoto, F., Lahoti, G., 1999. Surface integrated generated by precision hard turning, CIRP Annals, 48(1): pp. 59.7
- [155] <http://www.itescam.edu.mx/principal/sylabus/fpdb/recursos/r49682.PDF>
- [156] Prevéy, P., 1986. X-ray Diffraction Residual Stress Techniques, Metals Handbook, 10, pp 380-392.
- [157] M.E. Hilley, Ed., 1971. Residual Stress Measurement by X-Ray Diffraction, SAE J784a, Society of Automotive Engineers, Warrendale, PA, pp. 20.
- [158] A.L. Christenson and E.S. Rowland, 1953, Trans. ASM, 45, p.p 638.
- [159] D.P. Koistinen and R.E. Marburger, 1959, Trans. ASM, 51, pp. 537.
- [160] W.A. Rachinger, 1948, J. Sci. Instr., 25, 1948, pp. 254.
- [161] S.K. Gupta and B.D. Cullity, 1980, Adv. X-Ray Anal., 23, 1980, pp. 333.
- [162] P.S. Prevéy, Adv. X-Ray Anal., pp. 29.
- [163] <http://www.aviationmetals.net/inconel.php>
- [164] Segreto, T., Simeone, A., Teti, R., 2013. Multiple Sensor Monitoring in Nickel Alloy Turning for Tool Wear Assessment via Sensor Fusion, Procedia CIRP, 12, pp. 85-90.
- [165] Segreto, T., Simeone, A., Teti, R., 2012. Sensor Fusion for Tool State Classification in Nickel Superalloy High Performance Cutting, Procedia CIRP, 1, pp. 593-598.
- [166] Teti, R., D’Addona, D., Segreto, T., Simeone, A., De Chiara, G., Gabriele, L., Marrone, R., 2008. “Neural Network Tool Wear Prediction in Turning of Inconel 718”, 6th CIRP

Conference on Intelligent Computation in Manufacturing Engineering – CIRP ICME '08. Naples, Italy, pp. 199.

[167] Segreto, T., Teti, R., 2008. Sensor Fusion of Acoustic Emission and Cutting Force for Tool Wear Monitoring during Composite Materials Machining, 6th CIRP Conference on Intelligent Computation in Manufacturing Engineering - CIRP ICME '08. Naples, Italy, pp. 221.

[168] Whitehouse, D.J., 1994: "Handbook of Surface Metrology", Ch. 2, pp. 2-21.

[169] Degarmo, E.P., Black, J., Kohser, R.A., 2003. Materials and Processes in Manufacturing (9th ed.), Wiley, pp. 223.

[170] <http://hallite.com/technical-and-design/design-information/surface-roughness/>

[171] ISO 11562:1996 Geometrical Product Specifications (GPS) – Surface texture: Profile method – Metrological characteristic of phase correct filters.

[172] Zeng, W., Jiang, X., Scott, P., J, 2010. Fast algorithm of the robust Gaussian regression filter for areal surface analysis. Measurement Science and Technology.

[173] ISO 4288, 1996. Geometrical Product Specifications (GPS) – Surface Texture: Profile method – rules and procedures for the assessment of surface texture, International Organization for Standardization.

[174] De Chiffre, L., 2011. "Geometrical Metrology and Machine Testing", Ch. 1 & Ch. 2, pp. 205-235.

[175] Leach, R., 2011. "Optical Measurement of Surface Topography", Springer Editor, Ch.1, pp. 2-7, Ch. 2, pp. 16-22.

[176] ISO 3274:1996 Geometrical Product Specifications (GPS) – Surface texture: Profile method –Nominal characteristics of contact (stylus) instruments.

[177] Mills, M., 2005. Basic Structure of a stylus profilometer.

[178] Radhakrishnan, V., 1970. Effect of stylus radius on the roughness values measured with tracing stylus instruments, Wear 16.

[179] Leach., R., 2010. "Fundamentals principles of engineering nanometrology", Elsevier Inc., Oxford, UK.

[180] Russel, P., Batchelor, D., Thornton., J. " SEM and AFM: Complementary Techniques for High Resolution Surface Investigation".